

Geometrically programmed self-limited assembly of tubules using DNA origami colloids

Daichi Hayakawa,¹ Thomas E. Videbæk,¹ Douglas M. Hall,² Huang Fang,³ Christian Sigl,³ Elija Feigl,³ Hendrik Dietz,³ Seth Fraden,¹ Michael F. Hagan,¹ Gregory M. Grason,² and W. Benjamin Rogers^{1,*}

¹*Martin A. Fisher School of Physics, Brandeis University, Waltham, Massachusetts 02453, USA*

²*Department of Polymer Science and Engineering,
University of Massachusetts, Amherst, Massachusetts 01003, USA*

³*Department of Physics, Technical University of Munich, Munich, Germany*

Self-assembly is one of the most promising strategies for making functional materials at the nanoscale, yet new design principles for making self-limiting architectures, rather than spatially unlimited periodic lattice structures, are needed. To address this challenge, we explore the trade-offs between addressable assembly and self-closing assembly of a specific class of self-limiting structures: cylindrical tubules. We make triangular subunits using DNA origami that have specific, valence-limited interactions and designed binding angles, and study their assembly into tubules that have a self-limited width that is much larger than the size of an individual subunit. In the simplest case, the tubules are assembled from a single component by geometrically programming the dihedral angles between neighboring subunits. We show that the tubules can reach many micrometers in length and that their average width can be prescribed through the dihedral angles. We find that there is a distribution in the width and the chirality of the tubules, which we rationalize by developing a model that considers the finite bending rigidity of the assembled structure as well as the mechanism of self-closure. Finally, we demonstrate that the distributions of tubules can be further sculpted by increasing the number of subunit species, thereby increasing the assembly complexity, and demonstrate that using two subunit species successfully reduces the number of available end states by half. These results help to shed light on the roles of assembly complexity and geometry in self-limited assembly and could be extended to other self-limiting architectures, such as shells, toroids, or triply-periodic frameworks.

Self-assembly is a fundamental building principle used by Nature to make functional materials, including virus capsids for encapsulation and delivery [1], cytoskeletal filaments for transport [2], and macromolecular machines with diverse roles, like the ribosome for protein synthesis [3]. Recently, there has been considerable effort aimed at mimicking biological self-assembly to synthesize user-prescribed structures from synthetic nanometer- and micrometer-scale particles. For example, by encoding short-range specific interactions, DNA-grafted colloidal particles can be programmed to assemble into a variety of two- and three-dimensional crystal phases with prescribed symmetry groups and lattice constants [4–7]. However, rather than unbounded crystal phases, the aforementioned biological functionalities—encapsulation, motility, and protein synthesis—arise from self-limiting structures that have one or more self-limited length scales.

How does one go beyond periodic lattice structures with macroscopically uncontrolled dimensions, to program the assembly of self-limiting architectures that have self-limited length scales that are arbitrarily large with respect to the size of the individual subunits [8]? There are two prominent paradigms for prescribing self-limited assembly: 1) addressable assembly and 2) self-closing assembly. In addressable assembly, every component of a multi-species ensemble is distinct and is programmed to

occupy a specific location within a target structure [9–11]. Therefore, increasing the self-limited length scale necessitates increasing the assembly complexity in terms of the number and interaction specificity of the subunits. In self-closing assembly, anisotropic interactions give rise to the accumulation of curvature during growth that causes the structure to self-close at a finite size [8]. In contrast to addressable assembly, the self-limited length scale in self-closing assembly is therefore controlled by the binding angles between neighboring subunits and is programmed geometrically rather than through specific interactions, and as such, may require only one or relatively few subunits to target a specific self-closing size. But which strategy should one select for a particular target geometry, and which approach is more accurate, precise, or economical? Because the vast majority of examples either address only one paradigm or do not distinguish between the two, as in DNA-coated colloids [12], DNA tiles [13–17], hierarchical assembly of DNA origami [18–20] and designed proteins [16, 21], direct comparisons between addressability and geometry in prescribing self-limited assembly are obscured.

In this article, we create an experimental platform using DNA origami for examining the roles of geometric and interaction specificity in arguably the simplest system that could in principle be programmed by geometry alone: the assembly of cylindrical tubules from rigid triangular monomers. The tubule is the ideal target geometry because it represents an infinitely large class of structures, each of which can be assembled from a *sin-*

* wrogers@brandeis.edu

gle subunit species by controlling the dihedral angles between neighboring subunits. As anticipated, we show that we can vary the self-limited width of the tubules by tuning the dihedral angles between neighboring subunits without changing the interaction complexity. However, we find that the width of the assembled tubules takes a range of values and that the distribution broadens upon increasing the mean tubule width. We discuss how this distribution of the self-limited width is a generic feature of self-closing assembly when the self-limited length scale is sufficiently large compared to the size of the building block [22], which we understand using a simple theory. We conclude by exploring how increasing the assembly complexity enables us to constrain the width distribution by using multiple species of triangles with increased numbers of specific interactions. For a binary mixture of triangle species, we validate that the allowed states of the assembled tubules are reduced by half, as expected from simple geometrical arguments.

RESULTS AND DISCUSSION

A. Design principles

Our system consists of rigid triangular subunits made by DNA origami [20] that encode all of the information necessary to self-assemble tubules with user-prescribed geometries (Fig. 1A). Assembling tubules from triangular subunits requires that we specify two types of information: 1) the interaction specificity between the edges and 2) the local curvature between neighboring subunits. We encode the specific interactions by using unique protrusions and recesses that give rise to shape-complementary lock-and-key interactions whose attraction originates from blunt-end stacking (Fig. 1B) [23]. At a minimum, we require three specific interactions—one per side—which are each homophilic. These three specific interactions allow the triangular subunits to assemble into a deterministic triangular lattice, where each side aligns with one of the three lattice directions.

Additionally, we encode the local curvature by specifying the dihedral angles between neighboring subunits. Specifically, we design the bevel angles of each side of the triangular subunit such that it forms the three dihedral angles with its three neighbors corresponding to a target tubule geometry (Fig. 1C). For example, the subunit in Fig. 1B–C, which assembles into a tubule with five subunit edges in circumference, has dihedral angles of 138.2, 138.2, and -158.4 degrees for sides 1, 2, and 3, respectively. The accumulation of curvature from the dihedral angles upon assembly results in the formation of a curved triangular lattice. For appropriately chosen angles, the lattice will close upon itself to form a tubule (Fig. 1D), which can be chiral or achiral depending on how the tubule closes (Fig. 1E). See Supplementary Information II for more details of the tubule geometry.

Because the curvature originates from the combination

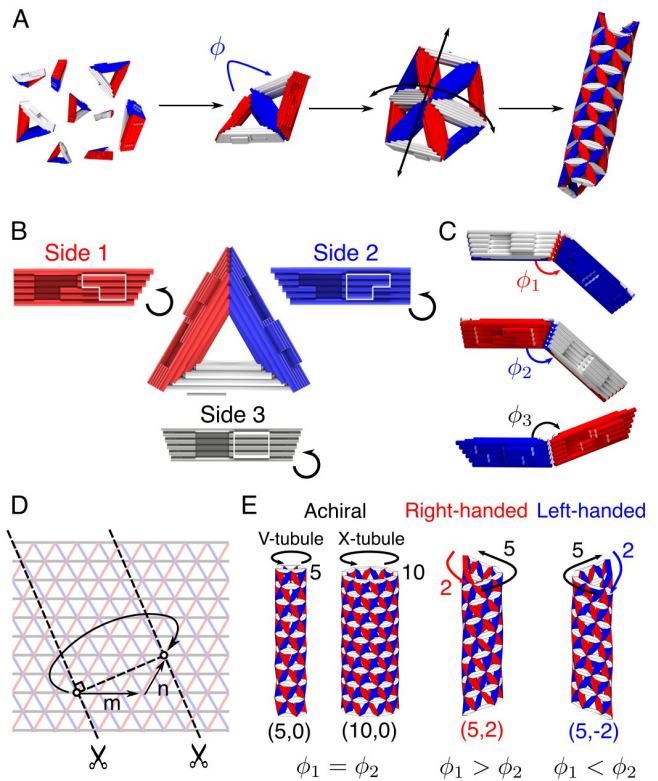


FIG. 1. **Overview of the design rules for tubule assembly.** (A) Triangular subunits bind at the edges with dihedral angles ϕ that specify the principal curvatures of the assembly to favor the formation of cylindrical tubules. (B–C) Design principles of triangular subunits assembling into tubules. (B) Each side has self-complementary lock-and-key interactions encoded in shape-complementary protrusions and recesses. Holes are shaded, while protrusions are highlighted with white. Black arrows indicate the sides that bind together. In this case, each side binds to itself. (C) The sides are also beveled so that when two triangles bind, they form a unique dihedral angle ϕ that is determined by the bevel angle. (D) A triangular lattice that is cut along two parallel lines can be rolled into a tubule, with periodicity determined by indices m and n . m denotes the number of steps along side 3, while n is the number of steps along side 1 or 2 (if $n > 0$, it is side 1, if $n < 0$, it is side 2). (E) Any tubule is identified by an index pair, (m, n) . V-tubule and X-tubule, corresponding to $(5,0)$ and $(10,0)$, are achiral tubules with 5 and 10 triangles in circumference, respectively. Tubules of varying width and chirality can be assembled by tuning the magnitudes of the dihedral angles ϕ_1 , ϕ_2 , and ϕ_3 .

of three bevel angles, the width, handedness, and pitch of the resulting tubules can be programmed using these three angles alone. Indeed, the final tubule structure is equivalent to the equilateral Yoshimura pattern of a buckled cylindrical shell [24], which constitutes a class of origami tilings of cylinders via a single triangular facet with a single set of fold angles on its three edges. In the case of tubules, larger dihedral angles in the direction perpendicular to the tubule axis produce wider tubules.

Furthermore, setting the dihedral angles of sides 1 and 2 to different values produces chiral tubules with different pitch and handedness (Fig. 1E). The relative magnitude of the two dihedral angles determines the handedness and the difference between the two angles determines the pitch, with a larger difference leading to a larger pitch. Thus, by tuning the dihedral angles of the three sides, we can assemble a variety of different tubule structures. We note that the ability to program any tubule geometry using a single triangular facet is in contrast to the ability to program assembly of an icosahedral shell, for example, which requires a larger and larger number of unique facets upon increasing the shell diameter [1, 20].

The resulting tubules can be uniquely classified using a pair of lattice indices, (m, n) [25]. Here, m refers to vector along side 3 of the triangle and n refers to the vector along side 1 ($n > 0$) or side 2 ($n < 0$). Therefore, (m, n) defines the shortest distance along the triangular lattice to go around the tubule and come back to the same vertex. Note that we only consider the case $m \geq |n|$. With our convention, we use the positive index n to define right-handed tubules and the negative index n for left-handed tubules. Each tubule type is associated with a different set of dihedral angles for the three sides.

B. Tubule assembly

To demonstrate the utility of our experimental approach, we design two different monomers that assemble into tubules with different widths: V-triangle, which targets a (5,0) tubule, and X-triangle¹, which targets a (10,0) tubule (Fig. 2A). Each side of the triangle has a cross-section that is 4-by-6 double helices arranged on a square lattice (Fig. S3A). We specify the three unique bevel angles required for a particular tubule geometry by varying the relative lengths of the double helices (Fig. S3B). We encode the specific shapes of the protrusions and recesses by designing the scaffold routing, which we choose to disallow off-target binding and to enforce the correct relative orientations of neighboring subunits. The size of the subunits is set by the length of the DNA scaffold, which is 8064-nucleotides long. See Supplementary Information III for details of the subunit design.

We fold, purify, and assemble the subunits using standard DNA origami protocols. In brief, we fold the origami using a slow, linear temperature ramp, purify the resulting monomers by gel extraction, and then assemble them at constant temperature for one week in a rotating incubator [26] (see Supplementary Information V). For a given design, we perform multiple assembly experiments at different concentrations of MgCl_2 to tune

the strength of the intersubunit attraction. Finally, we characterize the structures of the individual monomers using single-particle cryogenic electron microscopy (cryo-EM) [27] and the entire assemblies using negative-stain transmission electron microscopy (TEM).

The bevel angles of the folded monomers are close to the target values but do not match them exactly. By fitting a pseudo-atomic model to our cryo-EM reconstructions [28] we make an estimate of the bevel angles of each of the three sides for both of our monomers (Fig. 2A). We find that for the V-triangle the three sides have angles of $(21.3 \pm 0.1, 21.3 \pm 0.1, -5.5 \pm 0.1)$ compared with the target angles of $(20.9, 20.9, -10.8)$. Comparing these angles to the angles of different tubule types, this monomer is closest to a (5,0) tubule, as designed. In contrast, for the X-triangle, we see monomer bevel angles of $(11.4 \pm 0.1, 9.0 \pm 0.1, -6.4 \pm 0.1)$ compared with $(10.4, 10.4, -5.3)$, yielding a closest state of a (9, -1) tubule. While the (9, -1) tubule has a similar diameter to the (10,0) one, it is chiral and left-handed rather than achiral, as in the designed monomer. See Supplementary Information VIII for more detail on the cryo-EM reconstructions.

The assembly of the triangular subunits into self-limiting structures depends on the intersubunit attraction, which can be controlled by varying the concentration of MgCl_2 . For both designs, we observe the same sequence of outcomes upon increasing the Mg^{2+} concentration (Fig. 2B). At low Mg^{2+} concentration, we observe only monomers and oligomers containing a few subunits. At intermediate Mg^{2+} concentration, we see the assembly of filament-like, self-limited structures in coexistence with monomers. The fact that we observe the coexistence of assemblies and monomers suggests that assembly occurred near to equilibrium and that the assembled filaments likely grew by consuming monomers rather than the merging of clusters. At higher Mg^{2+} concentrations, we observe large disordered aggregates and rarely observe monomers or small clusters. Therefore, we hypothesize that these large aggregates are likely due to kinetic arrest [29]. These results are consistent with previous measurements of the stacking interactions between blunt ends, which show that the interactions become stronger upon increasing Mg^{2+} concentration [30].

TEM tomography confirms that the filament-like structures are indeed tubules. First, we observe a single filament assembled from V-triangles (Fig. 2C). Looking at different slices through the filament in the direction normal to the EM grid, or z -stack, we see that the structure clearly shows two triangular lattices at different z positions, separated by a hollow core. The distance between the top and bottom lattices is around 40 nm, which is shorter than the expected diameter of 88 nm, but longer than 20 nm, or twice the thickness of a triangle. Therefore, we hypothesize that the cross-section of the tubule deposited on grid is elliptical. Finally, we also see that the top and bottom lattices have different orientations of the triangular lattice with respect to one

¹ Roman numerals V and X are used as shorthand for the target tubule types (5,0) and (10,0) respectively.

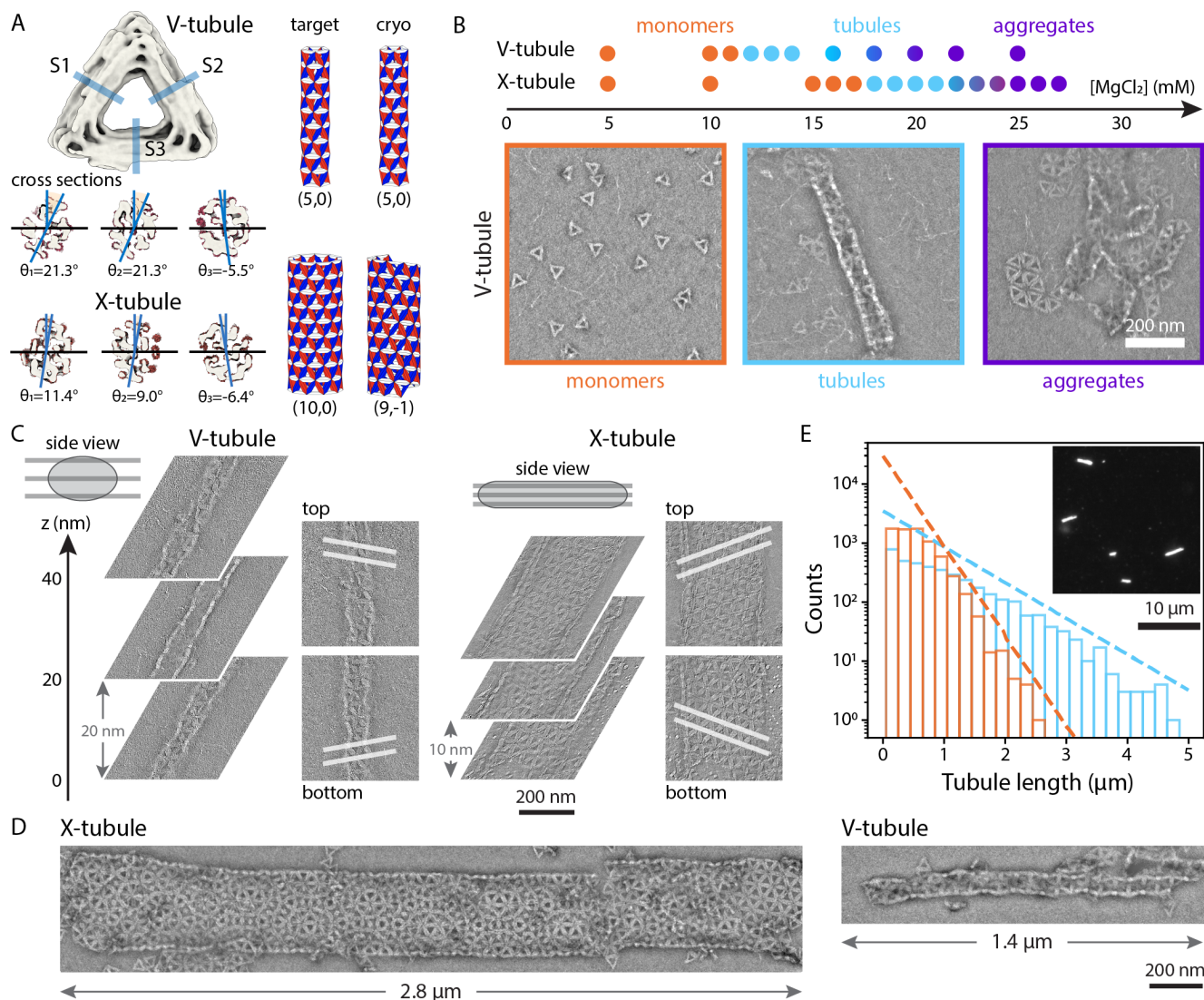


FIG. 2. Self-assembly of tubules. (A) Cryo-EM single-particle reconstructions for V-triangle and X-triangle. The figure shows cross-sections of three sides of the triangles (gray) and the estimated bevel angles, θ , from fitting the cryo-EM reconstruction to a pseudo-atomic model (maroon) (see Supplementary Information V). Tubule illustrations show the target geometry (labeled target) and the expected tubule geometry based on our cryo-EM measurements (labeled cryo) for the V-tubule and X-tubule. (B) Negative-stain transmission electron micrographs of V-triangles after incubation at different MgCl_2 concentrations for a week at 40°C . The points above the images show the MgCl_2 concentrations that lead to assembly of monomers (orange), tubules (cyan), or aggregates (purple). (C) Tomography reconstructions of the V- and X-tubules, showing different z positions. The orientation of side 3 is illustrated with white lines. (D) Images of tubules observed with V-triangles (right) and X-triangles (left). For the X-tubule one can see a Moiré pattern where the tubule has closed on itself. (E) Histograms of the tubule length observed with epi-fluorescence for V-tubules (orange) and X-tubules (cyan). Dashed lines are guides for the eye to highlight the exponential decay in length (see Supplementary Information VII A). The inset shows an example fluorescence image.

another, as would be expected for a chiral tubule. Taken together, these observations confirm that the filament is indeed a tubule. Going further, the lattice orientation can be tracked around the tubule, yielding a (4,1) tubule for this case. While this determination only gives us the magnitude of n , we also determine the handedness by comparing our reconstructions to reconstructions of a DNA origami nanohelix labeled with gold nanoparticles

in a right-handed, chiral arrangement (see Supplementary Information VII B) [31, 32].

Similarly, we find that the wider filaments formed from X-triangles are also tubules. As with the V-triangles, the tomograms of the wide filaments show two triangular lattices, which are mirror images of one another, and spaced apart along the z direction. In this case, the distance between the bottom and the top lattices is around 20 nm,

which matches the height of two triangles. We suspect that this spacing is due to the flattening of the X-tubule during the sample preparation. This hypothesis is further supported by the observation that the two triangular lattices appear to be planar, as expected for a flattened tubule. Finally, similar to the example V-tubule, the specific X-tubule shown in Fig. 2C is also chiral and right-handed, as seen in the mirror reflection of the top and bottom lattices (see Supplementary Information VII B).

Remarkably, we find that both V-tubules and X-tubules can grow to micrometers in length and exhibit length distributions that are characteristic of equilibrium one-dimensional growth. Figure 2D shows examples of some of the longest tubules that we observe in electron microscopy for both designs. The V-tubule is roughly 1200 nanometers in length and is made from about 210 subunits. The X-tubule is nearly 3 micrometers long and is assembled from about 1400 subunits. To complement our EM observations, we also perform epi-fluorescence experiments to get a more complete view of the tubule lengths (Fig. 2E, see Supplementary Information VII A for details). We find that both V- and X-tubules are characterized by length distributions that decay exponentially, with means of 0.5 micrometers and 0.9 micrometers, respectively, which is consistent with expectations for equilibrium one-dimensional assembly [33]. In the extremes, we find assemblies reaching up to 5 micrometers in length. Comparing our X-tubule results to earlier attempts to assemble tubules of similar width from DNA origami subunits [19] shows that our approach yields assemblies that are roughly an order of magnitude longer and contain about five times the number of subunits. Furthermore, our results show that although the width of the tubule is self-limited, the tubule lengths are unconstrained.

C. Tubule distributions

Whereas the results above show the structure of single tubules, our assembly experiments yield an ensemble of tubules that exhibits a variety of widths and lattice orientations, despite being formed from a single monomer type. For both the V- and X-tubule designs, we identify the pair of indices (m, n) that classifies the structure for each of hundreds of individual tubules, and create a distribution (Fig. 3A). The distribution shows that the most probable tubule types are $(4,0)$ and $(9,4)$ for the V- and X-tubules respectively, with the probability of different states falling off with distance from this tubule type. Furthermore, we find that the breadth of the X-tubule distribution is larger than that of the V-tubule. Although we cannot easily determine the chirality of every tubule, we examined 13 chiral V-tubules and 15 chiral X-tubules using tomography. In both cases, all of the tubules that we examined were right-handed. See the Supplementary Information VII B and VII C for a detailed description

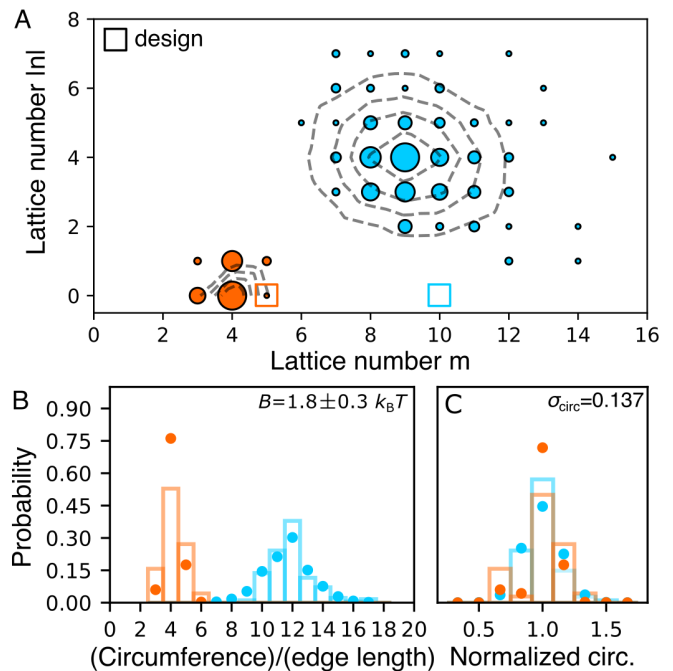


FIG. 3. **Measured distributions of the lattice numbers of observed tubules** (A) Lattice number distribution of the two tubules. The size of each circle is proportional to the number of tubules found for that lattice number. Orange represents data for the V-tubule, while cyan represents data for the X-tubule. The square symbols denote the target states. Contours show the expected spread based on model predictions, described in the text, where the spacing between contours is 20% of the peak probability. The plot shows distribution from $N=70$ and $N=182$ tubules for V- and X-tubules, respectively. (B) Histograms of the measured circumferences of the tubules. Points come from a model prediction using a bending rigidity of $B = 1.8 \pm 0.3 k_B T$; bars show experimental data. (C) The corresponding distributions of the circumferences normalized by the mean, whose variance, σ_{circ}^2 , is used to estimate B . $\sigma_{\text{circ}} = 0.137$ is the average of the standard deviations obtained from the V- and X- tubule distributions.

of the tubule classification.

The observed distributions beg two important questions: 1) Why are the tubule distributions not centered around the target structures? and 2) What determines the breadth of the tubule distribution around the most probable tubule type? We address the first question by returning to our single-particle reconstructions of the monomers from cryo-EM (Fig. 2A). While the V-triangle estimates a state close to the peak of the experimental distribution, the X-triangle estimate is 13% narrower in width than the $(9,4)$ peak that we observe. We note that the cryo-EM map of the X-triangle shows that some parts of the lock-and-key design protrude from the structure due to a missed crossover in the origami design (Fig. S16). Therefore, we hypothesize that this aspect of the structure causes a poor fit for the lock-and-key shapes of the interaction, leading to unintended torques

that could skew the dihedral angles to a different value. This misfit would cause a shift in the mean of the distribution away from what is expected from the geometry of the monomer alone.

Next, we tackle the origin of the breadth of the distribution. We start by noting that tubules with neighboring lattice numbers only vary by small changes in their dihedral angles. Therefore, if the bending rigidity of the assembly is sufficiently small, thermal fluctuations will cause the dihedral angles between neighboring triangles to explore a range of possible values, leading to tubules with larger or smaller diameters.

This idea can be captured by considering the Helfrich energy of an elastic sheet, $E_H = \frac{1}{2}BA(\Delta\kappa_\perp)^2$ where A is the surface area, B is the bending rigidity, and $\Delta\kappa_\perp$ is the fluctuation of the sheet's curvature in the circumferential direction [34]. We assume that as the assemblies grow, they must first form a patch-like circular sheet before closing into a tubule. Thermal fluctuations will cause this sheet to accommodate different curvatures from its preferred value, but once it grows large enough to close into a tubule we assume that it can not open into a sheet again, thereby locking in a specific tubule circumference. If the growth rate is faster than the dissociation of a subunit-subunit bond, then once a tubule forms and starts to grow, the possibility of opening a large number of bonds to allow the tubule to reform into a different type becomes increasingly unlikely. Therefore, we estimate the size of assemblies at this closure point as a disk with a diameter that corresponds to the circumference of the closed tubule. The fluctuations of the sheet's curvature at the point of closure will inherently lead to a distribution of tubule circumferences. Under these assumptions, we can write the Helfrich energy for a tubule at closure as

$$E_H = \frac{1}{2}B\pi^3 \left(\frac{\Delta C}{C}\right)^2 \quad (1)$$

where C is the circumference of a tubule. Assuming that the circumferences follow a Boltzmann distribution, $P \sim \exp(-E_H/k_B T)$, we can relate the spread of the widths to the bending rigidity ([22], see Supplementary Information IX for details).

The predictions from the Helfrich energy are consistent with our experimental observations, suggesting that the width distribution is determined by the bending rigidity of the growing assembly and the irreversibility of closure. Figure 3B shows the distribution of the tubule circumference for both V- and X-tubules. Following the insight we gained from considering the Helfrich energy, we rescale the circumference by the mean circumference of each distribution. Figure 3C shows that for both V- and X-tubules the scaled distributions have similar breadths, with standard deviations of 0.149 and 0.125, respectively. The importance of this observation is that it is an inherent feature of self-closing assemblies at finite temperature: Whenever the assembly has a finite bending rigidity, the system will form a distribution of end states with

a breadth that depends on the self-limited length scale relative to the size of the subunit.

Using the variance of the width distributions, we make an estimate of the bending rigidity of the V- and X-tubules. Assuming both assemblies have the same bending rigidity, we find $B = 1.8 \pm 0.3 k_B T$. To our knowledge, this is the first estimate of bending rigidity of shape-complementary interactions in DNA origami. Moreover, we can use this bending rigidity as an input to perform more detailed energetics calculations (see Supplementary Information IX) to get a complete (m, n) distribution for the expected tubules [22], which is shown in the contours of Fig. 3A. Similarly, we can compute the circumference distributions for the model. In both cases, we find that our model predictions match the experimental data well (Fig. 3B), further supporting the idea that the distribution of tubules we observe in the experiment is due to finite bending rigidity and is therefore expected for self-closing structures.

D. Pruning the tubule distribution by increasing the assembly complexity

Our observations of the X-tubule assembly highlight an inherent challenge in using self-closing assembly alone to target finite-sized soft materials: As we target larger self-closing lengths, the distribution of the self-limited dimension also gets broader. So how do we overcome this challenge to assemble wider tubules without compromising the accuracy of the assembly?

Here we turn our attention toward the other paradigm for encoding self-limitation: addressable assembly. The rationale of this approach is relatively easy to understand. By increasing the number of particle species per structure, and therefore the total number of specific interactions, the location of any given particle within that structure becomes more precisely defined. In the fully-addressable limit, each particle species can only occupy a single position within the final structure while simultaneously maximizing the number of its favorable interactions. Therefore, by eliminating the other ways in which the particles can be arranged, the yield of the target assembly can be increased.

We explore this approach by assembling a (10,0) tubule from two unique species of triangular subunits. Figure 4 shows our specific realization of this concept using a binary tiling that is compatible with tubule self-assembly (Fig. 4A, see Supplementary Information IV). The two species are placed periodically and unidirectionally in the pattern. Since each side encodes a specific dihedral angle, the sides must always remain in the same orientation. As before, a triangular lattice of these two species can be rolled up into a (10,0) tubule. However, unlike before, the binary lattice contains two distinct types of vertices. As a result, the assembled tubules have an additional constraint: When the triangular lattice closes to form a tubule, the closing vertices must match. There-

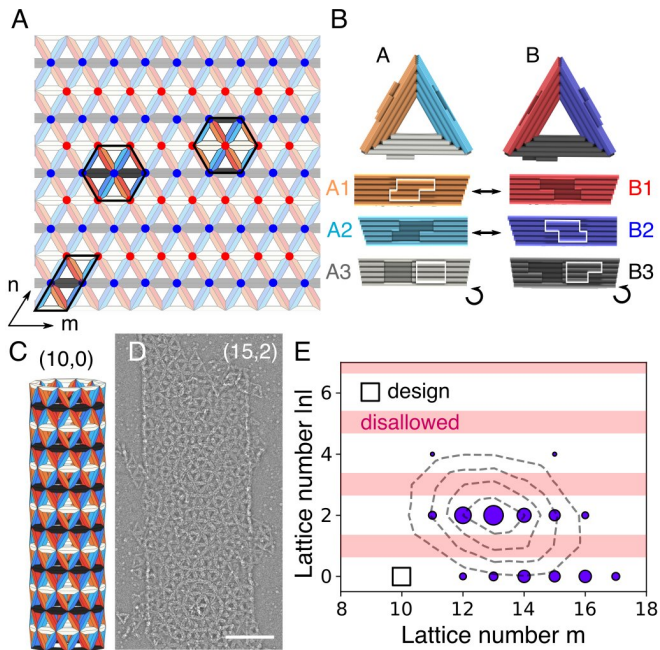


FIG. 4. **Schematics for binary species tubules and their lattice number distributions** (A) Triangular tiling using two types of monomers. The highlighted region in the lower left shows the primitive cell of the tiling. Red and blue dots denote the two distinct vertices present in the pattern, which are highlighted as well. (B) Schematic representation of the two types of monomers we use to construct the tubule. Black arrows represent the binding pairs of the lock-and-key interactions. (C) Diagram of the intended (10,0) tubule structure. (D) Negative-stain TEM micrograph of a tubule made from the two species, whose tubule type is (15,2). The scale bar is 200 nm. (E) Tubule type distribution of the binary mixture. The size of each circle is proportional to the number of tubules found for that pair of lattice indices. The square symbol denotes the target state. Contours show the expected spread based on model predictions with $B = 3.1 k_B T$, where the spacing between contours is 20% of the peak probability. This B value is estimated in the same manner as described previously. Red regions are disallowed due to the tiling pattern of the binary species, as seen in the experiments. The plot shows distribution from $N=113$ tubules.

fore, for our specific case, we expect that only tubules with an even lattice number n can assemble. The specific implementation of the lock-and-key geometries and their interactions is shown in Fig. 4B and the expected assembly is shown in Fig. 4C.

The distribution of assembled tubules demonstrates that increasing the assembly complexity limits the accessible states. Figure 4D shows an example tubule and Fig. 4E is the tubule distribution that we measure. We find that the distribution is maximal at (13,2), with some tubules being chiral and others achiral. All 7 tomography reconstructions of chiral tubules were identified to be right-handed (see Supplementary Information VII B). Most importantly, we do not find a single tubule classified by an odd value of n , as we intended by our design. We

also find that the probability of the most common state is increased compared to what it would be with a single particle type. The binary assembly has a larger average circumference than the X-tubule, which would suggest that the probability for the most common state would be comparatively lower. However, we find that the most populated state for the binary assembly is 22.1% compared to 17.6% for the X-tubule. This increase in probability is a result of using more species of triangles for the assembly since some fraction of tubules that might have had an odd n are distributed to nearby even n states.

As before, although the distribution is not centered around the target state, it has a width that is consistent with our energetics model. We hypothesize that the shift in the center of the distribution is again due to the experimental design challenge of accurately encoding the dihedral angles in our DNA origami subunits. The bevel angles of the triangles are designed to target X-tubules, similar to the previous case. However, cryo-EM reconstructions of the individual subunits reveal bevel angles that would target a (13,-1) tubule (see Supplementary Information VIII).

CONCLUSION

In summary, we devised a new class of colloidal particles using DNA origami and studied the roles of geometry and interaction complexity in their self-limited assembly into tubules. Our DNA origami design scheme allows for control over the valence, interaction specificity, and local curvature of the subunits, independently. We demonstrate that the new DNA origami colloids enable the assembly of complex structures, such as tubules, with self-limited dimensions that are much larger than the individual subunits. Using this design principle, we designed and assembled tubules of different widths, demonstrating that information encoded in the geometry of individual subunits can be used to program the geometry of the entire assembly. However, due to the intrinsic flexibility of the binding, tubules with a variety of widths and chiralities assembled from the same subunits, which was especially prominent for wider tubules. Such a distribution of assembled tubules for a single monomer type is an inherent feature of bending fluctuations in curvature-limited assemblies.

Here, we experimentally demonstrated one path toward removing off-target structures to focus the distribution on the target of interest. The precision in reaching a specific state can be increased by combining *interaction specificity* with *geometric specificity* in a multi-species design. As one specific realization of this concept, we assembled tubules using two species of subunits, which effectively reduced the number of accessible states by half. Therefore, as more species of subunits are added to the system, we anticipate that the yield of the target state will increase, though likely at the cost of longer timescales for assembly [22]. Another possibility other than *interac-*

tion specificity that follows from our observations is that one can exploit the *geometric specificity* of the system to mitigate the formation of off-target structures. For example, designing ever more rigid binding sites should increase the energetic cost to deform the structure away from the target geometry. While it is not clear how much control there is over this aspect given the material properties of the subunits themselves, one might expect the bending rigidity to vary with the particle aspect ratio (i.e. thickness to width) based on elastic considerations alone. Finally, Nature, confronted with the same design challenge of assembling tubules from few components, has evolved a third strategy for eliminating off-target states: employing seeded nucleation, as seen with the *in vivo* assembly of microtubules [2, 35, 36]. Thus, if one can tune the supersaturation level to avoid spurious nucleation while still allowing for growth by monomer addition, having templates off of which tubules grow would improve the specificity of a given target structure without impeding the kinetics [17].

A somewhat surprising result of the origami design is how different the bevel angles of the three different versions of the X-triangle are (see Supplementary Information Table IV). Even though all three of these structures were constructed using the same design principle, resulting in the same length of scaffold strands for each helix, this approach did not result in the same bevel angles for the different sides. One main difference is that the crossover connections between helices had to be placed in different locations to accommodate the different lock-and-key designs. This subtle change may cause unintended torsion within the sides that impact the relative angles of adjacent sides. One avenue to address this issue would be to use interior supporting struts to add additional length constraints to the system. Another possible issue is that the short (one to three base pairs) single-stranded DNA segments connecting helices at the vertices might over constrain the vertices and add stress to the subunit. A design modification that might avoid this issue is to only connect the sides at the vertices in a few locations. Lastly, it seems prudent to use existing simulation software, such as oxDNA [37], ENRG MD [38], and mrdna [39] to screen different arrangements of crossovers to find ones that yield the desired bevel angles.

Overall, our DNA origami colloids represent a powerful platform for programming the assembly of self-limiting architectures. We argue that our ability to program the local curvature with the precision of a few degrees per subunit opens up new directions in materials design that surpass what is currently possible. Whereas tubules assembled from DNA tiles are made from ‘floppy’ components and therefore prescribed mainly by the *interaction specificity* encoded in the tile sequences [13–16], our tubule structures can be programmed by both *interaction specificity* and *geometrical specificity*. As we showed, these two paradigms can play important complementary roles in self-limited assembly. Geometric specificity can enable economical designs that require only a few sub-

unit species and interaction specificity can improve the accuracy of assembly by eliminating off-target structures. Therefore, going forward, we anticipate that being able to prescribe both mechanisms of self-limited assembly will allow access to a new library of self-assembled structures with interesting material applications. Examples include 2D lattice-like membranes for patterning or separations [18, 40], spherical shells for encapsulation and delivery [20], fibers or length-limited tubules through geometrical frustration [41, 42], and three-dimensional 3D periodic structures for structural coloration [43].

MATERIALS AND METHODS

Brief descriptions of our experimental methods are provided below. For more detailed methods see the Supplementary Information I.

Assembly of triangular subunits

DNA origami subunits are assembled in a one-pot reaction with 50 nM of p8064 scaffold DNA (Tilbit) and 200 nM of each staple strand (IDT, see Supplementary Information for sequences) in a standard ‘folding buffer’. Standard ‘folding buffers’, described previously [26], contain X mM MgCl_2 , 5 mM Tris base, 1 mM EDTA, and 5 mM NaCl (FoBX). Reaction solutions are subjected to a thermal annealing cycle in a Tetrad (Bio-Rad) thermocycler. Optimal MgCl_2 concentrations and annealing protocols are described in Supplementary Information Table S1.

Purification of subunits

All origami subunits are purified by gel extraction and concentrated by ultrafiltration. We use a 1.5% agarose gel with 0.5XTBE buffer, 5.5 mM MgCl_2 , and 0.5x SYBR-safe (Invitrogen). Custom-made gel combs that can hold 0.2 ml per well were used to increase the throughput. The folded solution is mixed 5:1 with loading dye (30% w/v Ficoll 400, 0.1% w/v bromophenol blue, 3xTBE) and run at 110V for 2 hours. We remove the monomer band with a razor blade and dice it into small pieces. Gel pieces are placed in a Freeze 'N Squeeze spin column (Bio-Rad) and kept at -20°C for 5 minutes, then spun down for 5 minutes at 13 krcf. The supernatant is concentrated by ultrafiltration with 0.5 ml Amicon 100 kDa filters. Amicon filters are first equilibrated by centrifuging down 0.5 ml of 1xFoB5 at 5 krcf for 7 minutes, after which the flow-through is removed. The DNA origami solution is added up to 0.5 ml and centrifuged at 14 krcf for 15 minutes, then the flow-through is removed. This process is repeated until all of the DNA origami solution has been filtered. Finally, we place the filter upside down over a new Amicon tube and centrifuge at 1

krcf for 2 minutes. The DNA origami concentration of the final solution is measured using a Nanodrop (Thermo Scientific).

Self-assembly of tubules

Purified subunits are assembled in 50 μl mixtures of 1xFoBX with a monomer concentration of 10 nM. The MgCl_2 concentration (X) is varied from 5 to 30 mM. The assembly solution is pipetted into a capped 0.1 ml strip tube (Rotor-Gene), which is subsequently placed into a 0.2 ml strip tube (Corning) to suppress evaporation and condensation within the tube. Tubes are loaded into a rotating incubator (Roto-Therm, Benchmark Scientific) at 40° C for a week.

Negative stain TEM

Assembly samples are incubated on glow-discharged FCF400-Cu TEM grids (Electron Microscopy Sciences) for 60–120 s. Grids are then stained with 2% aqueous uranyl formate solution with 20 mM NaOH for up to 30 s before blotting on filter paper and using vacuum suction to remove excess fluid. Images of the grids are acquired on an FEI Morgagni TEM operated at 80 kV with a Nanosprint5 CMOS camera (AMT) at magnifications between x8000 and x20000. Tomograms of grid samples are acquired on a Tecnai F20 TEM with an FEG run at 200kV with a Gatan Ultrascan 4kx4k CCD camera. Tilt series were observed at a magnification of x32000 from -50° to 50° in 2° increments. Subsequent analysis is performed using Etomo (IMOD [44]).

Cryo-electron microscopy

Higher concentrations of DNA origami are used to prepare cryo-EM grids, summarized in SI Table S3. Samples are placed on glow-discharged C-flat 1.2/1.3 400 mesh grids (Protochip). Plunge-freezing of the grids in liquid ethane is performed with an FEI Vitrobot with sample volumes of 3 μl , blot times of 5–8 s, a blot force of -1, and a drain time of 0 s at 20° C and 95% humidity. All cryo-EM images were acquired with a Tecnai F30 TEM with the field emission gun electron source operated at 300kV and equipped with an FEI Falcon II direct electron detector at a magnification of x39000. Single-particle acquisition was performed with SerialEM. The defocus

was set to -2 μm for all acquisitions with a pixel size of 2.87 Angstrom.

Image processing was performed using RELION-3 [27]. Contrast-transfer-function (CTF) estimation was performed using CTFFIND4.1 [45]. After picking single particles we performed a reference-free 2D classification from which the best 2D class averages were selected for processing, estimated by visual inspection. The particles in these 2D class averages were used to calculate an initial 3D model. A single round of 3D classification was used to remove heterogeneous monomers and the remaining particles were used for 3D auto-refinement and post-processing. A summary of the cryo-EM reconstructions is shown in SI Table S3.

Epi-fluorescence imaging of tubules

To dye our samples, we incubate our assemblies with YOYO-1 dye (Invitrogen) at room temperature for at least half an hour in a solution of 5 nM DNA origami, 500 nM YOYO-1 dye, and 1xFoB, at the same MgCl_2 concentration as that of the assembly. We pipette 1.6 μl of the solution onto a microscope slide that has been cleaned with Alconox, ethanol (90%), acetone, deionized water, and subsequently plasma-cleaned. After deposition, a plasma-cleaned coverslip is placed on top to create a thin liquid layer. Samples are then imaged on a TE2000 Nikon inverted microscope with a Blackfly USB3 (FLIR) camera.

ACKNOWLEDGMENTS

We acknowledge Don Caspar for sparking an interest in the self-assembly of cylindrical tubules. We thank Botond Tyukodi and Farzaneh Mohajerani for helpful discussions, Thomas Gerling for experimental support, Ali Aghvami, Mike Rigney, and Berith Isaac, for technical support with electron microscopy. TEM images were prepared and imaged at the Brandeis Electron Microscopy facility. This work is supported by the Brandeis University Materials Research Science and Engineering Center, which is funded by the National Science Foundation under award number DMR-2011846. D.H. acknowledges support from the Masason Foundation. D.H., D.M.H., S.F., M.F.H., G.M.G., and W.B.R. conceived the research. D.H. and T.E.V. performed experiments. D.H., T.E.V, H.F., and E.F. analyzed the data. D.H., D.M.H., C.S., and H.D. designed the particles. All authors contributed to writing the manuscript.

[1] D. L. D. Caspar and A. Klug, Physical Principles in the Construction of Regular Viruses, Cold Spring Harbor Symposia on Quantitative Biology **27**, 1 (1962).

[2] H. Sui and K. H. Downing, Structural Basis of Interprotofilament Interaction and Lateral Deformation of Microtubules, Structure **18**, 1022 (2010).

- [3] B. T. Wimberly, D. E. Brodersen, W. M. C. Jr, R. J. Morgan-Warren, A. P. Carter, C. Vornrhein, and T. Hartsch, Structure of the 30S ribosomal subunit, *Nature* **407**, 327 (2000).
- [4] R. J. Macfarlane, B. Lee, M. R. Jones, N. Harris, G. C. Schatz, and C. A. Mirkin, Nanoparticle Superlattice Engineering with DNA, *Science* **334**, 204 (2011).
- [5] W. B. Rogers, W. M. Shih, and V. N. Manoharan, Using dna to program the self-assembly of colloidal nanoparticles and microparticles, *Nature Reviews Materials* **1**, 1 (2016).
- [6] H. Fang, M. F. Hagan, and W. B. Rogers, Two-step crystallization and solid–solid transitions in binary colloidal mixtures, *Proceedings of the National Academy of Sciences* **117**, 27927 (2020).
- [7] M. He, J. P. Gales, E. Ducrot, Z. Gong, G.-R. Yi, S. Sacanna, and D. J. Pine, Colloidal diamond, *Nature* **585**, 524 (2020).
- [8] M. F. Hagan and G. M. Grason, Equilibrium mechanisms of self-limiting assembly, *Rev. Mod. Phys.* **93**, 025008 (2021).
- [9] Z. Zeravcic, V. N. Manoharan, and M. P. Brenner, Size limits of self-assembled colloidal structures made using specific interactions, *Proceedings of the National Academy of Sciences* **111**, 15918 (2014).
- [10] W. M. Jacobs, A. Reinhardt, and D. Frenkel, Rational design of self-assembly pathways for complex multicomponent structures, *Proceedings of the National Academy of Sciences* **112**, 6313 (2015).
- [11] Y. Ke, L. L. Ong, W. Sun, J. Song, M. Dong, W. M. Shih, and P. Yin, DNA brick crystals with prescribed depths, *Nature Chemistry* **6**, 994 (2014).
- [12] J. D. Halverson and A. V. Tkachenko, Dna-programmed mesoscopic architecture, *Physical Review E* **87**, 062310 (2013).
- [13] P. W. K. Rothmund, A. Ekani-Nkodo, N. Papadakis, A. Kumar, D. K. Fygenson, and E. Winfree, Design and Characterization of Programmable DNA Nanotubes, *Journal of the American Chemical Society* **126**, 16344 (2004).
- [14] P. Yin, R. F. Hariadi, S. Sahu, H. M. T. Choi, S. H. Park, T. H. LaBean, and J. H. Reif, Programming DNA Tube Circumferences, *Science* **321**, 824 (2008).
- [15] B. Wei, M. Dai, and P. Yin, Complex shapes self-assembled from single-stranded DNA tiles, *Nature* **485**, 623 (2012).
- [16] H. Shen, J. A. Fallas, E. Lynch, W. Sheffler, B. Parry, N. Jannetty, J. Decarreau, M. Wagenbach, J. J. Vicente, J. Chen, L. Wang, Q. Dowling, G. Oberdorfer, L. Stewart, L. Wordeman, J. De Yoreo, C. Jacobs-Wagner, J. Kollman, and D. Baker, De novo design of self-assembling helical protein filaments, *Science* **362**, 705 (2018).
- [17] A. M. Mohammed and R. Schulman, Directing self-assembly of dna nanotubes using programmable seeds, *Nano letters* **13**, 4006 (2013).
- [18] G. Tikhomirov, P. Petersen, and L. Qian, Programmable disorder in random DNA tilings, *Nature Nanotechnology* **12**, 251 (2017).
- [19] K. F. Wagenbauer, C. Sigl, and H. Dietz, Gigadalton-scale shape-programmable DNA assemblies, *Nature* **552**, 78 (2017).
- [20] C. Sigl, E. M. Willner, W. Engelen, J. A. Kretzmann, K. Sachenbacher, A. Liedl, F. Kolbe, F. Wilsch, S. A. Aghvami, U. Protzer, M. F. Hagan, S. Fraden, and H. Dietz, Programmable icosahedral shell system for virus trapping, *Nature Materials* **20**, 1281 (2021).
- [21] J. B. Bale, S. Gonen, Y. Liu, W. Sheffler, D. Ellis, C. Thomas, D. Cascio, T. O. Yeates, T. Gonen, N. P. King, and D. Baker, Accurate design of megadalton-scale two-component icosahedral protein complexes, *Science* **353**, 389 (2016).
- [22] T. E. Videbæk, H. Fang, D. Hayakawa, B. Tyukodi, M. F. Hagan, and W. B. Rogers, Tiling a tubule: how increasing complexity improves the yield of self-limited assembly, *J. Phys.: Condens. Matter* **34**, 134003 (2022).
- [23] T. Gerling, K. F. Wagenbauer, A. M. Neuner, and H. Dietz, Dynamic DNA devices and assemblies formed by shape-complementary, non–base pairing 3D components, *Science* **347**, 1446 (2015).
- [24] Y. Yoshimura, *On the mechanism of buckling of a circular cylindrical shell under axial compression*, Tech. Rep. (1955).
- [25] R. K. F. Lee, B. J. Cox, and J. M. Hill, An exact polyhedral model for boron nanotubes, *J. Phys. A: Math. Theor.* **42**, 065204 (2009).
- [26] K. F. Wagenbauer, F. A. S. Engelhardt, E. Stahl, V. K. Hecht, P. Stömmer, F. Seebacher, L. Meregalli, P. Ketterer, T. Gerling, and H. Dietz, How We Make DNA Origami, *ChemBioChem* **18**, 1873 (2017).
- [27] J. Zivanov, T. Nakane, B. O. Forsberg, D. Kimanius, W. J. Hagen, E. Lindahl, and S. H. Scheres, New tools for automated high-resolution cryo-em structure determination in relion-3, *eLife* **7**, e42166 (2018).
- [28] M. Kube, F. Kohler, E. Feigl, B. Nagel-Yüksel, E. M. Willner, J. J. Funke, T. Gerling, P. Stömmer, M. N. Honemann, T. G. Martin, *et al.*, Revealing the structures of megadalton-scale dna complexes with nucleotide resolution, *Nature Communications* **11**, 1 (2020).
- [29] S. Whitelam and R. L. Jack, The Statistical Mechanics of Dynamic Pathways to Self-Assembly, *Annu. Rev. Phys. Chem.* **66**, 143 (2015).
- [30] F. Kilchherr, C. Wachauf, B. Pelz, M. Rief, M. Zacharias, and H. Dietz, Single-molecule dissection of stacking forces in DNA, *Science* **353**, aaf5508 (2016).
- [31] A. Kuzyk, R. Schreiber, Z. Fan, G. Pardatscher, E.-M. Roller, A. Högele, F. C. Simmel, A. O. Govorov, and T. Liedl, DNA-based self-assembly of chiral plasmonic nanostructures with tailored optical response, *Nature* **483**, 311 (2012).
- [32] A. Briegel, M. Pilhofer, D. N. Mastrorade, and G. J. Jensen, The challenge of determining handedness in electron tomography and the use of DNA origami gold nanoparticle helices as molecular standards, *Journal of Structural Biology* **183**, 95 (2013).
- [33] R. Phillips, J. Kondev, J. Theriot, H. G. Garcia, and N. Orme, *Physical biology of the cell* (Garland Science, 2012).
- [34] W. Helfrich and J. Prost, Intrinsic bending force in anisotropic membranes made of chiral molecules, *Physical Review A* **38**, 3065 (1988).
- [35] D. Chrétien and R. H. Wade, New data on the microtubule surface lattice, *Biology of the Cell* **71**, 161 (1991).
- [36] J. Roostal and T. Surrey, Microtubule nucleation: beyond the template, *Nature Reviews Molecular Cell Biology* **18**, 702 (2017).
- [37] T. E. Ouldridge, A. A. Louis, and J. P. Doye, Structural, mechanical, and thermodynamic properties of a coarse-

- grained dna model, *The Journal of Chemical Physics* **134**, 02B627 (2011).
- [38] C. Maffeo, J. Yoo, and A. Aksimentiev, De novo reconstruction of DNA origami structures through atomistic molecular dynamics simulation, *Nucleic Acids Res.* **44**, 3013 (2016).
- [39] C. Maffeo and A. Aksimentiev, Mrdna: a multi-resolution model for predicting the structure and dynamics of dna systems, *Nucleic Acids Research* **48**, 5135 (2020).
- [40] J. A. Millan, D. Ortiz, G. v. Anders, and S. C. Glotzer, Self-Assembly of Archimedean Tilings with Enthalpically and Entropically Patchy Polygons (2014).
- [41] G. M. Grason, Perspective: Geometrically frustrated assemblies, *The Journal of Chemical Physics* **145**, 110901 (2016).
- [42] B. Tyukodi, F. Mohajerani, D. M. Hall, G. M. Grason, and M. F. Hagan, Thermodynamic size control in curvature-frustrated tubules: Self-limitation with open boundaries, arXiv:2109.01174 [cond-mat] (2021), arXiv: 2109.01174.
- [43] K. Michielsen and D. Stavenga, Gyroid cuticular structures in butterfly wing scales: biological photonic crystals, *Journal of The Royal Society Interface* **5**, 85 (2008).
- [44] J. R. Kremer, D. N. Mastrorarde, and J. R. McIntosh, Computer visualization of three-dimensional image data using IMOD, *Journal of Structural Biology* **116**, 71 (1996).
- [45] A. Rohou and N. Grigorieff, Ctffind4: Fast and accurate defocus estimation from electron micrographs, *Journal of Structural Biology* **192**, 216 (2015).

Supplemental Information for “Geometrically programmed self-assembly of tubules using DNA-origami colloids”

Daichi Hayakawa, Thomas E. Videbæk, Douglas M. Hall, Huang Fang, Christian Sigl, Elija Feigl, Hendrik Dietz, Seth Fraden, Michael F. Hagan, Gregory M. Grason, W. Benjamin Rogers

I. EXPERIMENTAL METHODS

A. Folding DNA origami

Each DNA origami particle is folded by mixing 50 nM of p8064 scaffold DNA (Tilibit) and 200 nM each of staple strands (IDT, see SI Tables VI – IX for the sequences) with folding buffer and run through an individually optimized annealing protocol. Our folding buffer, or FoBX, contains 5 mM Tris Base, 1 mM EDTA, 5 mM NaCl, and X mM $MgCl_2$. We use a Tetrad (Bio-Rad) thermocycler for annealing the solutions.

To find the optimal folding conditions, we screen a range of temperature ramps and $MgCl_2$ concentrations. We begin with a coarse screening over a wide range of temperature ramps and $MgCl_2$ concentrations: 20 mM $MgCl_2$ mixtures are folded with 4 hour temperature ramps for the eight temperature ranges 50-47°C to 64-61°C with 2°C increments in the starting temperature and stepping by 1°C per hour; 5, 10, 15, 20, 25, 30 mM $MgCl_2$ mixtures are folded with a 17 hour temperature ramp from 60-44°C. This initial screen narrows down which $MgCl_2$ concentration range and starting temperature for the annealing will produce the highest folding yield. Subsequent detailed screenings with annealing protocols ranging from 4-17 hour ramps and over a smaller range of $MgCl_2$ concentrations provide an optimal folding condition. The results of the folding screens and optimal conditions for each DNA origami particle are shown in SI Section V.

B. Agarose gel electrophoresis

To assess the outcome of folding, we separate the folding mixture using agarose gel electrophoresis. Gel electrophoresis requires the preparation of the gel and the buffer. The gel is prepared by heating a solution of 1.5% w/w agarose, 0.5x TBE to boiling in a microwave. The solution is cooled to 60 °C. At this point, we add $MgCl_2$ solution and SYBR-safe (Invitrogen) to adjust the concentration of the gel to 5.5 mM $MgCl_2$ and 0.5x SYBR-safe. The solution is then quickly cast into an Owl B2 gel cast, and further cooled to room temperature. The buffer solution contains 0.5x TBE and 5.5 mM $MgCl_2$, and is chilled to 4°C before use. Agarose gel electrophoresis is performed at 110 V for 1.5 to 2 hours in a cold room kept at 4°C. The gel is then scanned with a Typhoon FLA 9500 laser scanner (GE Healthcare) at 100 μ m resolution.

C. Gel purification and resuspension

After folding, DNA-origami particles are purified to remove all excess staples and misfolded aggregates using gel purification. The folded particles are run through an agarose gel (now at a 1xSYBR-safe concentration for visualization) using a custom gel comb, which can hold around 2 ml of solution per gel. We use a blue fluorescent table to identify the gel band containing the monomers. The monomer band is then extracted using a razor blade, which is further sliced into smaller pieces. We place the gel slices into a Freeze 'N Squeeze spin column (Bio-Rad), freeze it in a -20°C freezer for 5 minutes, and then spin the solution down for 3 minutes at 12 krcf. The concentration of the DNA-origami particles is measured using a Nanodrop (ThermoFisher), assuming that the solution consists only of monomers, where each monomer has 8064 base pairs.

Since the concentration of particles obtained after gel purification is typically not high enough for assembly, we concentrate the solution through ultrafiltration [1]. First, a 0.5 ml Amicon 100kDA ultrafiltration spin column is equilibrated by centrifuging down 0.5 ml of FoB5 buffer at 5 krcf for 7 minutes. Then, the DNA origami solution is added up to 0.5 ml and centrifuged at 14 krcf for 15 minutes. We remove the flow-through and repeat the process until all of the DNA origami solution is filtered. Finally, we flip the filter upside down into a new Amicon tube and spin down the solution at 1 krcf for 2 minutes. The concentration of the final DNA origami solution is then measured using a Nanodrop (Thermo Scientific).

D. Estimating the binding free energies between subunits

In this work, we also use gel electrophoresis to analyze the binding strengths between the sides of the triangles (see SI Section VI). Here, the conditions for gel electrophoresis are slightly different. In order to maintain the same binding strengths as the assembly conditions, the MgCl_2 concentration is matched with that from the assembly experiment and the bias voltage is decreased to 80 V. We also exchange the buffer solution every 45 minutes to minimize MgCl_2 precipitation and excess heat generation.

E. Tubule assembly

All assembly experiments are conducted at a DNA-origami particle concentration of 10 nM. Note that for the binary species assembly, both A-triangle and B-triangle are at 10 nM. By mixing the concentrated DNA origami solution after ultrafiltration with FoB of suitable MgCl_2 concentration, we make 50 μl of 10 nM DNA origami at MgCl_2 concentrations ranging from 5–30 mM. The solution is carefully pipetted into 0.1 ml strip tubes (Rotor-Gene) and capped to prevent evaporation and condensation of water within the tubes. Each tube is then further sealed in a 0.2 ml strip tube and loaded into a rotating incubator (Roto-Therm, Benchmark Scientific) at 40°C.

F. Fluorescence microscopy

We incubate our DNA-origami tubules with YOYO-1 dye (Invitrogen) at room temperature for a minimum of half an hour in a solution of 5 nM monomers, and 500 nM YOYO-1, 1xFoB at the MgCl_2 concentration of assembly. This ratio of YOYO-1 to origami is chosen so that there are 100 dye particles per structure, a limit in which the dye's impact on the structural integrity of the origami should be negligible [2]. 1.6 μL of the solution is pipetted onto a microscope slide that has been cleaned with Alconox, ethanol (90%), acetone, deionized water, and subsequently plasma-cleaned. After deposition, a plasma-cleaned coverslip is placed on the droplet at an angle and carefully lowered so that the liquid film is as thin as possible. We find that this reduces the sample thickness to about the width of a tubule without damaging the tubules, allowing them to lie flat on the surface. Samples are imaged on a TE2000 Nikon inverted microscope with a Blackfly USB3 (FLIR) camera.

G. Negative stain TEM

We first prepare a solution of uranyl formate (Ufo). ddH_2O is boiled to deoxygenate it and then mixed with uranyl formate powder to create a 2% w/w Ufo solution. The solution is covered with aluminum foil to avoid light exposure, then vortexed vigorously for 20 minutes. The solution is filtered using a 0.2 μm filter. The solution is divided into 0.2 ml aliquots, which are stored in a -80°C freezer until further use.

Prior to each negative-stain TEM experiment, a 0.2 ml aliquot is taken out from the freezer to thaw at room temperature. We add 4 μL of 1 M NaOH and vortex the solution vigorously for 15 seconds. The solution is centrifuged at 4°C and 16 krcf for 8 minutes. We extract 170 μl of the supernatant for staining and discard the rest.

The EM samples are prepared using FCF400-Cu grids (Electron Microscopy Sciences). We glow discharge the grid prior to use at 45 mA for 90 seconds at 0.1 mbar, using a Quorum Emitech K100X glow discharger. We place 3 μl of the sample that initially contained 10 nM of monomers on the carbon side of the grid for 1 minute to allow adsorption of the sample to the grid. During this time 5 μl and 18 μl droplets of Ufo solution are placed on a piece of parafilm. After the adsorption period, the remaining sample solution is blotted on 11 μ Whatman filter paper. We then touch the carbon side of the grid to the 5 μl drop and blot it away immediately to wash away any buffer solution from the grid. This step is followed by picking up the 18 μl Ufo drop onto the carbon side of the grid and letting it rest for 30 seconds to deposit the stain. The Ufo solution is then blotted and we vacuum away any excess fluid. Grids are allowed to dry for a minimum of 15 minutes before insertion into the TEM.

We image the grids using an FEI Morgagni TEM operated at 80 kV with a Nanosprint5 CMOS camera (AMT). The microscope is operated at 80 kV and images are acquired between x8,000 to x20,000. The images are high-pass filtered and the contrast is adjusted using Adobe Photoshop.

H. TEM tomography

To obtain a tilt series, we use an FEI F20 equipped with a Gatan Ultrascan 4kx4k CCD camera, operated at 200 kV. The grid is observed at x18000, x29000, or x31000 magnification from -50 degrees to 50 degrees in 2 degree increments. The data is analyzed and the z stack is reconstructed using IMOD [3].

I. Cryo-electron microscopy

Higher concentrations of DNA origami are used for cryo-EM grids than for assembly experiments, as listed in SI Table III. When using triangles that could assemble into tubules, we typically found excess aggregation and binding. We avoid these issues by using passive monomers, which we prepare by adding a 5-nucleotide-long poly-T overhang at the end of the blunt ends for all lock-and-key structures. To prepare samples we fold between 1-2 ml of the folding mixture (50 nM scaffold concentration), gel purify it, and concentrate the sample by ultrafiltration, as described above. EM samples are prepared on glow-discharged C-flat 1.2/1.3 400 mesh grids (Protochip). Plunge-freezing of grids in liquid ethane is performed with an FEI Vitrobot with sample volumes of 3 μ L, blot times of 5-8 s, a blot force of -1, and a drain time of 0 s at 20°C and 95% humidity. All cryo-EM images are acquired with a Tecnai F30 TEM with the field emission gun electron source operated at 300 kV and equipped with an FEI Falcon II direct electron detector at a magnification of x39000. Single particle acquisition is performed with SerialEM. The defocus is set to -2 μ m for all acquisitions with a pixel size of 2.87 Angstrom.

J. Single-particle reconstruction

Image processing is performed using RELION-3 [4]. Contrast-transfer-function (CTF) estimation is performed using CTFFIND4.1 [5]. After picking single particles we performed a reference-free 2D classification from which the best 2D class averages are selected for processing, estimated by visual inspection. The particles in these 2D class averages are used to calculate an initial 3D model. A single round of 3D classification is used to remove heterogeneous monomers and the remaining particles are used for 3D auto-refinement and post-processing. A summary of the cryo-EM reconstructions is shown in SI Table III. All post-processed maps are deposited in the Electron Microscopy Data Bank.

II. DESIGN CRITERIA FOR TRIANGULAR SUBUNITS

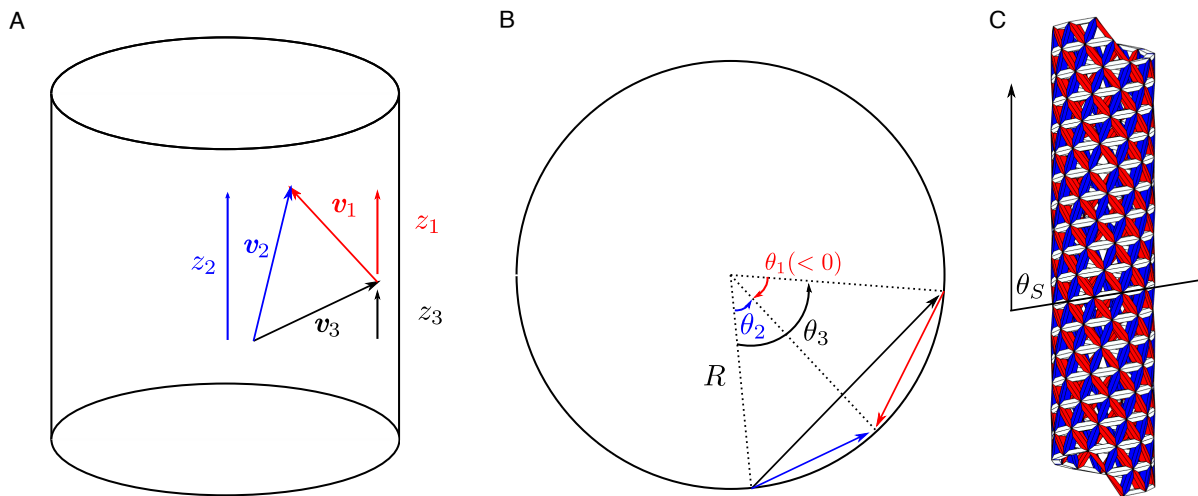


FIG. 1. **Calculations of the tubule lattice coordinates.** The location of the vertices of a triangle on the surface of a cylinder is shown from the side, to see the relative differences in z (A), and along the cylinder axis, to see relative differences in the angular coordinate (B). (C) A tubule, viewed from the side, shows the the maximum seam angle, θ_S .

We derive the coordinates and the dihedral angles of the triangular subunits by assuming that they are rigid triangles whose vertices lie on the surface of a cylinder. This scheme corresponds to the polyhedral model proposed in [6]. Let us choose one triangle on a tubule and label the three sides side 1, 2, and 3, as in Fig. 1A. For convenience, we choose side 3 to be the side that is closest to being perpendicular to the axis of the tubule. We choose the 3 vectors of the tubule \mathbf{v}_1 , \mathbf{v}_2 , and \mathbf{v}_3 as in Fig. 1A, whose length are all 1. The corresponding height and angular change along the vector in cylindrical coordinate is z_1 , z_2 , z_3 , and $\theta_1(\leq 0)$, θ_2 , θ_3 , respectively, and the radius of the tubule is R (Fig. 1B). Since the length of each side is 1,

$$4R^2 \sin^2 \frac{\theta_i}{2} + z_i^2 = 1, (i \in [1, 3]). \quad (1)$$

Additionally, for the three vectors to form a closed triangle,

$$z_1 + z_3 = z_2 \quad (2)$$

$$\theta_1 + \theta_3 = \theta_2. \quad (3)$$

Finally, for a right-handed, (m, n) tubule, we require closed loops after m steps along edge 3 and n steps along edge 1, as illustrated in Fig. 1D of the main text, yielding

$$mz_3 - nz_1 = 0 \quad (4)$$

$$m\theta_3 - n\theta_1 = 2\pi. \quad (5)$$

In the case of left-handed tubules, where n and z_3 are both negative, the loop constraint is given by

$$mz_3 - nz_2 = 0 \quad (6)$$

$$m\theta_3 - n\theta_2 = 2\pi. \quad (7)$$

Solving simultaneous the equations 1,3,5, for variables z_i , θ_i , and R , one obtains the coordinates for all the triangle vertices on the tubule. From the vertex coordinates, we derive bevel angles of triangles θ_{Bi} for side i as listed on Table V and plotted in Fig. 2A. Here, we used the relationship

$$\theta_{Bi} = \frac{180 - \phi_i}{2} \quad (8)$$

to calculate the bevel angle θ_{Bi} from the dihedral angle ϕ_i . In the case of left-handed tubules, equation 7 results in flipped bevel angles between sides 1 and 2. Additionally, we also obtain the seam angles, which we later use to classify the tubules into different lattice-number types (Fig. 2B). Here, we define the seam angle θ_S as the angle of side 3 with respect to the tubule axis (Fig. 1C). Coming back to the premise that side 3 is the side that is closest to being perpendicular to the axis of a tubule, the seam angle takes values between 60–90 degrees. Specifically, it is calculated as

$$\theta_S = \arctan \frac{2R \sin \frac{\theta_3}{2}}{z_3}. \quad (9)$$

III. DESIGNING TRIANGULAR SUBUNITS USING DNA ORIGAMI

We adapt the triangle design scheme initially developed by C. Sigl *et al.* [7] for our monomer design. Our triangle is created from three bricks that are 6-by-4 DNA double helices arranged on a square lattice (Fig. 3A). For generating the geometry, we assume 2.6 nm for the interhelical spacing, 0.34 nm for the dsDNA helical rise, and 0.5 nm for the length of a single unpaired nucleotide. To compensate for the 10.667 bp/turn helical pitch imposed by the square lattice scheme in the caDNAno software [8], we place a ‘skip’ every 32 bp, except in regions near the locks and keys. In essence, the triangles are simply three bricks that are rotated about the brick axes by the preassigned bevel angles (Fig. 3B). The three bricks are then connected at the vertices by single stranded domains of the scaffold and staple strands to make a closed object. In the design steps, we exclude helices 18 and 23 in Fig. 3A from our design to increase the size of the triangle. Also, on the faces of the bricks, we place locks and keys that are self-complementary, each spanning 4 helices in length and 1 helix deep.

Since the bevel angles are not the same on all sides, one needs to take care in how the corners are connected. In Fig. 3C, the white helices from side 3 and blue helices from side 2 do not match up at the vertex, as can be seen from the cross-sectional view. We refer to this mismatching distance between the helices as Δ . Such staggering at

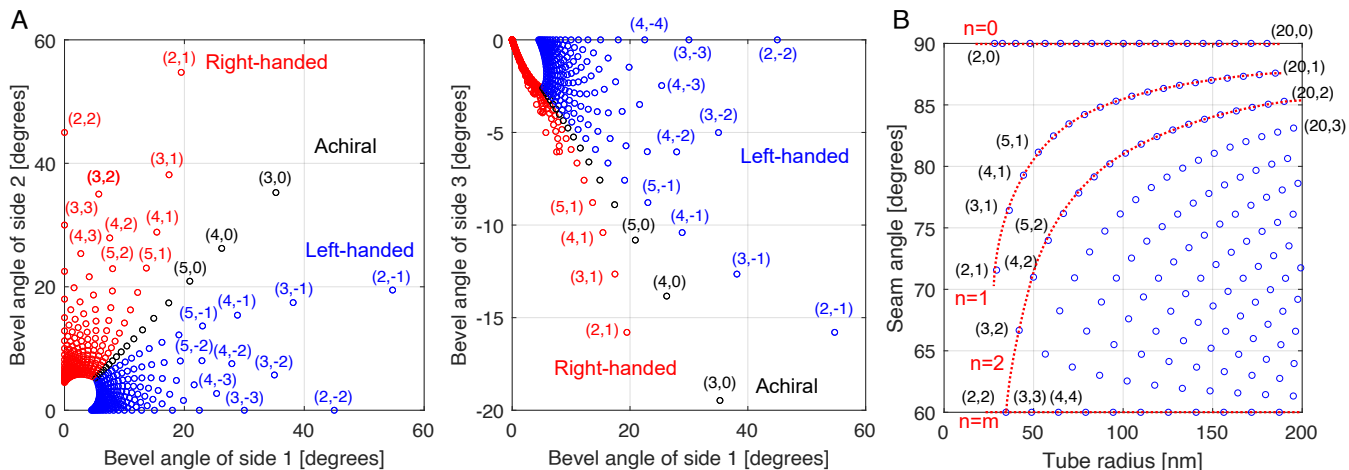


FIG. 2. **The geometry of tubules with different lattice numbers.** (A) A plot of the bevel angles of sides 1, 2, and 3 for different lattice numbers. (B) A plot of the maximum seam angle versus the tubule radius for different tubule types. Red dotted lines are guides for the eyes for different n values and are not fitted lines. To calculate the radius, we assume that the length of a side of a triangle is 56.44 nm.

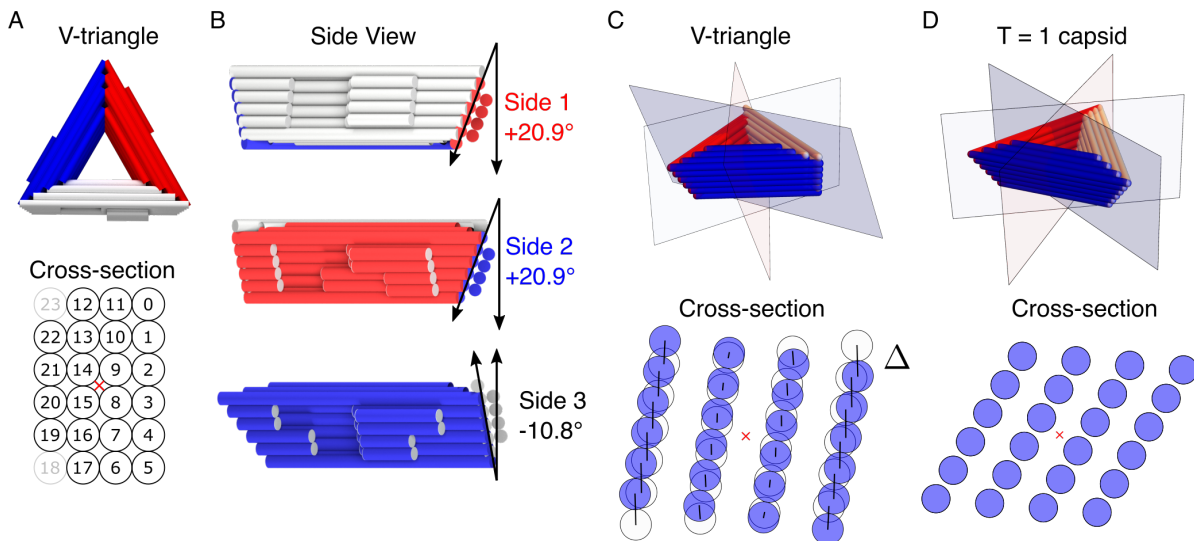


FIG. 3. **Triangle design.** (A) Schematic of the V-triangle and the cross-section of each brick composing a side. The numbers are labeled as in the caDNAno design. The red cross indicates the axis about which we rotate the brick. Helix 18 and helix 23 are excluded in the actual design. (B) Side view of the V-triangle with the bevel angles for each side. (C) (Top) Three planes that cut through the vertices of the V-triangle and (bottom) the cross-section of the vertex between sides 2 and 3. Again, the red cross shows the center of the bricks, which matches between sides 2 and 3. Δ shows the mismatching distance for each helix, illustrated by the straight black lines. (D) shows the same schematic as in (C) but for the T=1 capsid monomer design, where all bevel angles are 21.6 degrees [7].

the corners is a result of the bevel angle mismatch between the neighboring bricks. When there is no bevel angle mismatch, such as the T=1 capsid monomer from ref. [7], the helices meet perfectly at the corners (Fig. 3D).

Our goal is to come up with a design method for minimizing the effect of having mismatched helices at the corners; poorly designed corners may compromise the programmed bevel angles of the sides. First, we make an equilateral triangle with three bricks. Initially, the three bricks are placed so that the central axes of the bricks, marked by the red cross in Fig. 3A, forms an equilateral triangle. We call this the base equilateral triangle. The bricks are then rotated by the prescribed bevel angles around the brick axes. This rotation leaves the center of the brick fixed, but the helices around it are displaced. Then, we optimize the orientation of the plane used to cut through the corners, as shown at the top of Fig. 3C. At the corners, there are infinitely many ways one can come up with to terminate a

helix from one brick and transition it to the other. Here, we search for a flat plane that simultaneously goes through the corner of the base equilateral triangle and minimizes the sum of all mismatching distances Δ . The helices from both sides terminate where they meet this plane. Finally, the remaining mismatch of the helices is compensated by leaving a portion of the scaffold single stranded at the corners. Similarly, at the corners, we insert 5T to the staples to remove any potential base-stacking interactions that may add stress to the corners. Finally, the triangles are scaled so that the required scaffold length is 8064 bases in total, which is the length of the p8064 scaffold (Tilbit nanosystems). The final caDNAno designs for the triangles are shown in Fig. 18 and 19, and the corresponding sequences can be found in Tables VI-IX.

A. Designing the lock-and-key interactions

The interactions between our DNA-origami subunits are based on lock-and-key shape complementarity. In other words, we design the shapes of protrusions and recesses that fit together. In order for one face of our monomer to bind to another in the right orientation, the shapes of the protrusions and recesses need to be anti-mirror symmetric (see Fig. 4A). Here, the term ‘anti’ refers to the inversion between the protrusion and the recess, expressed as ‘+’ and ‘-’. Namely, for the two faces to bind to each other, the protrusions and recesses on one face have to be mirror symmetric in shape and inverted compared to those on the other face. In this paper, we only consider mirror symmetry that is horizontal, though the use of vertical mirror symmetry may be useful for other design applications. Regardless of the orientation of the symmetry, there are two locations where the mirror plane can be placed: in between two distinct faces, which we name Type I, or in the middle of the face, which we call Type II. By nature, Type I symmetries impose non-self-complementary interactions, whereas Type II symmetry imposes self-complementary interactions. Figure 4B shows examples of protrusions and recesses for binding, where open shapes denote recesses and filled shapes denote protrusions.

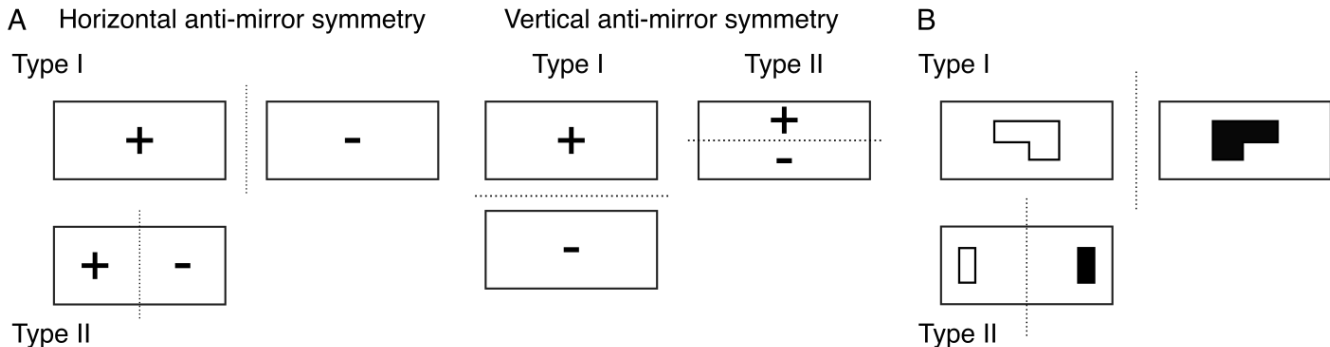


FIG. 4. **Symmetries of protrusions and recesses.** (A) Two symmetry patterns of protrusions and recesses are allowed on the faces of the triangles. For both the horizontal and vertical anti-mirror symmetries, the mirror plane can be located either between the two faces (Type I) or at the center of the face of a triangle (Type II). Dotted lines indicate the mirror plane. + and - signs indicate inversion of the protrusion and the recess. (B) Example protrusion and recess patterns for the triangles. A non-self-complementary interaction (Type I) and a self-complementary interaction (Type II) are shown. Protrusions are shown as outlines, whereas recesses are shown as filled shapes.

IV. DESIGN CRITERIA FOR BINARY TILINGS OF TUBULES

Previously, we found that there are only three possible tiling patterns that could assemble into a tubule using two species of triangles [9]. These patterns are shown in Fig. 5A and B. For each pattern, there is also an associated interaction matrix that describes which sides of the particles need to have favorable interactions to produce the given tiling. The basic premise is that by increasing the number of species of triangles in the system, the number of distinct vertices in the tiling increases, leading to a reduction in the number of accessible tubule states since some combinations of vertices cannot close in a periodic way. Since the pattern in Fig. 5A has only a single vertex type, it does not remove any accessible tubules, while both patterns in Fig. 5B have two distinct vertices, thereby removing half of the possible tubule types. The available tubule types for these patterns are shown in Fig. 5C.

An important consideration when designing the monomers for a multiple-species ensemble is determining how many unique interactions need to be encoded into the system. From the interaction matrices shown in Fig. 5A and B, we

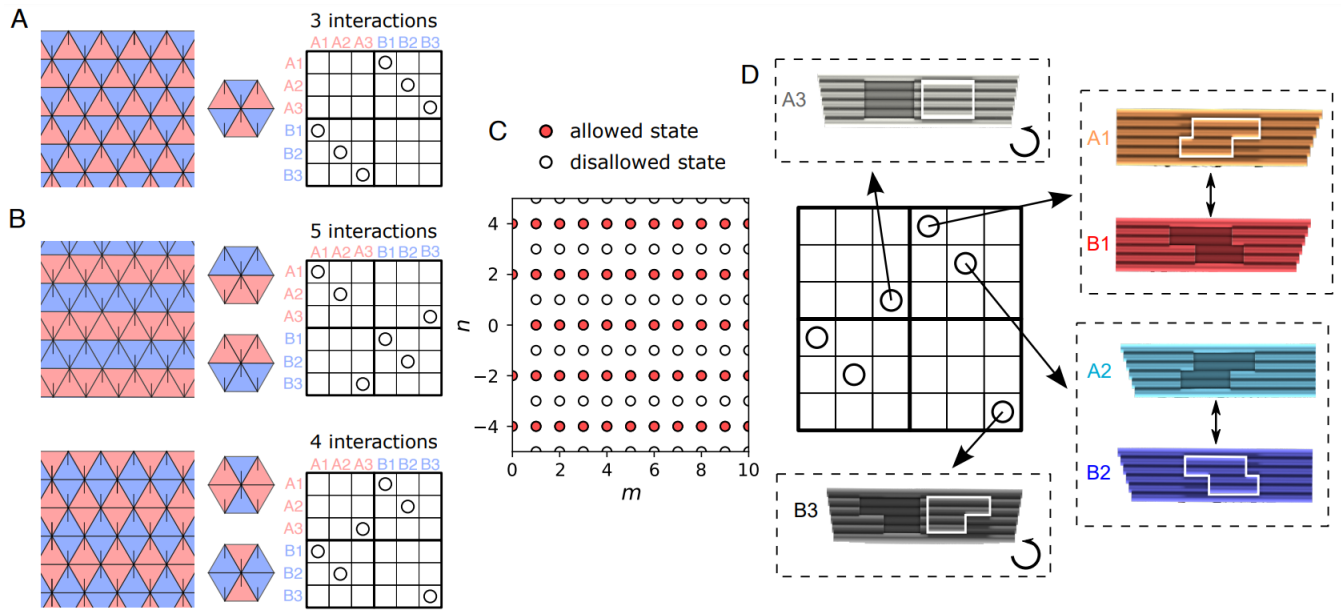


FIG. 5. **Two species design considerations.** (A) and (B) show the three possible tilings using two species that can fold into tubules. Red and blue triangles represent A and B triangles, respectively. A line inside the triangle points to the vertex in between sides 1 and 2. Each pattern has next to it the unique vertices in the pattern and the interaction matrix needed to create the tiling. Circles in the interaction matrix represent favorable interactions. The pattern in (A) contains only a single unique vertex, and thus, does not limit any tubule state. (C) Space of allowed (m, n) tubule types results from the tilings in (B). (D) Design for lock-and-key interactions for a given interaction matrix. Note that when you have self-complementary sides both a protrusion and a recess are needed on the same face.

can see how many interactions are needed by counting the number of points in the upper triangular region of the matrix. We can see that the patterns in Fig. 5B require different numbers of unique interactions even though they provide the same state restrictions. The fewer interactions that one needs to use, the easier it is to design interactions that have minimal cross-talk.

In the main text we use the interactions shown in Fig. 5D. This illustrates another aspect of how the lock-and-key interactions correspond to where the interaction appears in the interaction matrix. If the interaction is on the main diagonal, then the interaction needs to be self-complementary, or type II, illustrated in Fig. 4A. For such interactions, both a protrusion and a recess are necessary since they involve interactions with a single species of particle. Off-diagonal interactions are inherently between two species of particles and only require a protrusion or a recess, as in type I.

V. DNA ORIGAMI FOLDING CONDITIONS

The DNA-origami particles have folding conditions that are quite sensitive to the temperature ramp range and the salt concentration [10]. For each particle, we conduct a folding screen at different Mg^{2+} concentrations and temperature ramp ranges to determine the optimal conditions. The folding conditions are summarized in Table I. In the end, the folded solution contains a relatively high yield of monomers for all of the designs that we created, as can be seen from Fig. 6. Typically, the gel purification yield of the triangles is around 20-30% of the initial scaffold amount.

Object	Temperature ramp ($1^\circ\text{C}/1\text{hr}$)	Folding Mg^{2+} concentration (mM)
V-triangle	60-44 $^\circ\text{C}$	15
X-triangle	58-50 $^\circ\text{C}$	15
A-triangle	58-50 $^\circ\text{C}$	20
B-triangle	58-50 $^\circ\text{C}$	20

TABLE I. Summary of folding and assembly conditions.

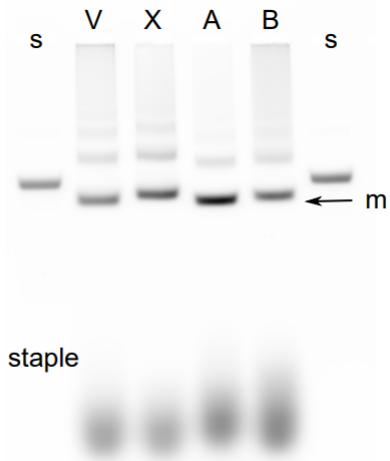


FIG. 6. **Gel electrophoresis of folded solutions.** Gel electrophoresis of folding solutions for each triangle type. The “s” band at both ends of the gel contains only the scaffold solution for reference. The monomer bands for the triangles are all lower than the scaffold band, denoted as “m”.

VI. BINDING ENERGIES AND ASSEMBLY CONDITIONS FOR TRIANGLES

A. Binding energies of V- and X-triangles

Our DNA-origami subunits interact through blunt-end stacking at the ends of the lock-and-key shapes that are located on each side of the triangle. The blunt-end interactions of dsDNA originate from the $\pi - \pi$ stacking between base pairs that are adjacent along the helical direction of DNA and are sequence dependent [11, 12]. In designing our DNA origami, we attempt to maximize the free energy of all intended blunt-end interactions, as predicted from ref. [12], while also keeping the differences between the free energy of each side’s blunt-end interactions below 4 kcal/mol, or $6.75 k_B T$ at 25°C (see Table II). Since the scaffold DNA is a loop, this task is accomplished by permuting the starting point of the loop through the 8064 possible positions until our free-energy criteria are satisfied as best as possible. Note that for sides 1 and 2 of A- and B-triangles, there are either protrusions or recesses, but not both on a single side. Having only a protrusion or a recess reduces the blunt-end stacking sites by half compared to the other cases, thus, the interaction is considerably weaker compared to that of side 3. For these triangles, we permute the starting point of the scaffold loop for the two triangles to maximize the total binding energy of all interactions, while keeping the maximum difference between the sides to below 10 kcal/mol, or $16.9 k_B T$.

Object	Predicted from [12] ($k_B T$)			Measured ($k_B T$)		
	Side 1	Side 2	Side 3	Side 1	Side 2	Side 3
V-triangle	-53.95	-54.18	-59.25	-20.55	-22.24	-24.27
X-triangle	-56.28	-51.48	-57.09	-18.44	-18.64	-18.93
A-triangle	-33.37	-33.00	-47.97	Not measurable	Not measurable	-19.59
B-triangle	-33.37	-33.00	-47.13	Not measurable	Not measurable	-19.13

TABLE II. **Summary of predicted and measured free energies of binding at 20 mM MgCl_2 .**

We experimentally measure the binding free energy of each side using gel electrophoresis. First, triangles are folded and purified, with only one target side activated and the other two sides are passivated. We passivate the sides by adding 5T to the ends of the staple strands at the locations of the blunt-end interactions of the locks and keys, effectively prohibiting them from binding (Fig. 7A). Samples at 10 nM monomers are incubated at 40°C in different MgCl_2 concentration buffers, then run in a 1.5% agarose gel with the same MgCl_2 concentration. As can be seen from the gel scan in Fig. 7B, we observe distinct monomer and dimer bands. We individually fit the monomer and dimer band with Gaussian distributions to find their relative concentrations.

To calculate the binding free energy we consider the rate equation for dimerization



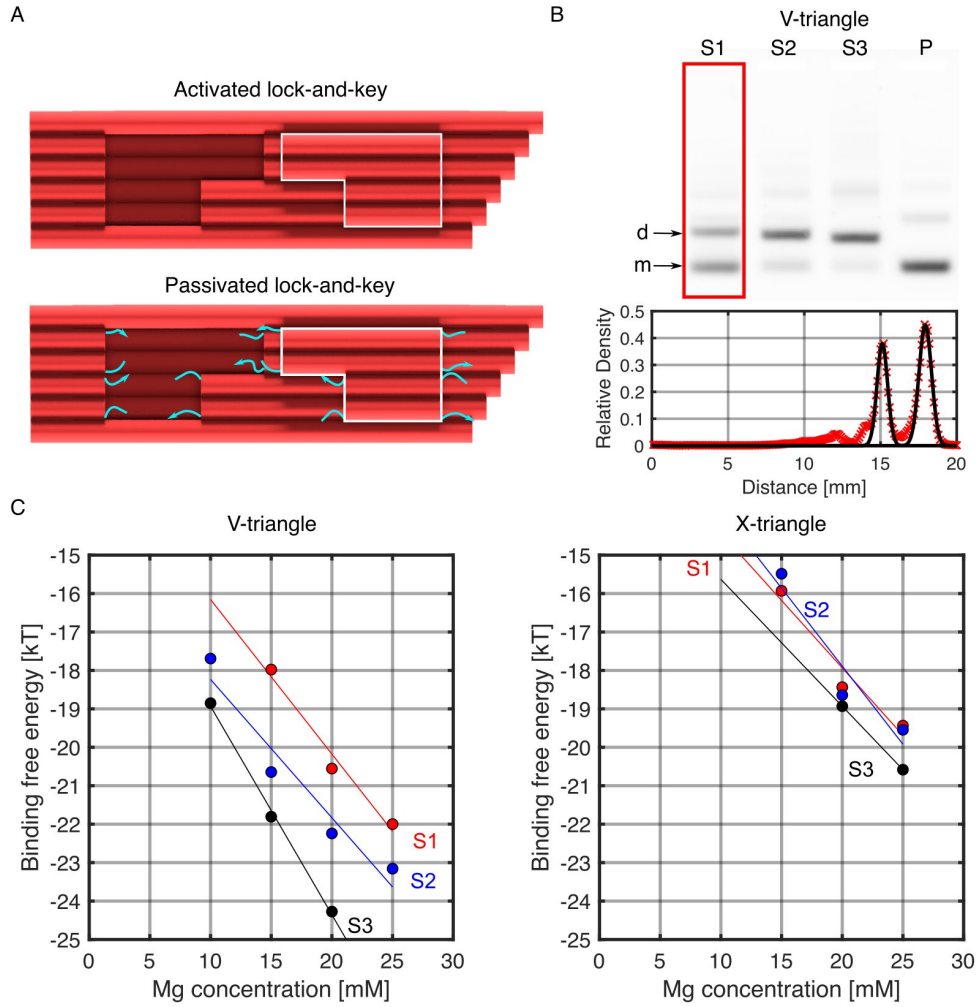


FIG. 7. **Bindings strength for V-triangle and X-triangle.** (A) An illustration of our method for passivating triangle interactions. Passivated triangles have staples with an extra 5T domain hanging from the blunt ends, illustrated in cyan. The arrows indicate the direction from the 5' to 3' ends of the DNA. The length of the poly-T sequence is not drawn to scale. (B) Gel electrophoresis of dimer samples at 15 mM MgCl_2 in a 1.5% agarose gel. The number after S indicates the side that is activated, while P indicates a fully passivated sample. A profile of the gel in the red rectangle is shown below. The monomer band, located at around 15 mm, and the dimer band, located at around 18 mm, are both fitted with a Gaussian, shown in black. (C) shows the measured binding free energies for V-triangle (left) and X-triangle (right). Red, blue, and black dots indicate the free energies for sides 1, 2, and 3, respectively. Lines are linear fits to the data.

where M is a monomer and D is a dimer. The chemical equilibrium constant, K , for this reaction equation is related to the free energy difference, ΔG , between the initial and the end state,

$$K = \frac{[D]u_0}{[M]^2} = \exp\left(-\frac{\Delta G}{k_B T}\right), \quad (11)$$

where u_0 is a reference concentration, set to 1 M in this case. Then the free energy is simply

$$\Delta G = -k_B T \log\left(\frac{[D]u_0}{[M]^2}\right). \quad (12)$$

Additionally, since the initial monomer concentration is 10 nM, we have

$$[M] + 2[D] = 10 \text{ nM} \quad (13)$$

as a constraint. Therefore, using the measured concentration ratio between the monomer and the dimer band with Eqn. 12 and 13, we obtain the free energy of binding for each side, as in Fig. 7C.

The binding free energies are relatively similar between the three sides of the triangles, as initially designed. However, the magnitude of the binding energies are less than half the value predicted from reference [12] (see Table II). This can be attributed to a few different factors. First and foremost, the assumption that the total free energy is the sum of the individual blunt-end stacking interactions may oversimplify the problem. Though the same assumption is used in the reference, the goal is entirely different. Kilcherr *et al.* [12] used a rigid origami rod that interacts with another origami rod in the direction of the DNA double helices, while our blunt ends are placed perpendicular to the direction of the binding between triangles. Geometry adds further complications. At the molecular scale, our designed lock-and-key configuration may be floppy, which could lower the binding strength if not all blunt ends in the lock-and-key interactions are in contact. Finally, gel electrophoresis is a non-equilibrium assay, and thus, the result might not accurately reflect the assembly conditions. During gel electrophoresis, the buffer is lowered to 4° C, an electric field is applied, and monomers become separated from the dimers, taking local concentrations far from their equilibrium values. For accurate measurement, we propose *in situ* measurements such as light-scattering.

B. Assembly condition for V- and X- triangles

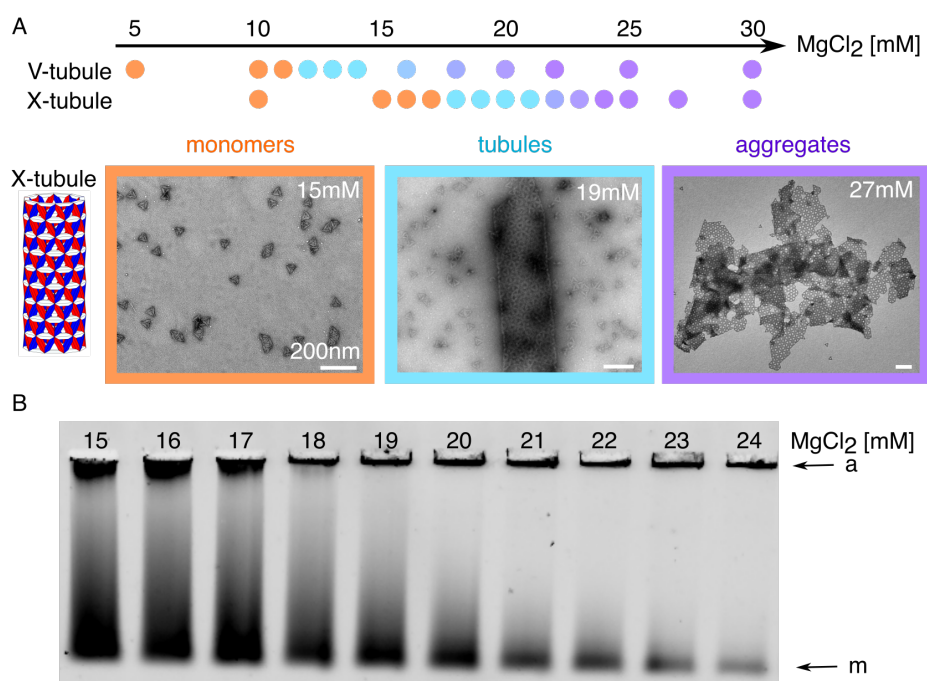


FIG. 8. **Assembly conditions for the V-tubule and X-tubule.** (A) A scan of the Mg²⁺ concentration for assembly of the V-tubule and X-tubule. Representative TEM images for the X-tubules are shown at the bottom (for V-tubule images, see Fig. 2 in the main text). The gradient in color from tubule assembly to aggregation is meant to convey a qualitative change in the aggregate fraction. (B) Gel electrophoresis of assembled X-triangles in 0.5% agarose and 20 mM MgCl₂ buffer. Different lanes show different Mg²⁺ concentrations of assembly. “m” denotes the location of the monomer band and “a” is the location of the assembly or aggregate band. The contrast of the image has been enhanced to highlight the bands.

After gel purification of folded monomers, we adjust the monomer concentration and Mg²⁺ concentration, then incubate the solution in a rotating incubator at 40°C for one week. At low salt concentrations, monomers remain unbound or form small clusters. Depending on the triangle types, we observe the spontaneous assembly of tubules between 10 and 20 mM MgCl₂ (Fig. 8A). The Mg²⁺ concentration for the transition is usually consistent within 1 mM MgCl₂ over repeated trials. As the Mg²⁺ concentration is increased even higher, fewer and fewer monomers are present (Fig. 8B), since the free energy of binding is lowered. However, this also enhances the chance for cluster-to-cluster binding to occur, resulting in aggregated structures, as can be seen in Fig. 8A. As a result, at high Mg²⁺ concentrations, we observe mostly aggregated structures in TEM, rather than tubules or free monomers. In essence, there is a Goldilocks principle for assembly. The Mg²⁺ concentration should not be too high nor too low to obtain tubules. It should be noted that the transition from tubule assembly to aggregate formation is gradual, as represented

qualitatively by the color gradient of circles at the top of Fig. 8A.

The Mg^{2+} concentration at which assembly begins can be compared against the binding energy. Tubule assembly starts around 12 mM MgCl_2 for the V-triangle and 18 mM for the X-triangle. By interpolating the free energy of binding using a linear fit, as in Fig. 7C, we obtain $-18.6 k_B T$ and $-17.5 k_B T$ as the average binding energy of assembly of the three sides for V- and X-tubule, respectively. Not surprisingly, the free energy for tubule assembly of the two systems is similar.

C. Binding free energies and assembly conditions for binary species triangles

Unlike the unary species triangles, we expect asymmetry in the binding strengths for the binary species triangles. To be specific, side 1 and side 2 of both the A- and B-triangles have only half the base-stacking sites as side 3. Using the same gel electrophoresis assay, we could not detect any dimer formation for side 1 or side 2 between triangles A and B, even at 20 mM MgCl_2 (Table II).

To overcome the discrepancy in the binding energy between different sides, we enhance the binding strength of sides 1 and 2 by adding hybridization interactions (Fig. 9A). We intentionally elongate or shorten the staple sequences that are at the end of the protrusions and recesses, so that base pairs can form in addition to the base stacking interactions. Here, we shortened either 2, 4, or 8 strands at the end of the recess of side 1 of the B-triangle, each by 3 nucleotides. At the same time, the corresponding staples on the protrusion of side 1 of the A-triangle were elongated by 3 nucleotides. The sequences of the elongated nucleotides were designed so that they were complementary to the exposed scaffold sequence on B-triangles. We also implemented similar designs for side 2 of the A- and B-triangle to enhance the interaction strength.

We measured the binding strength for the binary species particles, including different variants of sides 1 and 2, using gel electrophoresis (Fig. 9B). We find that the dimer bands for sides 1 and 2 are not detectable when we use less than 2 hybridization domains. The binding strength of sides 1 and 2 are almost equivalent to side 3 when 4 hybridization domains are used, and much stronger when all 8 domains are used. Note that for the analysis of binding between two different triangles, we use different equations from those discussed in the previous section. Here, the reaction equation is



where AB is a dimer complex of the A-triangle and the B-triangle. In the solution, we have total of 10 nM of both the A-triangle and the B-triangle, thus

$$\begin{aligned} [A] + [AB] &= 10 \text{ nM}, \\ [B] + [AB] &= 10 \text{ nM}. \end{aligned} \quad (15)$$

The free energy is then obtained from the equilibrium concentration of the A and B triangles as

$$\Delta G = -k_B T \log \left(\frac{[AB]u_0}{[A][B]} \right). \quad (16)$$

As a result of the different interaction strengths between the variants, they assemble at different Mg^{2+} concentrations. For a system with 4 hybridization domains for both sides 1 and 2, assembly occurs at around 14 mM MgCl_2 . The average binding strength of the three sides was $-18.06 k_B T$, which is very similar to the threshold free energy that we found for the V- and X-tubules. As the number of hybridizing domains was reduced, the Mg^{2+} concentration necessary to assemble tubules increased. For 2 domains, assembly occurred at 20 mM MgCl_2 , while for 0 domains, it was 30 mM MgCl_2 .

VII. CHARACTERIZATION OF TUBULE ASSEMBLIES

A. Measuring tubule lengths from fluorescence microscopy

In addition to TEM imaging, we also use fluorescence microscopy to assess the lengths of tubules that form (Fig. 10A). To characterize the tubules we perform some simple image analysis. Epi-fluorescence images of tubules are denoised by convolution with a Gaussian whose width is 2 pixels, after which we binarize the image with a single threshold. We use FIJI to extract particles and fit them with ellipses. Looking at the values of the major and minor axes lengths of these fits (Fig. 10B) we see a saturation of the minor axis length at about $0.6 \mu\text{m}$, which is roughly

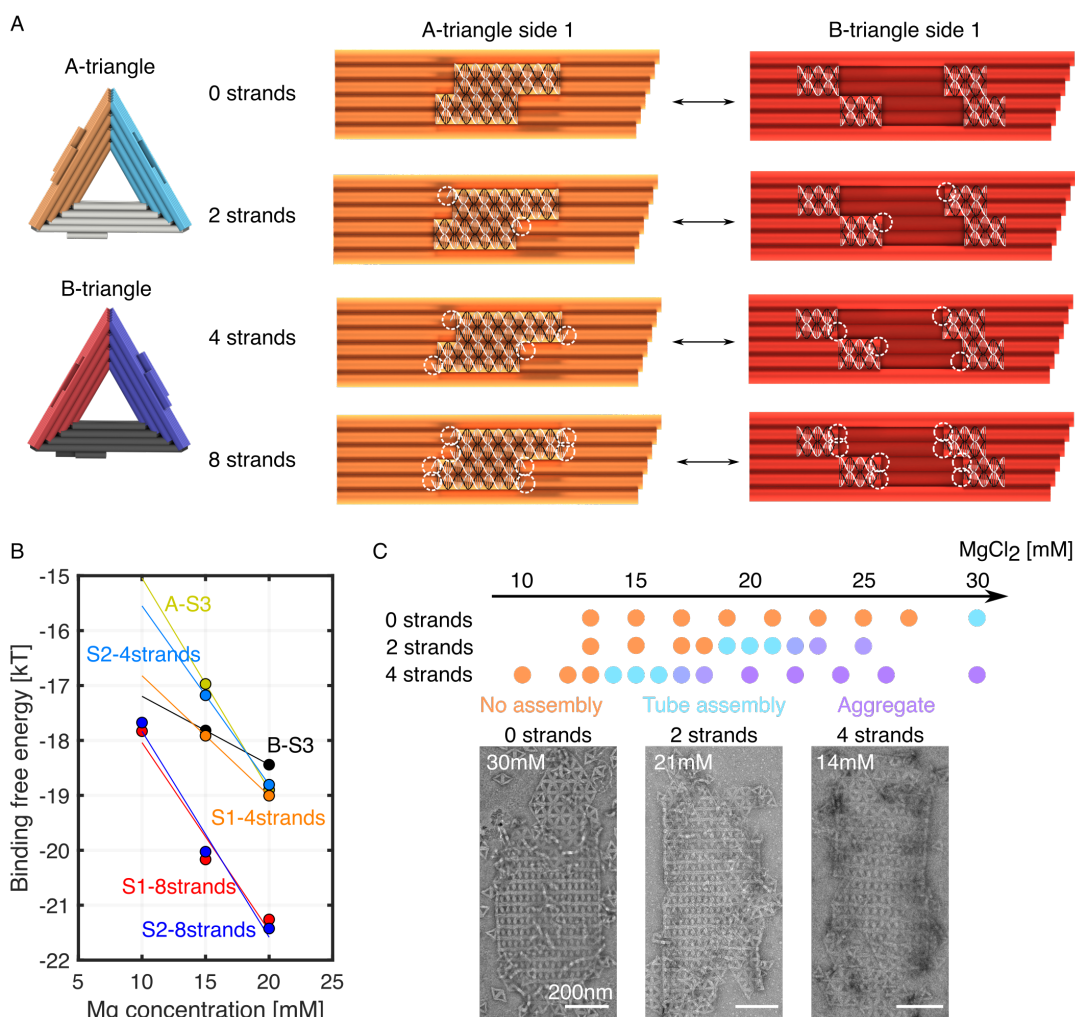


FIG. 9. Binary species interaction strengths and assembly conditions. (A) Schematics of the binary species triangles and the modification of lock-and-key shapes to incorporate hybridization domains for binding side 1 of the A-triangle to side 1 of the B-triangle. All of the DNA is explicitly illustrated for the protrusion on the A-triangle, whereas only DNA close to the hole is illustrated on B-triangle. The phosphate backbone and nucleotides colored in black indicate scaffold DNA, which is unchanged for all cases. Strands colored in white are staples, which are elongated by 3 nucleotides for the A-triangle and shortened by 3 nucleotides for the B-triangle. Locations where staples are elongated or shortened are circled in white. (B) A plot of the binding free energy between different sides for both triangle species. The number following “S” indicates the interacting side. When sides 1 and 2 have less than 2 strands with added hybridization domains, the binding energy is too weak to measure and is not reported. (C) Assembly conditions for the binary tubules with different numbers of hybridization domains for sides 1 and 2. Example TEM micrographs of tubules for 0, 2, and 4 hybridization domains are shown.

the width of a tubule. Using the value of the major axis length as the length of an assembly, we construct a histogram for the distribution of the lengths, including only particles with a minor axis length less than 1 micrometer to exclude aggregates. Figure 10C shows such a histogram. We perform this imaging and analysis for X-tubules (Fig. 10A-C) and V-tubules (Fig. 10D-F).

B. Determining tubule handedness from EM tomography

Through tomography reconstruction, we obtain a z-stack of the tubules, which yields their handedness. Ideally, if one has complete information about the electron microscope, the orientation of the grid, the direction of the tilting, and the reconstruction algorithms, the handedness of a tubule can be inferred correctly. However, this task is unfeasible in reality. To overcome this challenge, we measure the chirality of an object with known handedness and compare it

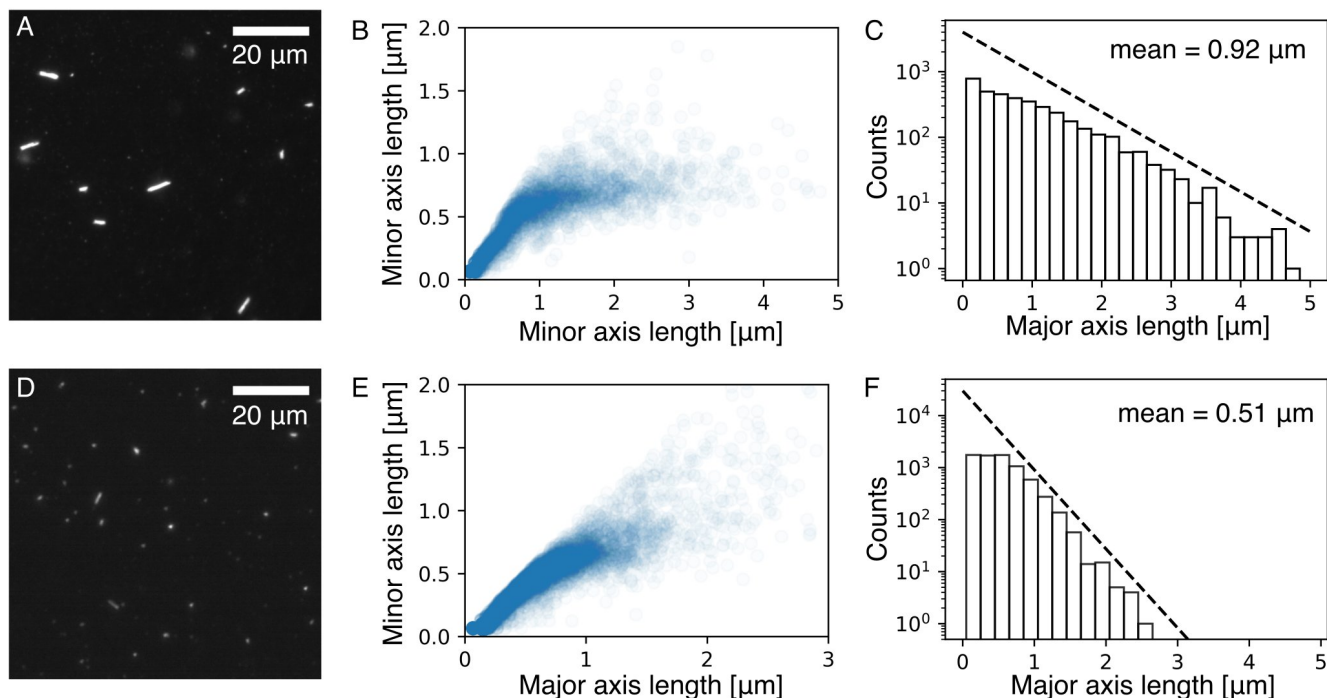


FIG. 10. **X-tubule and V-tubule length distributions.** (A) Epi-fluorescence image of X-tubules dyed with YOYO-1 and imaged with a 100x objective. (B) Plot of the major and minor axes lengths of particles found in epi-fluorescence. (C) Histogram of major axis lengths found for 3710 particles. Particles with a minor axis length greater than 1 μm are excluded. (D) Epi-fluorescence image of V-tubules, along with their (E) measured lengths and (F) a histogram for 7362 particles. Dashed lines are guides for the eye to highlight the exponential decay.

with tubules using the same measurement and analysis methods [13].

Here, we use a right-handed gold nanohelix to determine the handedness of the tubules [13, 14]. The gold nanohelix (Gattaquant DNA Nanotechnologies) is a 24 helix bundle DNA-origami rod with 9 gold nanoparticles arranged helically (Fig. 11(A)). Though the TEM image we obtain only contains 7 gold nanoparticles, it is still sufficient to determine the handedness. Through tomography reconstruction, we obtain z-stacks of a right-handed gold nanohelix and the tubules. In Fig. 11(B), the z-stack of the gold nanohelix is ordered so that it appears right-handed, as prescribed. The V-, X-, and binary species tubules in Fig. 11(B) are ordered in the same way as the gold nanohelix, to preserve the correct handedness. In all of the tubules shown, the seam of side 3 is right-handed. In total, we observe 26 V-tubules of which 8 are achiral and 14 are right-handed, 15 X-tubules which are all right-handed, and 9 binary species tubules of which 2 are achiral and 7 are right-handed.

C. Determining tubule types from negative-stain TEM

For all of the tubules we discussed, we find that there are distributions of assembled tubule types. The fundamental idea behind classification is illustrated in Fig. 2B. Different tubule types can be distinguished from the radius and the seam angle of the tubule. However, we use slightly different classification methods for V-, X-, and binary tubules. This choice is because they have very different widths and seam angles compared to each other. For example, V-tubules have small lattice numbers, which makes it easy to distinguish the tubule types. It is rather difficult to measure the width and seam angles to characterize these tubules since they vary greatly along the tubule axis. On the other hand, X-tubules are larger, and they lay close to flat on the TEM grid surface. This makes them suitable for measurement simply using the width and the seam angles as in Fig. 2B.

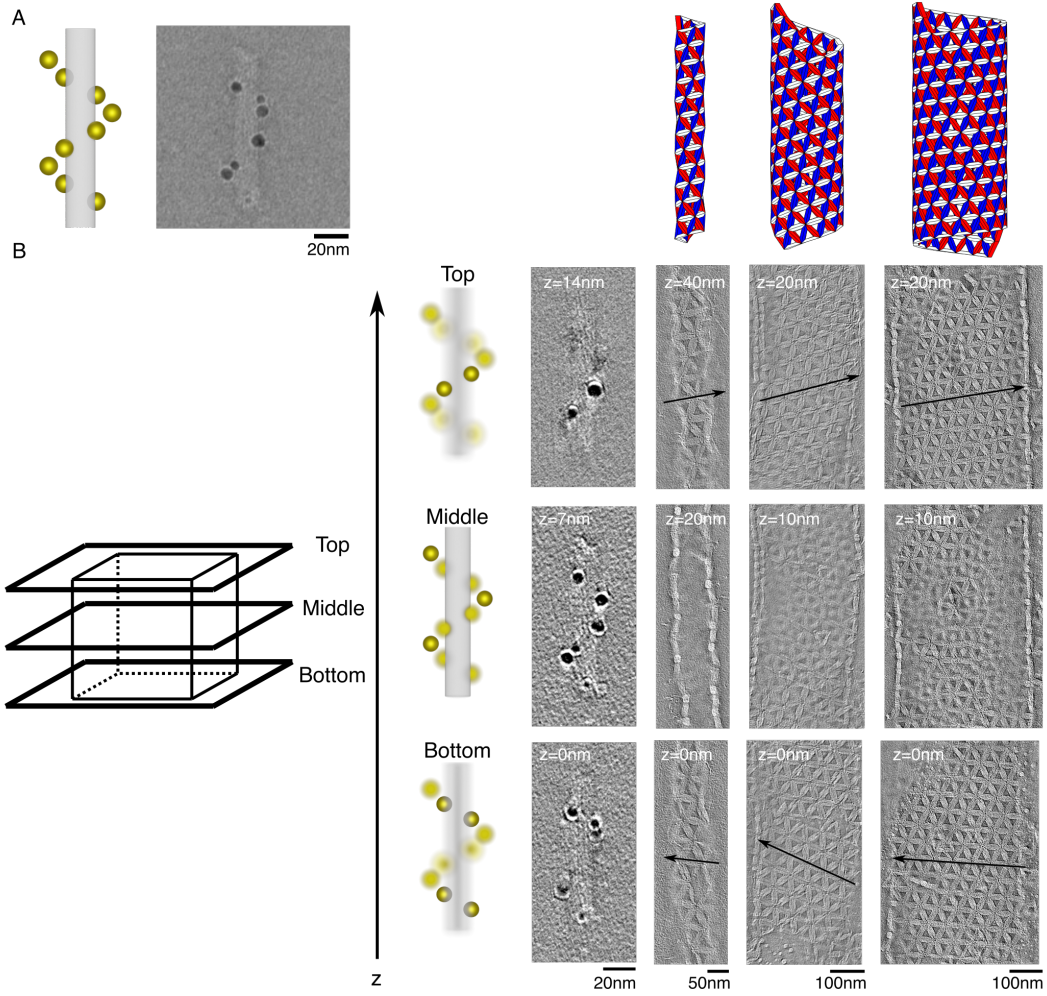


FIG. 11. **Determining the handedness of the tubules from tomography.** (A) Illustration of a right-handed gold nanohelix and its TEM image. (B) Tomography reconstruction of a right-handed gold nanohelix, a V-tubule, an X-tubule, and a binary species tubule. Z-slices from the top, middle, and bottom of each structure are shown. The order of sequences are all adjusted in the same way, so that the right-handed gold nanohelix appears right-handed. The black arrows indicate the direction of the seam along side 3. Above the TEM images of tubules, illustrations of the assembled tubules are also shown, which corresponds to (4,1), (9,4), and (14,2) tubules, for V-, X-, and binary tubules, respectively. The height of each image with respect to the position of the bottom image is labeled.

1. TEM image simulation

We first generate semi-transparent representation of tubules to generate Moiré patterns for comparison against TEM micrographs. Using the method described in Supplementary Section 2, coordinates of triangles can be calculated, given the lattice numbers m and n of a tubule. Triangles are modeled using transparent patches whose dimensions are in proportion to the original design. We assume the length of a side of a triangle is 56 nm, whereas the height and width are 6 by 4 helices or 15 nm by 10 nm. The transparent triangles allow us to see both the top and the bottom of the triangles overlapping with each other, just as in TEM. The simulation results for representative tubules are shown in Fig. 12. In Fig. 2C, we observe that the cross-section of V-tubules are ellipse on TEM grid, whereas X-tubules are flattened. We reflect this feature in our simulation. In Fig. 12, the (4,0) tubule is round, but the (9,4) and (13,2) tubules are flattened before image generation. For the (9,4) and (13,2) tubules, we observe that the edges of the tubules are staggered, unlike those from experimental images. Although this simulation may not be accurate near the edges, we argue that the characteristics of the Moiré patterns, which are generated by overlapping two triangular lattices that are mirror-symmetric to each other, are well-represented in the simulations. We also find that the Moiré patterns do not change depending on the orientation that the tubule lands on the grid when the tubules are chiral. Unfortunately, the handedness of the tubules cannot be determined solely from the Moiré pattern. Since the top and

bottom layers of the tubules are mirror symmetric, the same pattern appears for tubules with opposite handedness.

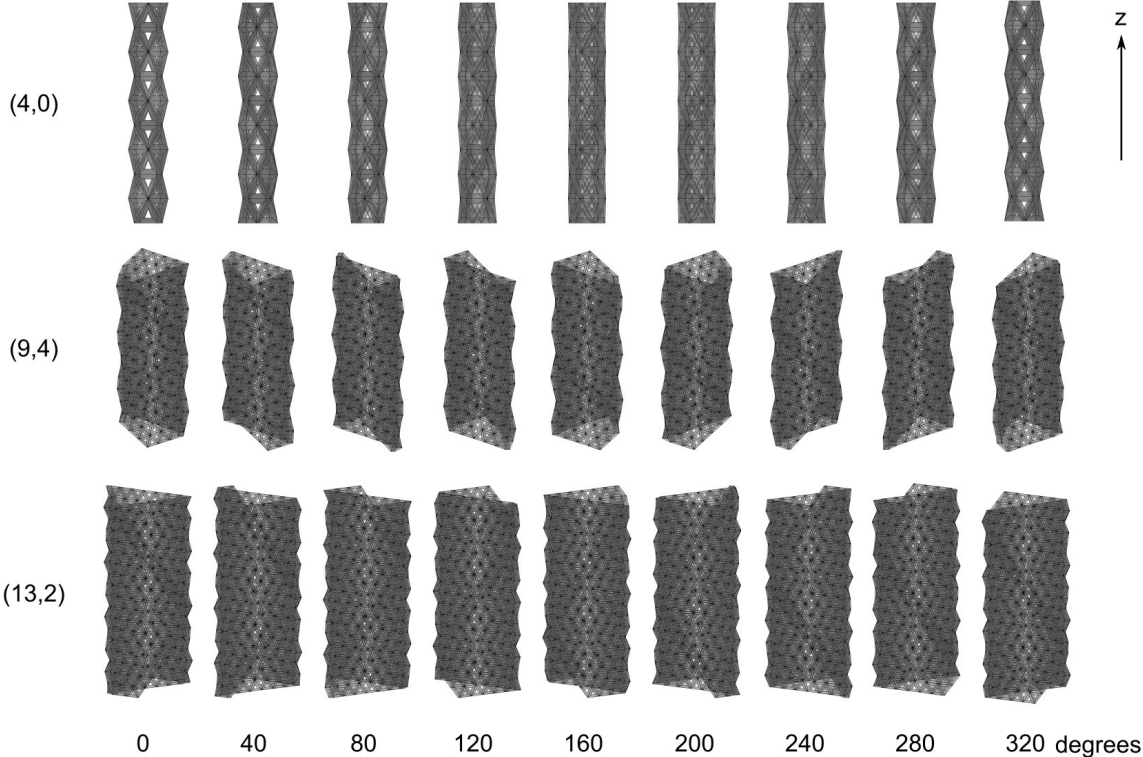


FIG. 12. **Simulations of TEM micrographs for representative tubule types.** From top to bottom, (4,0), (9,4), and (13,2) tubules are illustrated. The angles denote the rotation of the tubule about the z-axis. The method we used to generate these images is described in the SI text.

2. Classification of V-tubules

The width of V-tubules in the experiment are relatively small, with circumference ranging from 3 to 5 triangles. Since the dihedral angles between two triangles are small, tubules appear bumpy and inconsistent. This makes the determination of the tubule type by measurement of the width and the seam angle less reliable. Thus, we characterize the V-tubules by pattern matching by eye. The distinction between achiral and chiral tubules are not difficult; the angle along side 3, or seam angle, is perpendicular against tubule axis for achiral case, whereas for (4,1) tubule, it is further tilted by about 10 degrees. Within achiral tubules, (3,0), (4,0), and (5,0) can be distinguished by the width. (4,0) tubules typically exhibit the trademark hexagonal pattern, while (3,0) is narrower and (5,0) would be wider. Similarly, for achiral case, when the tubule width is around one hexagonal pattern wide, the tubule has an m number of 4. Different n numbers can further be categorized by the seam angle, which varies by around 10 degrees for a difference of 1.

3. Classification of X-tubules and binary tubules

On the contrary, X-tubules and binary species tubules can be classified by measuring the width and the seam angle. Because the tubule is flattened on the grid, as confirmed from the tomography reconstruction (Fig. 2C), the circumference of the tubule can be inferred approximately as twice the width of the tubule on grid. Combined with the measurement of seam angle, we obtain the lattice number of the tubule, which we define as the tubule state with the closest circumference and seam angle to the measured values. To find the closest tubule state, we define 'distance'

as

$$d = \sqrt{\frac{(\theta_{(m,n)} - \theta)^2}{\theta^2} + \frac{(c_{(m,n)} - c)^2}{c^2}}, \quad (17)$$

where $\theta_{(m,n)}$ and $c_{(m,n)}$ is the seam angle and circumference of an ideal tubule state (m,n) , respectively, and θ and c is the measured seam angle and circumference, respectively. The observed tubule is classified into a lattice number (m,n) whose distance is the shortest.

Additionally, in the case of binary tubules, Moiré pattern of the tubules provide more accurate and convenient estimation of n numbers. Surprisingly, $n=0$ and 2 tubes within this range has unique Moiré patterns which allows for a straightforward classification. $n=0$ tubules have parallel seam on the two sides of the tubules, whereas $n=2$ tubules shows distinct hexagonal pattern as shown in Fig. 12. On the other hand, $n=1$ or n higher than 3 states do not exhibit Moiré pattern that stands out. In the case we are able to identify the Moiré pattern, we decouple the lattice number classification by obtaining n from Moiré pattern and m from the circumference. It should be noted that not all tubules benefit from this Moiré pattern classification due to staining inconsistencies; when the layer of staining is thin, we sometimes only observe one layer of the triangle, and thus no Moiré pattern. Nevertheless, we emphasize that we only observe tubules with even n numbers.

VIII. DETERMINATION OF BEVEL ANGLES FROM CRYO-EM MAPS

A key aspect of the construction of tubules is the ability to have different bevel angles for each side of the triangular monomers. To supplement the TEM measurements of the tubule types that form, we also perform quantitative measurements on the cryo-EM reconstructions we have taken for each monomer type to see how close they are to our designed structures. To measure the bevel angles we fit pseudo-atomic models (PAM) to our reconstructions using the methods in ref. [15] implemented in <https://github.com/elija-feigl/dnaFit>. In brief, this method (i) takes the design file from caDNAno and simulates an atomic model of the structure using mrdna [16], it then (ii) uses the electron density of the cryo-EM reconstruction as a potential to relax the atomic model into a position that fits the cryo-EM map. This allows one to choose helices and base pairs from the design and find their coordinates in the cryo-EM map.

The process of fitting the bevel angles is shown in Fig. 13. Given a cryo-EM map (Fig. 13A), we can generate a PAM from which we extract coordinates. To get the angle of all three sides we will need to find four distinct planes: a plane to define the orientation of the monomer and a plane for the orientation of each side. Figure 13B shows our choice of helices to define the monomer and side orientations: the inner four helices (yellow) are used for the monomer and the six helices of the second layer (red) are used for each side. The extracted coordinates from the PAM are shown in Fig. 13C.

After extracting the coordinates we can fit a plane to each selection. Each plane can be used to generate a normal vector, \mathbf{n} . Taking the normal for the monomer and a side we can get the bevel angle from the following equation

$$\cos(\pi/2 - \theta_{\text{side}}) = \mathbf{n}_{\text{side}} \cdot \mathbf{n}_{\text{monomer}} \quad (18)$$

where θ_{side} is the deviation of the side normal being perpendicular to the normal of the monomer. To estimate the uncertainty of these measurements we use a bootstrap method. We perform measurements of the bevel angles from 100 random subsets of half of the positions in each selection from the PAM. Histograms of these values are shown in Fig. 13D. In general, our uncertainty is of the order 0.1 degrees. Measured bevel angles for all monomers are shown in Table IV. We note that the uncertainty written here does not reflect any thermal fluctuations that may occur.

IX. ESTIMATE OF BENDING RIGIDITY

Using the widths distribution of Fig. 3B we make an estimate of the intersubunit bending energy. The Helfrich energy goes as $E = \frac{1}{2}BA(\Delta\kappa_{\perp})^2$ where A is the area of the assembly, B is the bending rigidity, and $\Delta\kappa_{\perp}$ is the fluctuation of the curvature in the circumference direction. Based on prior research [9] we assume that the tubule type is frozen in at the point that the growing triangular sheet first closes on itself, forming a tubule. If the binding energies are similar, we can assume that the assembly will grow isotropically to form a patch-like disk. At the point of closure, we assume this disk just closes and will have an area of $A = \pi^3 R^2$, where R is the radius of curvature of the tubule. We estimate the fluctuation of the curvature as

$$(\Delta\kappa_{\perp})^2 = \left(\frac{1}{R} - \frac{1}{R + \Delta R}\right)^2 \approx \frac{1}{R^2} \left(\frac{\Delta R}{R}\right)^2. \quad (19)$$

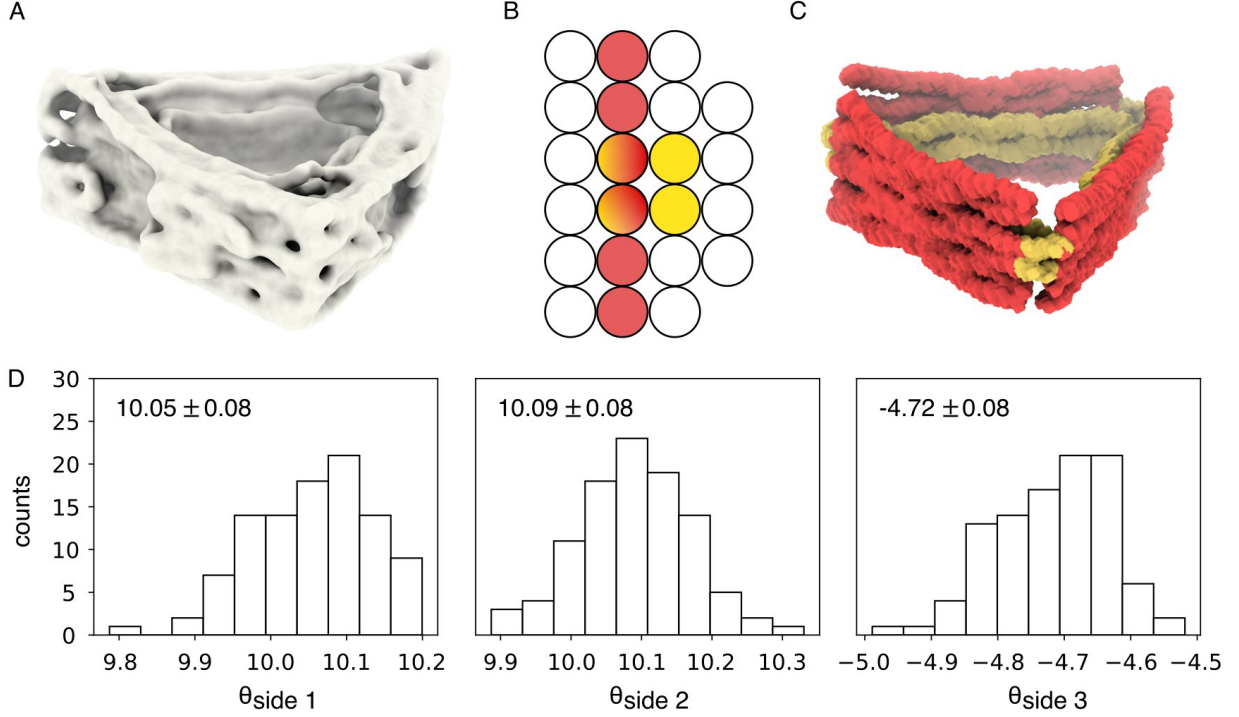


FIG. 13. **Fitting cryo-EM maps to determine the bevel angles.** (A) Cryo-EM reconstruction of the B-triangle. (B) Schematic of the cross-section of the triangle design. The four inner helices (colored yellow) are used to define the inner core, while the second layer of helices (colored red) is used to define the plane of each side. (C) Extracted portions of the cryo-EM map that are used to fit the planes. Red sections are the second layer of the sides and the yellow section is the inner core, to define the orientation of the monomer. (D) Histograms of the fit angles for each side from the bootstrap method for 100 iterations. Average and standard deviations are shown for each histogram.

In our experiment we measure the circumference, C , and its fluctuations; we note that $(\Delta C/C) = (\Delta R/R)$. Combining these two we get that the Helfrich energy is

$$E_H = \frac{1}{2} \pi^3 B \left(\frac{\Delta C}{C} \right)^2 \quad (20)$$

We then assume that the widths are distributed with a Boltzmann probability $P = \exp(-E_H/k_B T)/Z$, where Z is the partition function. By measuring the variance of the circumference distribution and assuming Gaussian fluctuations we can get an estimate for B as

$$B = \frac{1}{\pi^3} \frac{\langle C \rangle^2}{\langle C^2 \rangle}. \quad (21)$$

Using this method we find the following bending rigidities: $1.4 k_B T$ for the V-tubule, $2.0 k_B T$ for the X-tubule, and $3.8 k_B T$ for the binary tubule.

To get a sense of the (m, n) distribution that would be expected from Gaussian fluctuations, as well as get a second estimate of the bending rigidity, we consider a simple elastic model for the energy of our assembly. Each side of our triangle has a preferred binding angle with its neighbors and deviations from this angle will result in some bending energy. For an assembly consisting of N subunits, the elastic energy is

$$E = \frac{1}{4} N B \sum_{i \in 1,2,3} (\theta_i - \theta_{0,i})^2 \quad (22)$$

where B is the bending rigidity, $\theta_{0,i}$ is the preferred binding angle, and θ_i is the assembly binding angle. Using the same estimate of the assembly area at closure we can estimate N for any given tubule type. Dividing the disk area by the size of a triangle gives $N = (4\pi/\sqrt{3})(C/l_0)^2$, where l_0 is the edge length of a subunit and C is the circumference

of the tubule. We also assume that the tubule distribution follows a Boltzmann distribution of the elastic energy, $P(m, n) = \exp(-E(m, n)/k_B T)/Z$, where both the angles and N depend on the tubule type and Z is the partition function.

Using this elastic model we can fit our experimental distributions to a target (m, n) and bending rigidity B . The fits give targets of $(4,0)$ and $B = 1.1 k_B T$ for V-tubules, $(9,4)$ and $B = 3.0 k_B T$ for X-tubules, and $(13,2)$ and $B = 3.1 k_B T$ for binary tubules. These bending rigidity values are consistent with the estimate from the Helfrich model. In the main text, we showed contours corresponding to the model distributions overlaid on the experiment distributions in Fig. 3A and 4E; these come from the best fit target (m, n) given here and the average value of $B = 1.8 k_B T$ for the V- and X-tubules and $B = 3.8 k_B T$ for the binary tubule.

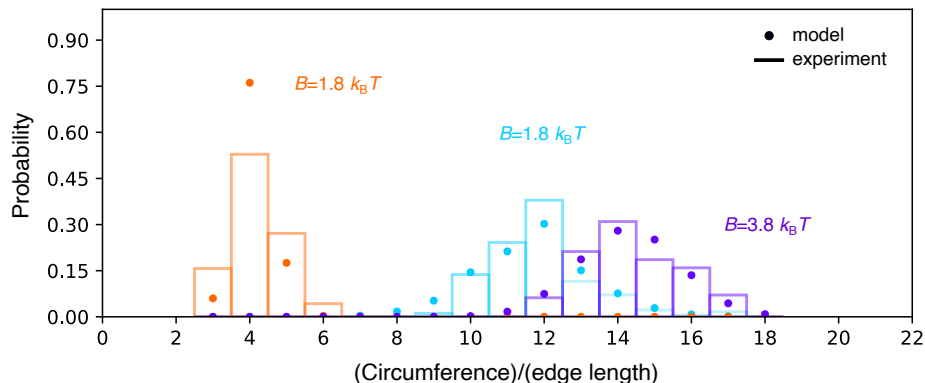


FIG. 14. **Estimation of the bending rigidity using the Helfrich energy.** Circumference distributions, shown as histograms, for the experimental V-, X-, and binary tubules are shown in orange, cyan, and purple respectively. Each distribution has a corresponding elastic energy model comparison, shown by the circles. The bending rigidity used to generate the model distributions comes from the Helfrich model estimate. For the V-tubule and X-tubule the B estimate of $1.8 k_B T$ comes from the average value of their respective Helfrich model estimates. The binary tubule value of $3.8 k_B T$ comes from the experimental distribution of the binary tubules.

Object	Concentration [nM]	# of refined particles	Dose (e/A ²)	Resolution of final 3D map [Å]
V-triangle	90	1228	25-35	23.48
X-triangle	170	3075	25-35	23.48
A-triangle	300	3627	25-35	19.97
B-triangle	150	1636	25-35	24.03

TABLE III. **Summary of cryo-EM reconstructions.** For each DNA origami structure used we have 3D reconstructions from cryo-EM. Here are listed the parameters summarizing each structure.

-
- [1] K. F. Wagenbauer, F. A. S. Engelhardt, E. Stahl, V. K. Hecht, P. Stömmner, F. Seebacher, L. Meregalli, P. Ketterer, T. Gerling, and H. Dietz, How We Make DNA Origami, *Chem Bio Chem* **18**, 1873 (2017).
 - [2] K. Günther, M. Mertig, and R. Seidel, Mechanical and structural properties of YOYO-1 complexed dna, *Nucleic Acids Research* **38**, 6526 (2010).
 - [3] J. R. Kremer, D. N. Mastrorade, and J. R. McIntosh, Computer visualization of three-dimensional image data using IMOD, *Journal of Structural Biology* **116**, 71 (1996).
 - [4] J. Zivanov, T. Nakane, B. O. Forsberg, D. Kimanius, W. J. Hagen, E. Lindahl, and S. H. Scheres, New tools for automated high-resolution cryo-EM structure determination in RELION-3, *eLife* **7**, e42166 (2018).
 - [5] A. Rohou and N. Grigorieff, Ctfind4: Fast and accurate defocus estimation from electron micrographs, *Journal of Structural Biology* **192**, 216 (2015).
 - [6] R. K. F. Lee, B. J. Cox, and J. M. Hill, An exact polyhedral model for boron nanotubes, *J. Phys. A: Math. Theor.* **42**, 065204 (2009).
 - [7] C. Sigl, E. M. Willner, W. Engelen, J. A. Kretzmann, K. Sachenbacher, A. Liedl, F. Kolbe, F. Wilsch, S. A. Aghvami, U. Protzer, M. F. Hagan, S. Fraden, and H. Dietz, Programmable icosahedral shell system for virus trapping, *Nature Materials* **20**, 1281 (2021)

Object	measurement	$\theta_{\text{side 1}}$	$\theta_{\text{side 2}}$	$\theta_{\text{side 3}}$	Estimated (m, n)	Experimental (m, n)
V-triangle	design	20.9	20.9	-10.8	(5,0)	(4,0)
	2 nd layer (PAM)	21.3 ± 0.1	21.3 ± 0.1	-5.5 ± 0.1	(5,0)	
X-triangle	design	10.4	10.4	-5.3	(10,0)	(9,4)
	2 nd layer (PAM)	11.4 ± 0.1	9.0 ± 0.1	-6.4 ± 0.1	(9,-1)	
A-triangle	design	10.4	10.4	-5.3	(10,0)	
	2 nd layer (PAM)	7.2 ± 0.1	4.2 ± 0.1	-0.4 ± 0.1		
B-triangle	design	10.4	10.4	-5.3	(10,0)	
	2 nd layer (PAM)	9.9 ± 0.1	9.7 ± 0.1	-5.0 ± 0.1		
2-species combined	2 nd layer (PAM)	8.6 ± 0.1	7.0 ± 0.1	-2.7 ± 0.1	(13,-1)	(13,2)

TABLE IV. **Summary of designed and measured bevel angles.** This table shows the bevel angles for the different triangle designs used in this research. The "measurement" column denotes if the following quantities come from the design, from surface estimates of the cryo-EM maps, or from fits to pseudo-atomic model (PAM). θ denotes the bevel angle of a given side. Estimated (m, n) shows which tubule type has the minimum deviation of angles from the given bevel angles. Experimental (m, n) is the tubule type that most closely matches the observed tubule distributions.

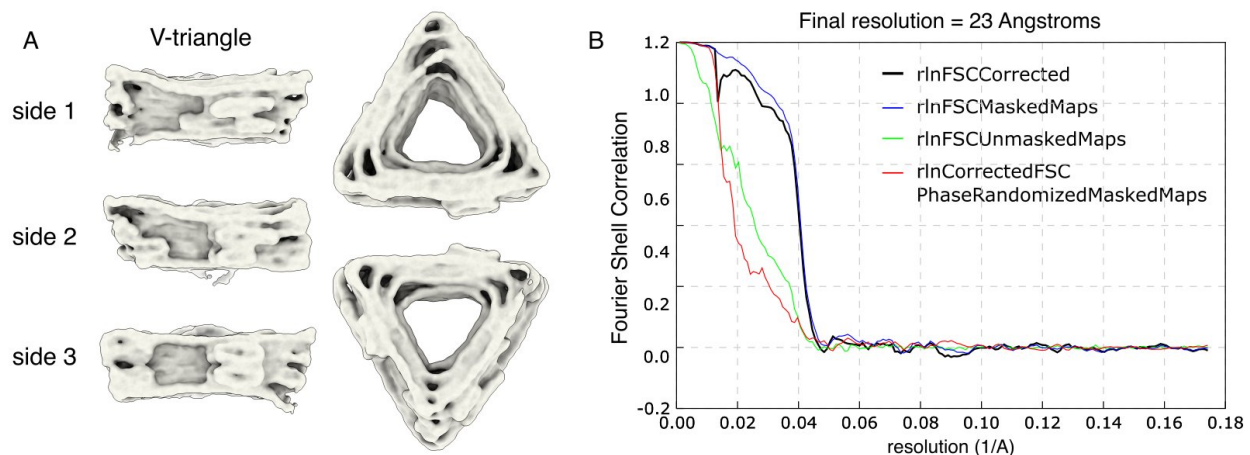


FIG. 15. **Cryo-EM reconstruction of the V-triangle.** (A) Electron density maps of the V-triangle shown from different viewing angles. (B) Plot of the FSC curves used to estimate the resolution for the V-triangle.

- [8] S. M. Douglas, A. H. Marblestone, S. Teerapittayanon, A. Vazquez, G. M. Church, and W. M. Shih, Rapid prototyping of 3D DNA-origami shapes with caDNAno, *Nucleic Acids Research* **37**, 5001 (2009)
- [9] T. E. Videbæk, H. Fang, D. Hayakawa, B. Tyukodi, M. F. Hagan, and W. B. Rogers, Tiling a tubule: how increasing complexity improves the yield of self-limited assembly, *J. Phys.: Condens. Matter* **34**, 134003 (2022).
- [10] J.-P. J. Sobczak, T. G. Martin, T. Gerling, and H. Dietz, Rapid Folding of DNA into Nanoscale Shapes at Constant Temperature, *Science* **338**, 1458 (2012).
- [11] J. SantaLucia, H. T. Allawi, and P. A. Seneviratne, Improved Nearest-Neighbor Parameters for Predicting DNA Duplex Stability, *Biochemistry* **35**, 3555 (1996).
- [12] F. Kilchherr, C. Wachauf, B. Pelz, M. Rief, M. Zacharias, and H. Dietz, Single-molecule dissection of stacking forces in DNA, *Science* **353**, aaf5508 (2016).
- [13] A. Briegel, M. Pilhofer, D. N. Mastrorarde, and G. J. Jensen, The challenge of determining handedness in electron tomography and the use of DNA origami gold nanoparticle helices as molecular standards, *Journal of Structural Biology* **183**, 95 (2013).
- [14] A. Kuzyk, R. Schreiber, Z. Fan, G. Pardatscher, E.-M. Roller, A. Högele, F. C. Simmel, A. O. Govorov, and T. Liedl, DNA-based self-assembly of chiral plasmonic nanostructures with tailored optical response, *Nature* **483**, 311 (2012).
- [15] M. Kube, F. Kohler, E. Feigl, B. Nagel-Yüksel, E. M. Willner, J. J. Funke, T. Gerling, P. Stömmer, M. N. Honemann, T. G. Martin, S. H. W. Scheres, H. Dietz, Revealing the structures of megadalton-scale dna complexes with nucleotide resolution, *Nature Communications* **11**, 1 (2020).

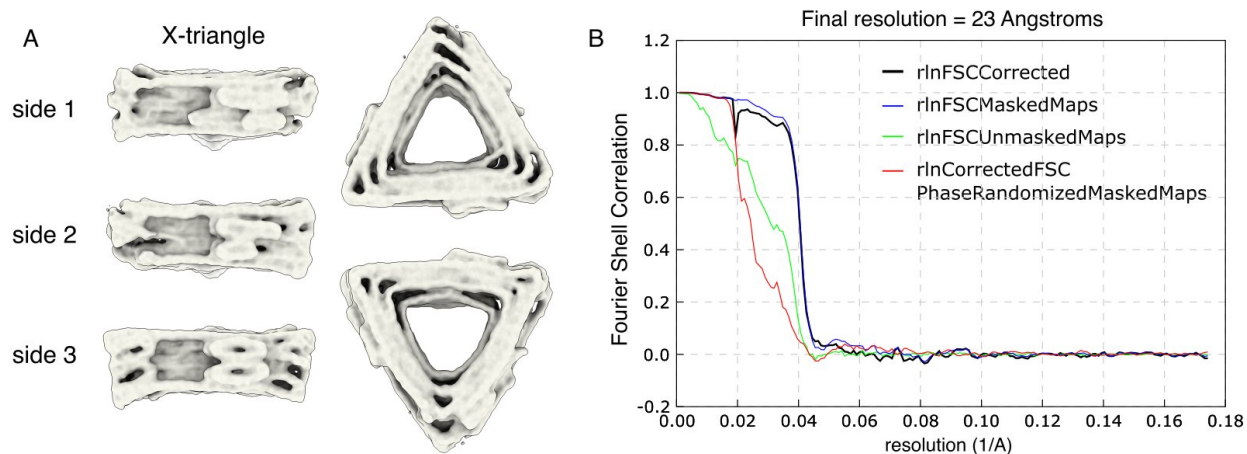


FIG. 16. **Cryo-EM reconstruction of the X-triangle.** (A) Electron density maps of the X-triangle shown from different viewing angles. (B) Plot of the FSC curves used to estimate the resolution of the X-triangle.

[16] C. Maffeo and A. Aksimentiev, Mrdna: a multi-resolution model for predicting the structure and dynamics of dna systems, *Nucleic Acids Research* **48**, 5135 (2020).

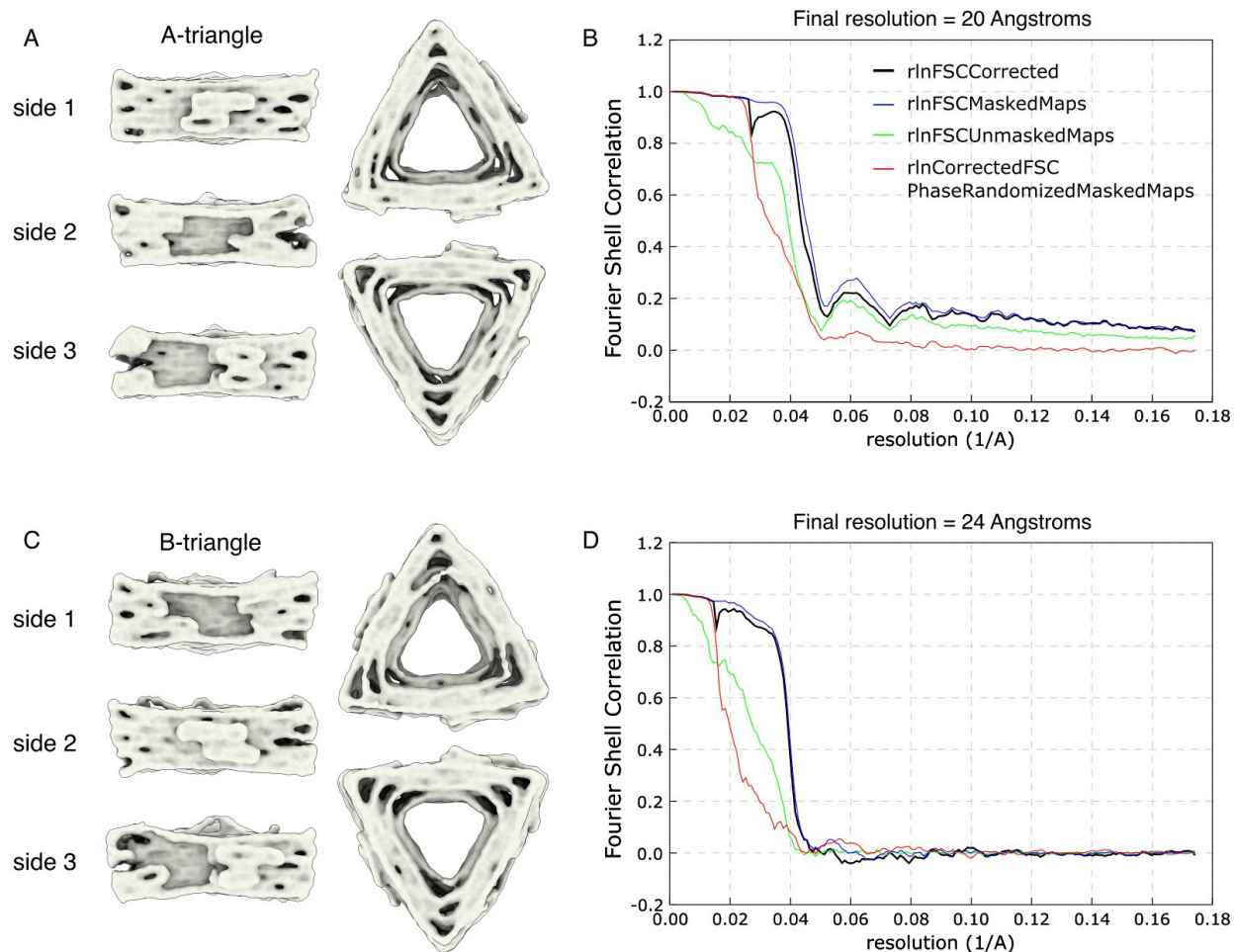


FIG. 17. **Cryo-EM reconstruction of the 2-species X-triangles.** (A) Electron density maps of the A-triangle shown from different viewing angles. (B) Plot of the FSC curves used to estimate the resolution of the A-triangle. (C) Electron density maps of the B-triangle shown from different viewing angles. (D) Plot of the FSC curves used to estimate the resolution of the B-triangle.

m	n	type	Side1	Side2	Side3	Tube Radius	Seam Angle
3	0	armchair	70.5288	70.5288	-38.9424	0.57735	90
3	1	chiral	34.8794	76.289	-25.2939	0.64526	76.4267
3	2	chiral	11.4318	70.0346	-10.0106	0.74313	66.6665
3	3	zigzag	0	60	0	0.86603	60
4	0	armchair	52.4484	52.4484	-27.6723	0.70711	90
4	1	chiral	30.8016	57.7027	-20.8118	0.78561	79.2816
4	2	chiral	15.0912	55.8337	-12.0981	0.88462	70.9921
4	3	chiral	5.4309	50.7492	-4.9378	1.0019	64.7355
4	4	zigzag	0	45	0	1.1315	60
5	0	armchair	41.8103	41.8103	-21.6246	0.85065	90
5	1	chiral	27.3046	46.0569	-17.5731	0.93259	81.1551
5	2	chiral	16.0536	45.862	-12.0747	1.0312	73.9826
5	3	chiral	8.2454	43.2505	-6.9803	1.1444	68.2498
5	4	chiral	3.1803	39.6875	-2.9532	1.2689	63.6781
5	5	zigzag	0	36	0	1.4013	60
6	0	armchair	34.7781	34.7781	-17.7989	1	90
6	1	chiral	24.4024	38.1678	-15.159	1.0832	82.4765
6	2	chiral	15.9669	38.6429	-11.4411	1.1808	76.1687
6	3	chiral	9.6541	37.3291	-7.7299	1.2909	70.9337
6	4	chiral	5.175	35.1086	-4.5289	1.4112	66.6031
6	5	chiral	2.0912	32.558	-1.9682	1.5392	63.0079
6	6	zigzag	0	30	0	1.673	60
7	0	armchair	29.7777	29.7777	-15.1445	1.1524	90
7	1	chiral	21.9995	32.5095	-13.3042	1.236	83.4572
7	2	chiral	15.4541	33.2418	-10.6588	1.3324	77.8349
7	3	chiral	10.2954	32.6383	-7.8818	1.44	73.0418
7	4	chiral	6.4037	31.2534	-5.3381	1.5568	68.9691
7	5	chiral	3.5464	29.4859	-3.1733	1.6811	65.5047
7	6	chiral	1.4808	27.5905	-1.4067	1.8112	62.5447
7	7	zigzag	0	25.7143	0	1.9459	60
8	0	armchair	26.0376	26.0376	-13.189	1.3066	90
8	1	chiral	19.996	28.2713	-11.8409	1.3903	84.2133
8	2	chiral	14.7784	29.081	-9.8827	1.4856	79.1461
8	3	chiral	10.508	28.8779	-7.7527	1.5909	74.738
8	4	chiral	7.1397	28.0234	-5.7144	1.7049	70.9154
8	5	chiral	4.5469	26.7963	-3.8979	1.8259	67.6008
8	6	chiral	2.5811	25.3912	-2.3465	1.9528	64.7196
8	7	chiral	1.104	23.934	-1.056	2.0843	62.2052
8	8	zigzag	0	22.5	0	2.2195	60
9	0	armchair	23.1338	23.1338	-11.6859	1.4619	90
9	1	chiral	18.3088	24.9873	-10.6601	1.5455	84.8137
9	2	chiral	14.0578	25.7944	-9.1641	1.6398	80.2044
9	3	chiral	10.4774	25.8206	-7.4941	1.7433	76.1307
9	4	chiral	7.5564	25.3093	-5.8424	1.8548	72.5412
9	5	chiral	5.2252	24.4584	-4.3174	1.973	69.3804
9	6	chiral	3.3914	23.4156	-2.9677	2.0969	66.5938
9	7	chiral	1.9623	22.2839	-1.8054	2.2255	64.1306
9	8	chiral	0.85495	21.1312	-0.82207	2.3579	61.9457
9	9	zigzag	0	20	0	2.4936	60
10	0	armchair	20.8135	20.8135	-10.4933	1.618	90
10	1	chiral	16.8731	22.3729	-9.6889	1.7015	85.3018
10	2	chiral	13.3463	23.1424	-8.516	1.7948	81.076
10	3	chiral	10.3088	23.3001	-7.1813	1.8967	77.2937
10	4	chiral	7.7644	23.0145	-5.8272	2.006	73.9176
10	5	chiral	5.6752	22.4284	-4.5415	2.1218	70.9073
10	6	chiral	3.983	21.6541	-3.3707	2.2431	68.2218
10	7	chiral	2.6252	20.7746	-2.3336	2.369	65.822
10	8	chiral	1.5422	19.8484	-1.432	2.4989	63.6723
10	9	chiral	0.68173	18.915	-0.65822	2.632	61.7409
10	10	zigzag	0	18	0	2.768	60
11	0	armchair	18.9167	18.9167	-9.5233	1.7747	90
11	1	chiral	15.6393	20.2449	-8.8771	1.8581	85.7062
11	2	chiral	12.6684	20.9633	-7.9374	1.9505	81.8062

m	n	type	Side1	Side2	Side3	Tube Radius	Seam Angle
11	3	chiral	10.0635	21.195	-6.8526	2.0509	78.2789
11	4	chiral	7.835	21.0594	-5.7298	2.1584	75.097
11	5	chiral	5.9628	20.6617	-4.6394	2.272	72.23
11	6	chiral	4.41	20.0877	-3.6231	2.3909	69.6467
11	7	chiral	3.1338	19.4038	-2.7018	2.5144	67.3168
11	8	chiral	2.0915	18.6593	-1.8824	2.6419	65.2117
11	9	chiral	1.2438	17.8896	-1.1636	2.7727	63.3055
11	10	chiral	0.55636	17.1189	-0.53898	2.9064	61.5751
11	11	zigzag	0	16.3636	0	3.0426	60
12	0	armchair	17.3372	17.3372	-8.7185	1.9319	90
12	1	chiral	14.5689	18.4809	-8.1889	2.015	86.0468
12	2	chiral	12.0335	19.1446	-7.4222	2.1066	82.4266
12	3	chiral	9.778	19.4156	-6.5274	2.2058	79.1239
12	4	chiral	7.8149	19.3807	-5.5863	2.3116	76.118
12	5	chiral	6.1343	19.1183	-4.6555	2.4233	73.3858
12	6	chiral	4.7129	18.6946	-3.7711	2.5401	70.903
12	7	chiral	3.5213	18.1629	-2.9536	2.6615	68.6456
12	8	chiral	2.5286	17.5643	-2.2126	2.7867	66.5907
12	9	chiral	1.7052	16.9294	-1.5502	2.9153	64.717
12	10	chiral	1.0244	16.2807	-0.96416	3.0469	63.0053
12	11	chiral	0.4627	15.634	-0.44948	3.181	61.4381
12	12	zigzag	0	15	0	3.3174	60
13	0	armchair	16.0012	16.0012	-8.0398	2.0893	90
13	1	chiral	13.6325	16.9958	-7.5984	2.1723	86.3375
13	2	chiral	11.4444	17.606	-6.963	2.2632	82.9602
13	3	chiral	9.4743	17.8954	-6.2154	2.3612	79.8563
13	4	chiral	7.735	17.9281	-5.4187	2.4656	77.0101
13	5	chiral	6.2226	17.7638	-4.6188	2.5755	74.4037
13	6	chiral	4.9222	17.4538	-3.8464	2.6905	72.0178
13	7	chiral	3.8136	17.041	-3.1206	2.8098	69.8333
13	8	chiral	2.8745	16.5595	-2.4519	2.933	67.8317
13	9	chiral	2.0825	16.0357	-1.8445	3.0596	65.9953
13	10	chiral	1.4167	15.4897	-1.2987	3.1891	64.3081
13	11	chiral	0.85835	14.9362	-0.81195	3.3213	62.7551
13	12	chiral	0.39086	14.3859	-0.38058	3.4558	61.3231
13	13	zigzag	0	13.8462	0	3.5924	60
14	0	armchair	14.8566	14.8566	-7.4596	2.247	90
14	1	chiral	12.807	15.7289	-7.0865	2.3298	86.5885
14	2	chiral	10.9001	16.289	-6.5527	2.4201	83.4239
14	3	chiral	9.1657	16.5839	-5.9208	2.5171	80.4971
14	4	chiral	7.6162	16.662	-5.2402	2.6201	77.796
14	5	chiral	6.2509	16.5691	-4.5482	2.7285	75.3064
14	6	chiral	5.0605	16.3457	-3.8709	2.8418	73.013
14	7	chiral	4.0312	16.0262	-3.2255	2.9593	70.9004
14	8	chiral	3.1466	15.639	-2.6224	3.0806	68.9533
14	9	chiral	2.3898	15.2068	-2.0669	3.2053	67.1572
14	10	chiral	1.7445	14.7471	-1.5609	3.3329	65.4984
14	11	chiral	1.1956	14.2734	-1.1036	3.4633	63.9643
14	12	chiral	0.72962	13.796	-0.69314	3.5959	62.5434
14	13	chiral	0.33456	13.3221	-0.3264	3.7307	61.2251
14	14	zigzag	0	12.8571	0	3.8674	60
15	0	armchair	13.8649	13.8649	-6.9579	2.4049	90
15	1	chiral	12.0742	14.636	-6.6385	2.4876	86.8074
15	2	chiral	10.3979	15.15	-6.1848	2.5773	83.8305
15	3	chiral	8.8604	15.4425	-5.6451	2.6734	81.0624
15	4	chiral	7.4727	15.5507	-5.0589	2.7752	78.4934
15	5	chiral	6.2361	15.5102	-4.4565	2.8822	76.1122
15	6	chiral	5.145	15.353	-3.8599	2.9938	73.9065
15	7	chiral	4.1899	15.1072	-3.2846	3.1097	71.8638
15	8	chiral	3.3588	14.7962	-2.7403	3.2293	69.9713
15	9	chiral	2.6389	14.4395	-2.233	3.3522	68.217
15	10	chiral	2.0174	14.0523	-1.7653	3.4781	66.5893
15	11	chiral	1.4823	13.647	-1.3377	3.6066	65.0774

m	n	type	Side1	Side2	Side3	Tube Radius	Seam Angle
15	12	chiral	1.0224	13.2328	-0.9494	3.7376	63.6713
15	13	chiral	0.62783	12.817	-0.59863	3.8707	62.3618
15	14	chiral	0.28961	12.4047	-0.28303	4.0058	61.1406
15	15	zigzag	0	12	0	4.1425	60
16	0	armchair	12.9974	12.9974	-6.5197	2.5629	90
16	1	chiral	11.4196	13.6836	-6.2434	2.6455	87
16	2	chiral	9.9348	14.1559	-5.8536	2.7347	84.19
16	3	chiral	8.563	14.4414	-5.3886	2.8299	81.5647
16	4	chiral	7.3141	14.5691	-4.8798	2.9306	79.1162
16	5	chiral	6.1903	14.567	-4.3521	3.0364	76.8356
16	6	chiral	5.1886	14.4607	-3.8244	3.1466	74.7128
16	7	chiral	4.3022	14.2733	-3.3101	3.2609	72.7373
16	8	chiral	3.5225	14.0242	-2.8184	3.3789	70.8988
16	9	chiral	2.8398	13.7299	-2.3551	3.5002	69.1869
16	10	chiral	2.2439	13.4038	-1.9234	3.6244	67.5919
16	11	chiral	1.7253	13.0568	-1.5248	3.7513	66.1046
16	12	chiral	1.2749	12.6976	-1.159	3.8807	64.7161
16	13	chiral	0.8843	12.3327	-0.82535	4.0122	63.4186
16	14	chiral	0.54595	11.9674	-0.52222	4.1456	62.2045
16	15	chiral	0.25316	11.6055	-0.24777	4.2809	61.067
16	16	zigzag	0	11.25	0	4.4177	60
17	0	armchair	12.2321	12.2321	-6.1335	2.7211	90
17	1	chiral	10.8314	12.8467	-5.8923	2.8035	87.1706
17	2	chiral	9.5074	13.2812	-5.5544	2.8923	84.51
17	3	chiral	8.2764	13.557	-5.1503	2.9867	82.0138
17	4	chiral	7.1472	13.6968	-4.7055	3.0865	79.6758
17	5	chiral	6.1225	13.7228	-4.2408	3.191	77.4885
17	6	chiral	5.2009	13.656	-3.7719	3.3	75.4437
17	7	chiral	4.3779	13.515	-3.3108	3.4129	73.5327
17	8	chiral	3.6469	13.3163	-2.8658	3.5293	71.7469
17	9	chiral	3.0006	13.0737	-2.4426	3.6491	70.0775
17	10	chiral	2.4312	12.7991	-2.0445	3.7718	68.5161
17	11	chiral	1.9309	12.5021	-1.6735	3.8971	67.0549
17	12	chiral	1.4922	12.1903	-1.33	4.0249	65.6861
17	13	chiral	1.1081	11.8702	-1.0138	4.1549	64.4028
17	14	chiral	0.77237	11.5465	-0.7241	4.2868	63.1984
17	15	chiral	0.47911	11.2231	-0.45955	4.4206	62.0668
17	16	chiral	0.22318	10.903	-0.21872	4.556	61.0024
17	17	zigzag	0	10.5882	0	4.693	60
18	0	armchair	11.5519	11.5519	-5.7907	2.8794	90
18	1	chiral	10.3002	12.1054	-5.5783	2.9617	87.323
18	2	chiral	9.1123	12.506	-5.283	3.05	84.7968
18	3	chiral	8.0018	12.7707	-4.9292	3.1438	82.4178
18	4	chiral	6.9765	12.9173	-4.5379	3.2426	80.1811
18	5	chiral	6.0392	12.964	-4.1264	3.3461	78.0805
18	6	chiral	5.1896	12.9277	-3.7081	3.4538	76.1091
18	7	chiral	4.4245	12.8238	-3.2934	3.5654	74.2598
18	8	chiral	3.7393	12.6662	-2.8898	3.6805	72.525
18	9	chiral	3.1283	12.4667	-2.5028	3.7988	70.8976
18	10	chiral	2.5853	12.2356	-2.1358	3.9201	69.3703
18	11	chiral	2.1042	11.9812	-1.7908	4.0439	67.9361
18	12	chiral	1.6787	11.7107	-1.4689	4.1702	66.5885
18	13	chiral	1.3031	11.4298	-1.1701	4.2988	65.3212
18	14	chiral	0.972	11.143	-0.89424	4.4293	64.1285
18	15	chiral	0.6804	10.854	-0.64038	4.5616	63.0049
18	16	chiral	0.42383	10.5658	-0.40753	4.6957	61.9453
18	17	chiral	0.19824	10.2806	-0.19449	4.8313	60.9451
18	18	zigzag	0	10	0	4.9683	60
19	0	armchair	10.9434	10.9434	-5.4842	3.0378	90
19	1	chiral	9.8182	11.4445	-5.2959	3.12	87.4598
19	2	chiral	8.7466	11.8146	-5.0358	3.2079	85.0551
19	3	chiral	7.74	12.0674	-4.724	3.301	82.7832
19	4	chiral	6.8052	12.2173	-4.3778	3.3991	80.6397

m	n	type	Side1	Side2	Side3	Tube Radius	Seam Angle
19	5	chiral	5.9452	12.279	-4.0115	3.5016	78.6197
19	6	chiral	5.1602	12.2663	-3.6368	3.6082	76.7174
19	7	chiral	4.4481	12.1922	-3.2627	3.7185	74.9267
19	8	chiral	3.8056	12.0683	-2.896	3.8323	73.2414
19	9	chiral	3.2283	11.9047	-2.5417	3.9493	71.6551
19	10	chiral	2.7113	11.7103	-2.2031	4.0692	70.1617
19	11	chiral	2.2497	11.4926	-1.8825	4.1917	68.7551
19	12	chiral	1.8384	11.2578	-1.5811	4.3166	67.4297
19	13	chiral	1.4726	11.0112	-1.2994	4.4437	66.1798
19	14	chiral	1.1477	10.7571	-1.0374	4.5728	65.0003
19	15	chiral	0.85945	10.499	-0.79459	4.7038	63.8863
19	16	chiral	0.60393	10.2396	-0.57038	4.8366	62.8334
19	17	chiral	0.3776	9.9811	-0.36387	4.9708	61.8373
19	18	chiral	0.17725	9.7254	-0.17409	5.1065	60.894
19	19	zigzag	0	9.4737	0	5.2436	60
20	0	armchair	10.3959	10.3959	-5.2087	3.1962	90
20	1	chiral	9.3789	10.8515	-5.0406	3.2783	87.5833
20	2	chiral	8.4074	11.1943	-4.81	3.3659	85.2891
20	3	chiral	7.491	11.435	-4.5335	3.4585	83.1151
20	4	chiral	6.6356	11.5856	-4.2255	3.5557	81.0577
20	5	chiral	5.8441	11.658	-3.898	3.6573	79.1128
20	6	chiral	5.1172	11.6638	-3.561	3.7629	77.2754
20	7	chiral	4.4535	11.6136	-3.2225	3.8721	75.5405
20	8	chiral	3.8506	11.5174	-2.8885	3.9847	73.9027
20	9	chiral	3.3053	11.3838	-2.5636	4.1004	72.3566
20	10	chiral	2.8136	11.2205	-2.251	4.219	70.8968
20	11	chiral	2.3715	11.0342	-1.9531	4.3402	69.5181
20	12	chiral	1.9749	10.8305	-1.6711	4.4638	68.2153
20	13	chiral	1.6197	10.6141	-1.4058	4.5896	66.9837
20	14	chiral	1.3021	10.3889	-1.1575	4.7174	65.8186
20	15	chiral	1.0185	10.1582	-0.92588	4.8471	64.7157
20	16	chiral	0.76535	9.9248	-0.71068	4.9785	63.6709
20	17	chiral	0.53965	9.6907	-0.51125	5.1115	62.6804
20	18	chiral	0.33854	9.4576	-0.32687	5.246	61.7406
20	19	chiral	0.15943	9.2271	-0.15673	5.3819	60.8482
20	20	zigzag	0	9	0	5.519	60

TABLE V: **Summary of bevel angles, tubule radii, and seam angles for different tubules.** Bevel angles and seam angles are in the unit of degrees. Tubule radius is in units of the monomer edge length. To get opposite chirality tubules, $n < 0$, swap the bevel angles of sides 1 and 2.

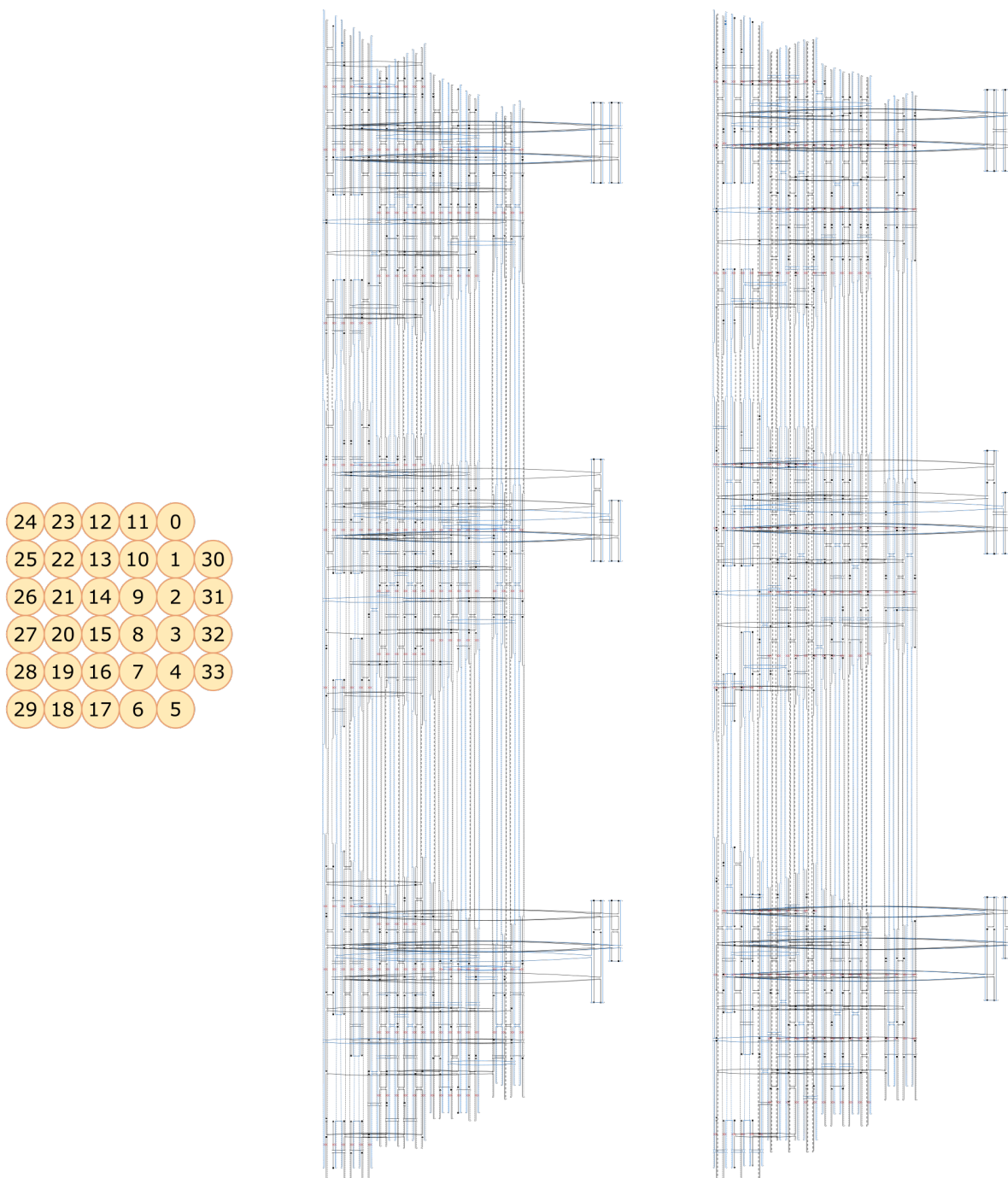


FIG. 18. Helical numbers and caDNAno designs for V-triangle (middle) and X-triangle (right).

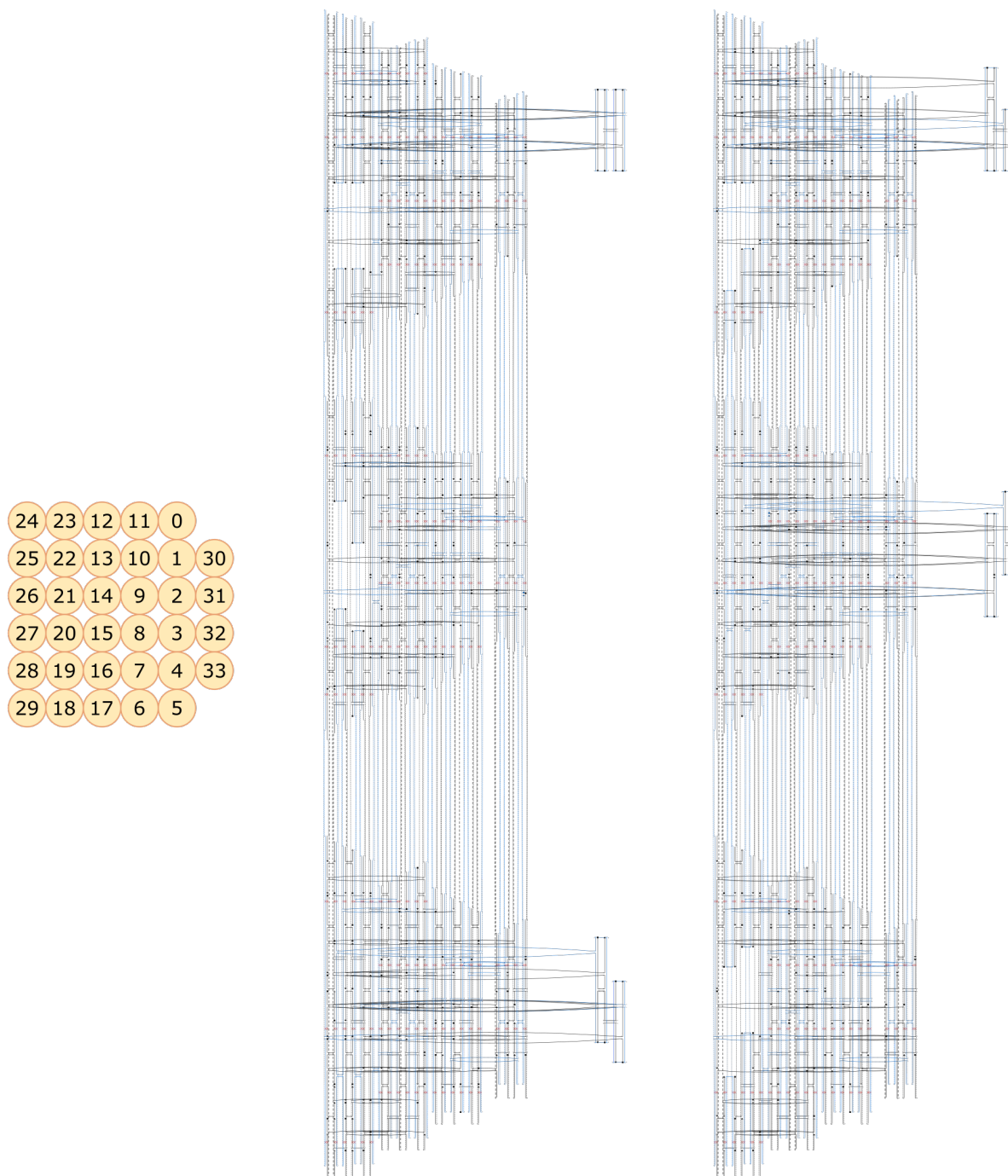


FIG. 19. Helical numbers and caDNAno designs for A-triangle (middle) and B-triangle (right).

Name	Sequence
Core 1 Side1 1	TAATCAGTTTAGAATCAGAGCGGGAGCTAAAGAAAGGAAGGGAAGACCGTAAAG
Core 1 Side1 2	CGCATCGTTTTGCCGCCATCAACATAAGGTGGCAACATCAG
Core 1 Side1 3	GCTTGACGGGGAAAGAGCCCCCGCAATATAAGGAATTATCAAACAATGATTTAGA
Core 1 Side1 4	CCGCCGGGATTGCAGGAGGTGTCCAGCATCAGAGACAGGAACGGTACG
Core 1 Side1 5	CACTCAATCGGCAATGAAATAGCAATAGAAAATACATA
Core 1 Side1 6	TGCTCATAAACCGTGTGACCGTGAAGATCGCACTCCAGCCAGCTT
Core 1 Side1 7	AAAAAGAGAAAAGCCGCCGCAAGAATGCCAAC
Core 1 Side1 8	CGTGCGCACAGGAGGCCAGAATCCTGAGAAGTGTTTTTTA
Core 1 Side1 9	CGATTAAAGGGATTTTAATAACCAATTTTACATTAATGGAATTGTTTGG
Core 1 Side1 10	AGAAAATTCGCCTGATTGCTTTGCGGGGTC
Core 1 Side1 11	ATAAACAGTAAATTTTCGTGTACATGTGCCATCCCACGCAACCAGCTT
Core 1 Side1 12	AATTCATATTTAGACGCGGAGCCAGCTTTC
Core 1 Side1 13	AACCACCATCAGCAAATCGGAACCCTAAAGGGCCGCGGAAACAGTACC
Core 1 Side1 14	CCTTATCTACCAGCGCCAAACCTGAAAATTC
Core 1 Side1 15	ACCTTGCTGAACCTCAAATATCATGCGGCTGGTATGAGC
Core 1 Side1 16	AGTATTAAATCAATACAATCAATTTTCTGATTGTTTGGC
Core 1 Side1 17	AAGTTTATTTTGTACAGTAAGCAATGATGGCAACAATAA
Core 1 Side1 18	GATAGCCGAGCCCTTTTTAAGAAATTCTGAACGGGAGA
Core 1 Side1 19	ATTATACGACTTTACATCATAATCTGGTCAGTTGGC
Core 1 Side1 20	TACCTATCTTACCGAAACAAAGTTACCAGACCCACAC
Core 1 Side1 21	TGTAGGTAAAGATTCACCCAGTCACGACGTTG
Core 1 Side1 22	AAAGCGCCAGGCTGCCGTGCGGTCGACATAAAAAAATC
Core 1 Side1 23	ACTAGAAAAGCCCTGTGTAAGGTTTCATAATTAAGCATC
Core 1 Side1 24	TTAGTATCATATGCGTTATACAAAGATAATCACGGGTCAC
Core 1 Side1 25	GGAAGGTATGTTGCCAACGACAAAAGGGCGA
Core 1 Side1 26	GAGGGAGAGTATAAAGCCAACGCTCAACAGAGGCTATCAAAGGTGA
Core 1 Side1 27	TTAAATACCGAACGCCTAAAACATCGCCAT
Core 1 Side1 28	CACCGGAATGGTGTGTGAAGGAGCTCCTAATTTTCCCTTAATACAGTA
Core 1 Side1 29	GGCCTTCCTATATAAAGAAACGCAAAGAAT
Core 1 Side1 30	TAAATGTAAATAATTTAAAATATATGTACCCCGTTTTTCTTACC
Core 1 Side1 31	AACAACCCATCAAACCTCCATATTAAGAATTGAGTTAAGCCCAATAAGGCGGTT
Core 1 Side1 32	CACTAAATCGTTAACGGCATCAATAAGGCG
Core 1 Side2 1	CCAGAGCACATCCTCATAACGGAAGTTAAACGATGCTGATTGCCGT
Core 1 Side2 2	AGTAGCATTAAACATCCAATAAATCAGGTAGAGGTCATTTATTACCTTAGCTTGCT
Core 1 Side2 3	GTGGCATCAATTCTAAAAATAGCAGAGTACCTTATAACCACAAAAGGA
Core 1 Side2 4	AGTCCCGGAAAATAGCATTAACTGAACACCCCTGAACAAA
Core 1 Side2 5	AGCGCCATGTTTACCATCGGCGATCAAGATTTTTTAGCGAAGCCGTTACCGCACT
Core 1 Side2 6	AGCTAAATAAGCAATACAAGGCAAAGAATTAGCGTCTCGTCTGGCA
Core 1 Side2 7	GAGCATAAAAAGACGTTAGTAAATGAATGTAGTTTATC
Core 1 Side2 8	ACGCGGTCCGTTTTTTTACGGGAGAAGCCTTTA
Core 1 Side2 9	TTCCAAAACAGGGAAGCGCATTAGCAAAAT
Core 1 Side2 10	TTAACGTCAAAAATGAATTTGTGTCCGGCAAGCCTCCGG
Core 1 Side2 11	CTCAGAACGTTAGCGTAAACGATCTAAAGTTTGGCTTAG
Core 1 Side2 12	CCTTAAAAACGTACCGGTTAATCATTGTGA
Core 1 Side2 13	TTCGAAGTTTTAGCGATTTTGCTAAACAACCTACAATTCAGAGAG
Core 1 Side2 14	CGAGCATTAAAGAACATTTTTAGAACCTCACCGGAAACA
Core 1 Side2 15	ATCCCATCGCCTGTTTATCAACAATAGATAATTTTGGCGAAAAACAT
Core 1 Side2 16	ACCGATATATTCGCTGCCATCGCC
Core 1 Side2 17	GTCCGTCGCTGAGGCTTGCAGGGAGTTAGAACCGCCACCCAGAATGGA
Core 1 Side2 18	CATCGAGGACAACAAAACAAGAACGACTTGCTTTGTACC
Core 1 Side2 19	ATTTACCGTTCAGTAAGCGCAGGTTAATGCTAAATTTGTTTAAAGAA
Core 1 Side2 20	CGAGAATGTTTTGCAAAAAGAAGTTGGCGCGAGCTGAAAAG
Core 1 Side2 21	TAGTTGCGCCGACAATTTCAACAGTTTGAAGAATAACAT
Core 1 Side2 22	GAGTGAGAATAGAAAATAAGCTTGATACCGACACGACATA
Core 1 Side2 23	GGAACAACCTTGATCGCCGCCACCCTCCTTTTAGCTTAATTTGCTGAAT
Core 1 Side2 24	TTATCCTGTATTTTGCACCCAGCAACAAGCAACCTCCAAATAAT
Core 1 Side2 25	TCATCAGTGAATAAGGTTGGGAACCTGGCTCATTTAATTG
Core 1 Side2 26	GACGTGACAATCATAAGGGAACCAGAATCATCCCTCAG
Core 1 Side2 27	TCAGACTGACGAGGCGCAGACGGTCCCCCAGC
Core 1 Side2 28	ATATAAAGAGAGAGCAAAAATCAGGATAAAAAGCGAGGCGAGTAAAGA
Core 1 Side2 29	GAGAATTACCATGTAATAAGAGACAGAACGCTCAATTTA
Core 1 Side2 30	GGCCGCTAGCAGACCGTAATCAGTAGCGACGAACCTGAACAGCATCACGAGTAG
Core 1 Side2 31	AGCCGCCACCCTCAAAAAGCGAAAAGCCAACCTT

Name	Sequence
Core 1 Side2 32	GGGAATTTACCGACAATTTAGGCAGAGGCATTTTCGAG
Core 1 Side2 33	TATGACCCATTTCAACGGGGGTGAATTTCTTAAACAACATCTCTGACCTCAGC
Core 1 Side2 34	TTTATTTCAACGCAACCAGTAGCACCAGCC
Core 1 Side2 35	CTTAGAAACACCAGAGGAACGAGTTAAAGCC
Core1 Side12 1	ACGTGCCGGACTTGTAGAACGTCAGCTTGTGGTGTCTGGTCA
Core1 Side12 2	GGCGATCGGTGCGGGCGCAACACAGGCGGCCTTTATTGTGATGAAGGGTAA
Core1 Side12 3	CTCTTCGCTATTATTCCGCCAGCTGGCGAGGGTAACGC
Core1 Side12 4	ACAGCGGGTCGGATTATGTTAGATAGAAGGCTTTTATCCGGTATTC
Core1 Side12 5	AGAGATAGACTTTCTGCCACGGGACTCCTTATTTTACGCAGACGGCCAG
Core1 Side12 6	TAACCCACTTTATCCCAATCCAAATAAGATTAACGATTTTTTTGT
Core1 Side12 7	GTCAGAGGGTAATTGAGTTCGCTAATATCAGAGAGACCGTAAAAACGCAGAA
Core1 Side12 8	GTAGAAATTTCCAATCAATAATCGGCTGTCTTTAGCAAGCAGCCATCAAGAGCGAGT
Core1 Side12 9	CATTC AACCGAATAAACAACATGTTTTTCAGCTAATG
Core1 Side12 10	CAGGGTTTTAAAGTTGGTGAGAAAGGCCGGAGACAGTCAAATATATATTTAGCCATTT
Core1 Side12 11	CACGGAATATATGGTTATTCCAAGAACGGGTATTTTAAACCAAGT
Core1 Side12 12	TTTATTTTCATCGTATTGGAATCATTACCGCGAGGAAACCGAAAATAC
Core1 Side12 13	AATCTTACCAACGCTAACGAGCGTTTCTTTCCAGAGCCTAATTTGCCAGT
Core1 Side12 14	TAAATTAATGCCGGTTAGAGGGTAGCTATTT
Core1 Side12 15	AAAAGGTTTTAAAGTAATTGAGAATCGCCATATTTTTTAAACAACGC
Core1 Side12 16	ATAGGAACAATCAGATCAAACGTAGAGGAAACGCAATTTAATAACGGAATACCCATGC
Core1 Side12 17	TAAATGCATTATGCCTGAGTAATTTTTTAAACCAATTATCACCCTCACCAGCTTTTG
Core 2 Side3 1	ATTCTGCGAACGAGTATAACAGTTGATTTCCAGTTTTCGTCACGGATA
Core 2 Side3 2	AGAAGAACATTGCCCTCCGCGCCAGCTGCAATAGTGAATTTAGGAATAAATCA
Core 2 Side3 3	GAAAGACTTCAAATAATTAAGAGTCAGTACCGCTGAGACTAAGTTTT
Core 2 Side3 4	TCACGCTGAAATTGCGAAAGAAGATGATGAAACAAACATCGCCGCTCACCACA
Core 2 Side3 5	TGACGAGTGGCAAGGAATAGCTGAACCACGGTTTGC
Core 2 Side3 6	CACGTATATTGTAGCAATACTTCTTTGATTAAATCAAAATGTAGCGG
Core 2 Side3 7	CAAAACATGTACCGTAACACTGATATCCAG
Core 2 Side3 8	CAATAGGAAACAGGAAAACAATATTCGGCCTTGTCTGGTAA
Core 2 Side3 9	TACATTTAACAACAGAAAGAGTCATTAATGGCTACT
Core 2 Side3 10	GAGAAGGAGGACTCATTACGTAATGCCACTA
Core 2 Side3 11	TTATCAAATCATAGGTCTGTAATAACAACAGTTAATGAAAAC
Core 2 Side3 12	TGCAAGGATATATAACTTTAACCTCCGGCTTAAACAGTACTTAGCGGG
Core 2 Side3 13	AGGAGCACTTTTAAAATGCGTTGCAATCGGCC
Core 2 Side3 14	AGAACCACGCCTTGATATTCACAAATGAAAGTCCAACCTAGGATTGCA
Core 2 Side3 15	CAGCATTGAATCGTCTGGAATAACCTACATTTTCCAGTGC
Core 2 Side3 16	ACAAAGAACGGCAACAGTGCCACATATCTTT
Core 2 Side3 17	TGATAAGGAGGTGTAGGTTGGGTGGTTGAGG
Core 2 Side3 18	TAACCTTGACGCTGAGAAATAAAGCGCGTAACACAGGGCGATCACTTGCCTGAGT
Core 2 Side3 19	ATATAAGTATAAGTGCCGTCGAGCTGGTAATCCTCAACAGGTCAGGTAATA
Core 2 Side3 20	TACTTTTTTTAAATGGAAGGGTTGGCAAGCCGTTTTGC
Core 2 Side3 21	ATTTGAATATATATGTGAGTGAATATAGAGACTACCTT
Core 2 Side3 22	GGTGCCATATGAGTGACCGGGGTTTTCTGC
Core 2 Side3 23	ATTAGCGTTTGCATCGATTACACAGTACACATTATTTACATTTGGCA
Core 2 Side3 24	GAGATAGAACCCTTCTGACCTGACAGCACGCCTGACCTAACATTAAT
Core 2 Side3 25	AAGCGTAACGGTCAGTATTAACACCGCCTCGATTATCTT
Core 2 Side3 26	AAGTTTCCCGAAGGCAATTAAGAGAGGTTTTACGTTGAAACCACCACCTAATTCGA
Core 2 Side3 27	ATTAACGGACGATTGCACCAGAGCCGCCGC
Core 2 Side3 28	TCAAAAAGTCGCGTTTCTCATTTTACCAGTACAACTACAACGCCTG
Core 2 Side3 29	GAAGCCCAAACGAACCTGTCTGGCCATTGCACCTTAAT
Core 2 Side3 30	TCACCCAGCGGTGAGCTAACTCAATTTAATGGTTTGAGGTTGAGG
Core 2 Side23 1	ATAACCTGTTTAGCTTTTTTTTTTTCATTTGGTTGCCAGAGTTTTTTTTTAAATAGTAAAATG
Core 2 Side23 2	AGCAAATTTTCCAACAGGTCAAACATGTTTTTATTTTTATGCAACTATGGTCA
Core 2 Side23 3	GTGTTCTGGTAGCTATCCACTTTGACAGCCCACTA
Core 2 Side23 4	AAGTTTCGCTTCAAAGCGAACAGTCAGAAAAAAAATTGGCTCATCAAAA
Core 2 Side23 5	CGCCACCCCTCAGATTTCCGCCACCCCTCAGAGATCTCCAGCAAAGC
Core 2 Side23 6	CCCCTGCCGCCTTTAATAAAGGATTTTTTTCGAATAATAATTTCCG
Core 2 Side23 7	TATTTCCGGAACCTTTTTTATTCTGAAAC
Core 2 Side23 8	ACAAATAATTTTCTCAGGTAGCAAACCGCCAGTTTGCCTTTAGCG
Core 2 Side23 9	TCAGAGCCACACTTTTTTCAGAGGGCCACCTTTTCATATCATGAGG
Core 2 Side23 10	AAGCGTTTTTTTTTATGCTTTTGAACCGGGTCAGTGCTTTTTTTGTAAACAGTGCCCGTA
Core 2 Side23 11	TCCCCCTCAATTTTTTTTTTAAACAGTTCAGAAAA
Core 2 Side23 12	ATAGCCCGGAATAGGTGTTTTTTTTCCGTACTCAGGAGGTTTATTTCTGTATGG

Name	Sequence
Core 2 Side23 13	GATTATACCAAGCGGATTTTTTAAAGTACACCATGTTTTTTTTAGCCGGA
Core 2 Side23 14	ACCTGCTACGGAGATTTGTAATACACTTTAAAACACTCAT
Core 2 Side23 15	TAGCGGTTTTTTTTTCGGCATTTCGGTCATAAATCCGCG
Core 2 Side23 16	ACGGCTACAGATTTGCTTTGAGGACTAAAGACTTTTATCAAAA
Core 2 Side23 17	ATCAGGTCTTTTTTCTGCTGATTTGAATTTAGACTGGATAGCTTTCGCAAAAAGTACG
Core 2 Side31 1	GAGGCCACCGAGTAAATTTTTTCTGTCCATCAGGCAATGTTGTTCCAGT
Core 2 Side31 2	ACAAGAGTCAAGGGCGAATTTTTTGTCTATCAGGGCGATGGC
Core 2 Side31 3	CCTGAGCATAGATTTTCAGGTTTATTTTCGTCAGATGAAT
Core 2 Side31 4	GTTACAAAATCGCGCAGAGGCGAATTTTTTCATTTCAATTA
Core 2 Side31 5	GAATCCTTGAAATTTTCATAGCGATAGCTTAACATTATCATT
Core 2 Side31 6	GTTTGAGTAGATTAAGCTTCTGTATTTTTTGTGCGCTATTAATTGA
Core 2 Side31 7	GCGGAACAAAGAGGAATTGAGGAATTTTTTATCTAAA
Core 2 Side31 8	AAATCAACCATTTGAGTCGACAACCTCGTATTTTTTTTTCTTTGCCCGAACGT
Core 2 Side31 9	GCTGAGATTTTCAGCAGCAAATGAAAAATCTTAAAAATAAGAATAAA
Core 2 Side31 10	TATATGTATAATAGATTAGAGCCGTCTTTTTTTATAATAAGTTGAAA
Core 2 Side31 11	CCACTACGCCGAGATAGGGTTGAGATTAACCGACGTGCTTTTTTTTTCG
Core 2 Side31 12	GGGTTAGAACCTACCTTTTTTCAAATTTATTTGCACGTAAAATTTTC
Core 2 Side31 13	CCGGTGCCCCCTGCATCAGACGATTTTTTGCAGCAGTGT
Core 2 Side31 14	CGGCCAGAATTTTTTGCGGGCCGTTTTTCACGGTTCAT
Core 2 Side31 15	TGCGCGAACTGATAGCAACCACCAGCAGAAGATAATTTACAGA
Core 2 Side31 16	GAATACGTGGCACAGACAATATTTTTTTTTTTGGCTATTAGTCTTTAA
Active Hubble1 1	CGCGGATCATCCATTATTTTCGCTGCCAGTTTGAGGGGACGACGAC
Active Hubble1 2	AGTATCGGCCTCAAATGGGATATATTTTGTGCGCTCTAATATTGACGGAAAT
Active Hubble1 3	TCCAGACGACGACATTTATTCATTTGTCAATCTCGCATTAATTCGTAA
Active Hubble1 4	AACTAGCAAGGTCATTTGAACGGTAATTTTTGGGAACAAA
Active Hubble1 5	GTGCCGAAACCAGGCTCCGGCACTCTCCGTG
Active Hubble1 6	GGCAGCACGCAACTGTTGGGAAGTAAAACGCGCTTCTG
Active Hubble1 7	CAAACAAGAGAATCGAGCCTGAGAATCTACAATAGGGCTTAATTTCTG
Active Hubble1 8	TAAATCAGCTCATGTTGAGAGGTCGGAG
Active Hole1 1	GTGTAGATGGGACGGCTGGCGCTTTCGAGCAGTTGTAAGAGCA
Active Hole1 2	GAAAAAGCCTAAATTTGTAACGTTAAGGTCACGTTG
Active Hole1 3	TGTATAAGCCTTACACTTCTTTGCTCGTCATGTAATGG
Active Hole1 4	AAACATCCAAATATTCAAAAACAGGAAGAT
Active Hole1 5	AATCAAGTTTTTTTTTTGGGAACGTCACACTATTAAGAACG
Active Hole1 6	TGGACTCCTCGAGGTGAAGCGAAAGGATTTTGGGCGCTAGGGCGC
Active Hole1 7	AATACCGTTTCCGGGTGCTGCACTGCGCGCCTGTG
Active Hole1 8	CACTCTGTTGTGATAAGATGCCGGTTTTTCTGTCAGCCA
Active Hubble2 1	GAAAAATCGACGCAACTATCATAACCCTCGAAGTTTCTATCAGT
Active Hubble2 2	TGAGATTTAGGAAATAAAACGAACTAACGGAA
Active Hubble2 3	GATAAGATTTACCATACGTTATAACCACATAGAGTAATCTTGACAAGAACC
Active Hubble2 4	GGATATTCATTACGACAGATGCCATCGATTTTGGGGTGTAATAC
Active Hubble2 5	ATTACGAGGCATAGTACATAACGCGTCAGGACCTTGCCCT
Active Hubble2 6	ATAATGCTGTAGCTCGGATTAGGAGAGGCACCATAACAAAAGGA
Active Hubble2 7	CTGCTCATTCACTAATAATGCAGATAAGAGCAACTAAAAACCCTAATAGT
Active Hubble2 8	ATGCGATGCTTGAGCTGACCTGAAAGAGCCAAATCAACGTAAACAAAG
Active Hole2 1	CAACATTATTACATACAGGAAGCCTCATTGCGGATTTGCTGCT
Active Hole2 3	GACCAGGCGCATAGGCTGGATGGTTTTAATCGTCAC
Active Hole2 4	CCATAGCAAGGCCGAAACGTCACCAATGAAAAACGGTGTACA
Active Hole2 5	TGCCAAGCTTTCTTAGAGATTAAGTTAAGGGGGATGTGCTG
Active Hole2 6	CAAGGCGGTGGAGCCCCGTGGTGAAGGGATAGTTCTCTCACGG
Active Hole2 7	ACTGGCATGATTAAGAACGGATAACCCTCCACCATCAATATG
Active Hole2 8	ATATTCAACCGTTCTAGCTGACAACATGT
Active Hubble3 1	CGCCAGGGGCAAAATGTTTGTATGGTGGTTCTCACCGCTGGCC
Active Hubble3 2	CTGAGAGAGTTGCTCTTTTTACCAGTGAGACG
Active Hubble3 3	CGAAATCTGGTTTTAGCAAGCGGTTGAGGATCCCCGGGTACCG
Active Hubble3 4	AGCTCGAATTCGTTTGTATCGGCCAACATTTTCAAATGACGCTCACAATCCA
Active Hubble3 5	CAGGCGAAAATCCCCCTTATAGTAATAACCGTACTATGGTTGCTT
Active Hubble3 6	GTTTCCTGAAAGTGATCCTCACAGTCCACGCTGGTTTGCCCCAG
Active Hubble3 7	GCGTCCGTGAGCCAAGCCTGGGTATTGGGAACGCGCGGGGAGAGG
Active Hubble3 8	GAAGCATTGTGAAAAATCATGGTCATAGCTGTGCCTGTTCTTC
Active Hole3 1	GGCAACAGCTGTCAAACATATACCAGCCAGCTTGAATGCAAGAAAA
Active Hole3 3	CCACACAACATACGAGCCGCCGCTTTATATTTTTAATGCTGAATCGCAAG
Active Hole3 4	GAAATGGGACCAGTAATAAAAGGGACATTTCTCGCTCACAATT

Name	Sequence
Active Hole3 5	ATTCCATAGATTTAGTTTGACCATTAGATACAGTCCAATACTG
Active Hole3 6	CGGAATCGTCATAAATATTACTATTATAGACCGGA
Active Hole3 7	AAACGAAAGAGGCCAAAAGATCATCGCCTGATA
Active Hole3 8	AATTGTGTCGAGCCCCCTTTACCCGGAACCAGTTTGCCACCACCGG
Passive Hubble1 1	CGGCGGATCATCCATTATTCGCTGCCAGTTTGAGGGGACGACGACTTTTT
Passive Hubble1 2	TTTTTAGTATCGGCCTCAAATGGGATATATTTTGTGCGCTCTAATATTGACGGAAAT
Passive Hubble1 3	TCCAGACGACGACATTTATTCATTTGTCAATCTCGCATTAATCGTAATTTTT
Passive Hubble1 4	TTTTTAACTAGCAAGGTCATTTGAACGGTAATTTTTGGGAACAAA
Passive Hubble1 5	TTTTTGTGCCGAAACCAGGCTCCGGCACTCTCCGTG
Passive Hubble1 6	GGCAGCACGCAACTGTTGGGAAGTAAAACGCGCTTCTGTTTTT
Passive Hubble1 7	TTTTTCAAACAAGAGAATCGAGCCTGAGAATCTACAATAGGGCTTAATTCTG
Passive Hubble1 8	TTAAATCAGCTCATGTTGAGAGGTCTGGAGTTTTT
Passive Hole1 1	TTTTTGTGTAGATGGGACGGCTGGCGCTTTCGAGCAGTTGTAAGAGCA
Passive Hole1 2	GAAAAGCCTAAATGTAAACGTTAAGGTCACGTTGTTTTT
Passive Hole1 3	TTTTTTGTATAAGCCTTACACTTCTTTGCTCGTCATGTAATGG
Passive Hole1 4	AAACATCCAAATATTCAAAAACAGGAAGATTTTTT
Passive Hole1 5	AATCAAGTTTTTTTTTGGGAACGTCACACTATTAAGAACGTTTTT
Passive Hole1 6	TTTTTTGGACTCCTCGAGGTGAAGCGAAAGGATTTTGGGCGCTAGGGCGC
Passive Hole1 7	AATACCGTTTCCGGGTGCTGCACTGCGCGCTGTGTTTTT
Passive Hole1 8	TTTTTCACTCTGTTGTGATAAGATGCCGGGTTTTTCTGCAGCCA
Passive Hubble2 1	GAAAAATCGACGCAACTATCATAACCCTCGAAGATTCATCAGTTTTTT
Passive Hubble2 2	TTTTTTGAGATTTAGGAAATAAAACGAACTAACGGAATTTTT
Passive Hubble2 3	GATAAGATTTACCATACGTTATACCACATAGAGTAATCTTGACAAGAACCTTTTT
Passive Hubble2 4	TTTTTTGGATATTCATTACGACAGATGCCATCGATTTTGGGGTGTAAATAC
Passive Hubble2 5	TTTTTATTACGAGGCATAGTACATAACGCGTCAGGACCTTGCCCT
Passive Hubble2 6	ATAATGCTGTAGCTCGGATTAGGAGAGGCACCATAACAAAAGGATTTTT
Passive Hubble2 7	TTTTTCTGCTCATTCACTAATGCAGATAAGAGCAACTAAAAACCCTAATAGT
Passive Hubble2 8	ATGCGATGCTTGAGCTGACCTGAAAAGAGCCAAATCAACGTAACAAAGTTTTT
Passive Hole2 1	TTTTTCAACATTATACATACAGGAAGCCTCATTGCGGATTTGCTGCTCT
Passive Hole2 3	TTTTTGACCAGCGCATAGGCTGGATGGTTTAAATCGCTCAC
Passive Hole2 4	CCATAGCAAGGCCGGAACGTCACCAATGAAAAACGGTGTACATTTTT
Passive Hole2 5	TGCCAAGCTTTCTTAGAGATTAAGTTAAGGGGATGTGCTGTTTTT
Passive Hole2 6	TTTTTCAAGGCGGTGGAGCCCCGTGGTGAAGGATAGTTCTCTCACGG
Passive Hole2 7	ACTGGCATGATTAAGAACGGATAACCCTCCACCATCAATATGTTTTT
Passive Hole2 8	TTTTTATATTC AACCGTTCTAGCTGACAACATGT
Passive Hubble3 1	CGCCAGGGGGCAAAATGTTTTGATGGTGGTTCTCACCGCCTGGCCTTTTT
Passive Hubble3 2	TTTTTCTGAGAGAGTTGCTCTTTTACCAGTGAGACGTTTTT
Passive Hubble3 3	CGAAATCTGTTTTAGCAAGCGTTGAGGATCCCCGGTACCGTTTTT
Passive Hubble3 4	TTTTTAGCTCGAATTCGTTTTGTTATCGGCCAACATTTTCAAATGACGCTCACAATCCA
Passive Hubble3 5	TTTTTCAGGCGAAAATCCCCCTTATAGTAATAACCGTACTATGGTTGCTT
Passive Hubble3 6	GTTTCCTGAAAGTGTATCCTCACAGTCCACGCTGTTTTGCCCCAGTTTTT
Passive Hubble3 7	TTTTTGCGTCCGTGAGCCAAGCCTGGGTATTGGGAACGCGGGGAGAGG
Passive Hubble3 8	GAAGCATTGTGAAAAATCATGGTCATAGCTGTGCCTGTTCTTTTTT
Passive Hole3 1	TTTTTTGGCAACAGCTGTCAAACCTATACCGCCAGCTTAATGCAAGAAAA
Passive Hole3 3	TTTTTCCACACAACATACGAGCCGGCCCGCTTTATATTTAATGCTGAATCGCAAG
Passive Hole3 4	GAAATGGGACCAGTAATAAAAGGGACATTCTCGCTCACAATTTTTTT
Passive Hole3 5	ATTCCATAGATTTAGTTTGACCATTAGATACAGTCCAATACTGTTTTT
Passive Hole3 6	TTTTTTCGGAATCGTCATAAATATTACTATTATAGACCGGA
Passive Hole3 7	AAACGAAAGAGGCCAAAAGATCATCGCCTGATATTTTT
Passive Hole3 8	TTTTTAATTGTGTCGAGCCCCCTTTCACCGGAACCAGTTTGCCACCACCGG

TABLE VI: Staple sequences for V-triangle.

Name	Sequence
Core 1 Side1 1	TATAATCAACTATGGGTAAAGGTATGTCAA
Core 1 Side1 2	AGCCTTTATTTCAACAAAAGGGTGAGAATC
Core 1 Side1 3	CTGATAGCCCTGAGAAGTGTTTTTCCCTTG
Core 1 Side1 4	CCGATTGGCGTTTTTCATCGATTTCTGCTCA
Core 1 Side1 5	AGTCACGACGTTGTAACCAGGCAGTGTAGGT
Core 1 Side1 6	ACCACTCCAGAGCCAGACGATTGGCCTTGA
Core 1 Side1 7	ACACTGGTGTGTTTTCCACCATCATCACCGAC
Core 1 Side1 8	AGGAAGATATTTTTGTTAAAATTTCGCATTAA

Name	Sequence
Core 1 Side1 9	AGCATCAGCGGGGTCATTGCAGGGTGCCGGGAAATTA
Core 1 Side1 10	GAACCAGAATCACCTAATCAGTAGCGACAGAATCAAGT
Core 1 Side1 11	CTCCGGCTCATATGTACCCCGGAAACTAGCTTCTTTGC
Core 1 Side1 12	ATATGATATTCAACCGACGACAGTAACGGCAGCGGGAGA
Core 1 Side1 13	TGATGAAGGGTAAAGTTAAACGACTTATTAGAGGGAGGG
Core 1 Side1 14	TTAGACGGAATTTGCCACTCAAACCTACCCGACGCCATT
Core 1 Side1 15	TGGTAGAATATCACCGCAGAGCACTCTCGTCGCTGGCAGC
Core 1 Side1 16	CCGGCACCGCTTCTGGTGCCGGAAAAACGACGTCACCGCC
Core 1 Side1 17	TAAATTGTAAACGTTATGTATAAGCAAATATTGCGGTATG
Core 1 Side1 18	TGATAAATATGAACGGTAATCGTATTGATAATCAGAAAAG
Core 1 Side1 19	TCGTCTTCGCGTCCGTTGCCCTAATGAGGGTCACTGTTGCC
Core 1 Side1 20	ATCTTTTCCCGGAACCTGCTGATTAACGTCAGCGTGGTGC
Core 1 Side1 21	GTAAGAATACGTGGCACAGACAATATTAGAGGGTAAGCGCA
Core 1 Side1 22	ACAAAGTCTTTGAATGACCGAGTAAAAGAGTTAGAAGAAGTTACA
Core 1 Side1 23	AACGTCACCTCATTAATTTGGGAATTAGAGCCACGAGCGAAAC
Core 1 Side1 24	TATTA AAAATATCCATCTTCAGCAAATCGTTAAGGCCGAGACAG
Core 1 Side1 25	GAGAATTAGTGAGGCCGCTATTAGTCTTTAATGCGCGAACTGCGGC
Core 1 Side1 26	TTGAGCCAAGGTGAATCACCCCTGACACTCAATCCGCCGGGCGCGGTT
Core 1 Side1 27	TTATCCTGAAATAAACAGAGCCGCCAGCCGCCACCCTCAGAACCGCCA
Core 1 Side1 28	GAGGGGACGTTCTAGCTTCATAAACATCCCTTCCCGAACGACAACCTCG
Core 1 Side1 29	AAAGATTCGCAAGGATAACGAGCGGAACAATATATCGGCCTTGTCTGT
Core 1 Side1 30	AATCTTATGACAGGGAGTAATAAGCGCCATTTCGCCATTCAAGCTGGCCTCTT
Core 1 Side1 31	AAACAGGGAATTGAGCTATTGACGACTTGTAGGCCGTTCCGGCAAACGCGGTCCG
Core 1 Side1 32	GCCAGCATCCAACGCTAAAAATTTTTAGAACCCTCATATATTTTTCCCCTACAATT
Core 1 Side2 1	TGAGCAAAAAGAAGATTACATTTGGCTCCA
Core 1 Side2 2	GGCCAACGACGCTGAGGTCTGAGAGACTA
Core 1 Side2 3	AATTA AACGTATAAACAGTTAATGCCCCCT
Core 1 Side2 4	GAGCCAGCAGCAAATGAAAAATCAATATAC
Core 1 Side2 5	AGACAAAAGAACGCGACAGAACGCGCCTGAT
Core 1 Side2 6	GGTGAATTCATATGGTTTACCATTAGCAAA
Core 1 Side2 7	AAGTACCAGAAGCGCGGCAGCACCGTCGGT
Core 1 Side2 8	GAAAACATAGCGAGCAAGAAACAATGACCAT
Core 1 Side2 9	ATATTTTAGTTAATTCGACGACAGAGAATAT
Core 1 Side2 10	AGATAGCTTAGATTAAGAGATAGTCACCAGT
Core 1 Side2 11	ATTTACGAAATACATACATAAAGGACAATCAA
Core 1 Side2 12	GAATCGCCATATTTAAAGTAGGGCTAAAGAAA
Core 1 Side2 13	AATTTCTAAATTTATCAAATGCTGAACCTCAA
Core 1 Side2 14	CTTTTTAGAAAAGTACTATCTTACCGAAGCC
Core 1 Side2 15	GATCATTTTCGAGCCATTAGTATCTTTCAAAT
Core 1 Side2 16	TATAGAAGGCCAGAATGGAAAGCGCCATCCTA
Core 1 Side2 17	TTAAGCCAATGAAACGTAGAAGCATGTAGAAACTAA
Core 1 Side2 18	CCTTTTTAGCAATACTAACCCCTTCTGACCTGAAAGC
Core 1 Side2 19	CACACGATTTACATTTGGCAGATACCTACATTTTGACG
Core 1 Side2 20	ATTTTCAGGTTTAAACCCAGTATAAAGCCAAAGCCTGT
Core 1 Side2 21	CCACGGAATAAGTTTATTTTGTCTGGCAACATATAAAA
Core 1 Side2 22	GATAGCAAGGATTAGCGGGGTTACAGTGCAGTAATTC
Core 1 Side2 23	CTCAATCGTATTATAACTATATGGATTTATCAACAATA
Core 1 Side2 24	AAGAAAATAATATCCAGTCTCTTAAATGCTCAATCGCA
Core 1 Side2 25	GAAAACCTTATATGCGTTCTATCAACAGTTGAAAGGAATT
Core 1 Side2 26	GATGAAACGTCAGATGTAAAGCATCACCTAGGGACATTCT
Core 1 Side2 27	GGTTAACATCCTGAACGAAACGCAAAGATTGTATCGGTTT
Core 1 Side2 28	TCGTCACCGTAGCAACAGTTTGTACGTTGAACTTTTTTC
Core 1 Side2 29	TACCAGGCCAGCCACCACCCTCAGGCTACAGAGCGCTTTT
Core 1 Side2 30	CAATAATATAGAAAATAGCAATAGAGCAGATAGCCGAACA
Core 1 Side2 31	GTAATAAATAAACATAACGGGGTTCAGTGCCTTGAGTATTGCTCAG
Core 1 Side2 32	TCCCTTAGAATCCTTGCTATTAATTAATTTGCTTCTGTAAATCGTC
Core 1 Side2 33	TCTGTATTTTAAATGAAAACAGTACATTTGAATTACCTTTGGGATTT
Core 1 Side2 34	GATGCAATCAAGATTACGATTTTTTGTAAACCTCCGGCTTAGGTTG
Core 1 Side2 35	TTGCGTAGAGTAACAGAAAAAAAAAACAATTTCATAAATCAATATAT
Core 1 Side2 36	CAACGCCATGCTTGAGGACTAAAGAAATCTCCTACCTTTTCAATTACC
Core 1 Side2 37	GGTCAGTTGGCAAGAAATGGATTACCAGTAATAAATCATAGAAGAGT
Core 1 Side2 38	GTGAGTGAGCGCCGACAAAGGAGCCTTTAACACAATAGTGAAACATCA
Core 1 Side2 39	AAATCAGACGTCATACATGGCTTTTTTACCCTCCAGTAAGTTAAAATC

Name	Sequence
Core1 Side12 1	AAACAGCGGTCTCCGTTTTTTTGGTGAAGGGATAGCT
Core1 Side12 2	TAAGATTTTTACGCGAGGCGTTGTTGGGA
Core1 Side12 3	GCAACAGGAAAAATTTTTTCGCTCATGAAAAT
Core1 Side12 4	TCTCCGTTGAGCGAGTAAACAACCCACTCCAG
Core1 Side12 5	ATAGCAGTTTTTCCTTTACAGAGAGAATAACATAA
Core1 Side12 6	TTTGCCGCCAGTTTTTCAGTTGGGCGGGAGACGCAG
Core1 Side12 7	CCCACGCAACCATTTTTGCTTACGGCTGGAGGTGTCC
Core1 Side12 8	TCTTTGATTAGTAATATTTTTTACATCACTTGCCAG
Core1 Side12 9	TGGTCTGGTCAGCAGCAACCGCAATTTTTGAATGCCAA
Core1 Side12 10	AAGCCGTTTTTATTTTTCATTTTTTTCGTAGGAATCATTACC
Core1 Side12 11	CTGTCCATCACGCAAATTTTTTAAACCGTTGTAACGTCAAA
Core1 Side12 12	CGGGTATTAACCAAGTACTTTTTTCGCACTCATCGAGAACAAGC
Core1 Side12 13	AAGGTAAGCTAATATCAGAGAGATAACCCACATTTTTAGAAATTGAG
Core1 Side12 14	CCAGCTTTGGCCTCAGGAAGATCGATACTTTTCAGATGCACAATTCCG
Core1 Side12 15	TATTCATTTTTTAAACAAATAAATCCTCATTAAGCTTATCTAGCAAGC
Core1 Side12 16	ACATAAAAAAATCCCGTAAAAATTTTTAAGCCGCACAGGCGGCCCTTAG
Core1 Side12 17	GTTGCTATTTTTTTTTGCACCCAGGACTTGCCTTTTTGGAGGTTTTGAAGCC
Core1 Side12 18	GCAGGTCACCACCCTCAGCCATATATTTATCCCAATTTTTTCCAAATAAGAAA
Core 2 Side3 1	GCAAAAACGAAAGAGGGCGAGAGAAAAGATT
Core 2 Side3 2	CGTTTACACATTCATTCCCAATTCTGCGA
Core 2 Side3 3	CGTACAATACCAAGTTACAAAATGACAGGT
Core 2 Side3 4	AACGTCAAATCATTGTGAATTAGCTCATT
Core 2 Side3 5	AATCAGAGCCTAACGTGCTTTCTTCATTG
Core 2 Side3 6	AAAGGAGCGGGCGCTAACCCCTAAAGGGAGC
Core 2 Side3 7	AACAAAGTACAACGGAGATTCTATGCATCAG
Core 2 Side3 8	ACACTCATCTTTGACCCCCAGCGACAGGTAG
Core 2 Side3 9	ACCTGCTCCATGTTACTTAGAAGGGGAAGAA
Core 2 Side3 10	AGGCACCAACCTCTCAGTTTTGCAATCCCCC
Core 2 Side3 11	GGTGCCGTAAAGCACTGGACTCCGTTTTTCT
Core 2 Side3 12	ACATACGATGTAGCGGTACGCTGCGCGTAA
Core 2 Side3 13	TCCAATAAATCATACAGGCAAGGAAGGCTTG
Core 2 Side3 14	CAGAGGGGGTAATAGCCAAAATAGCAAAAAGA
Core 2 Side3 15	ATACAGATAAATAAGGGTAAAATATTAGACTG
Core 2 Side3 16	CCCCGATTATCCTGTTGCTGATTGCCCTTAAT
Core 2 Side3 17	GGTCAGGATTAGAGAGCGAAAGACAGTTTCAG
Core 2 Side3 18	ACCGACCGGGAATACCCAGACGACGATAAAAA
Core 2 Side3 19	CTTGAGATGGTTTAATTTCAACTTTAAGGGCGA
Core 2 Side3 20	ACGAACCACCAGCAGTCACAATCGTAATCTGAGAGA
Core 2 Side3 21	CTCGAATTTCCACACAGTGAGACGGGCAACACAAGAGT
Core 2 Side3 22	TTGCTTTGAACACCGCTCTGAATATCGTTAGGGAATTA
Core 2 Side3 23	CGGGAGCTACAGAGGTGAGGCGGTACGTATTACGAGCA
Core 2 Side3 24	GAACGTGCAGTTCAGAAAACGACATAAATAATGGAAGG
Core 2 Side3 25	ACCGTCCAATACTGCGGAATCGTGAATGACCTTGTATGG
Core 2 Side3 26	CGTATGTGTGAAATTGCCCGCCGCGCTTAATGCGCCGCT
Core 2 Side3 27	CACTACGATCATCATACTAACAATAATAGATTAGAGCC
Core 2 Side3 28	ATTATACCGCGCTGTGTCAATAGAACCACCAGAAGGAGC
Core 2 Side3 29	GCTTTTTGCAAGAACATAACGAGATGTGGTGCAGCTGTTT
Core 2 Side3 30	ACGAGTAGATTTAGTTCATCAGTTGAGATTTATGTCTAAA
Core 2 Side3 31	TTAGCAAATTTGGGGCGAGAGCATAAAGTGTATCATCGCCT
Core 2 Side3 32	AAGCAAAGCGGATTGCTGACTATTATAGTCAGACAGGGCG
Core 2 Side3 33	AAGATAAAAAACAGGAGGCCGATTTTTGCGGGAATGCGGCGCAGT
Core 2 Side3 34	GATAAATAACCTGTTTAGCTATATTTTCATATTCCGGATAGGCTGG
Core 2 Side3 35	CTACCATATGATTGCTATAAATCAAAAATATAGAAAAGGAAATATGCA
Core 2 Side3 36	TCACACCGCTGGCCATGGTCAATTGCGGCCAAACAAAGAAATAATACA
Core 2 Side3 37	ACGATCCAGCGGGCCGAAATCTACGTTTAAGAACTGGCTCTTTACCA
Core 2 Side3 38	GCTTTAAAGCGAGAAAAGGAAGGGAAGAAAGCGCCACCACATTATCCGC
Core 2 Side3 39	TAAAATGTCGTAATGCGTTAGAACATTATACTCTGCAACAGTGCCACGCT
Core 2 Side23 1	TTAATTGAGGAAGTTTTTTTTCCATTAACGG
Core 2 Side23 2	TCAAAATTTTTGTTTTTTACGTAAAACAGAAA
Core 2 Side23 3	ACATCGGGAGAACTTTTTTATAACGGATTCCGC
Core 2 Side23 4	ATAATAAATGCTGTAGCTTTTTTCAACCAAACACTAC
Core 2 Side23 5	GAGGAAGTTATCTAATTTTTTTTTATCTTTAGGAGCA
Core 2 Side23 6	CGGAGTGACGCGCAGAGTTTTTTTCGAATTATTCATTT

Name	Sequence
Core 2 Side23 7	ATATCAAACCCTCAATATAATCCTTTTTTTTATTGTTTGG
Core 2 Side23 8	GCCTATTTTTTTTTTTGAACCTATTATTCTGAATATAATTCCAAC
Core 2 Side23 9	AGGAATTTTTTTTGCATAATATGCTAAACAACCTTTTTTTTCAAC
Core 2 Side23 10	TGTCCAGATCATCTTCTGACCTAAATTTAATTTTTTTGGTTTTGAAAT
Core 2 Side23 11	TTCCTGATTATCAGATTTTTTTTTTTGGCAATTCATCAATCAATATCT
Core 2 Side23 12	GATAGTAAAGTATTTTGCAGGATGGCTTTTTTTAGAGCTTAATTTGCTGGA
Core 2 Side23 13	TTCAAATATCGCGTTTTTAATTTTTTTTCGAGCTTCAAAGCGTAAATGAATTT
Core 2 Side23 14	ATGAAAGTATTAAGATTTTTTTTCTGAGACTCCTCAAGAGAAGGATTAGCCCAAT
Core 2 Side23 15	CGTTAAATAAGTTTTTTTATAAACACCGGAATCATAATTACTAGAAAACGCTCAAC
Core 2 Side23 16	ATTTTTTTCGTCTTTCCAGACGTTAGAACCAGACCGGAAGTTTTTTTTAACTCCAACA
Core 2 Side23 17	AAAGTACCGACAAAAGGTTCGAGGCATAGTAAGAGTTTTTTTAACTATCATAACCCT
Core 2 Side31 1	GAGCCTCCTCACATTTTTTTTTGAGGATCCCCGG
Core 2 Side31 2	CCTAAAACATCGCCATTTTTTTTTTAAAATACCGA
Core 2 Side31 3	TTTGAGGATTTAGAAGTATTATTTTTTTCTTTTACAA
Core 2 Side31 4	CGGTTACCTGCAGCCAGCGGTTTTTTTGCCGGTGCCCC
Core 2 Side31 5	GTCATACCGGGGTTTTTTTTTCTGCCAGCACGCGTGCCTG
Core 2 Side31 6	GCCCGAAGGCCGAAGCATAAAGTTTTTTGTAAAGCCTGGGG
Core 2 Side31 7	AGCCGTGAGCTAACTCACATTAATGCGTTTTTTTTGCGCTCACT
Core 2 Side31 8	TTATTAATTTTTAAAAGTTTTTTTTTGAGTAACATTATCATTAAAGGGA
Core 2 Side31 9	ATTATACCAGCTATCAGGTCATGCTTAGAACGCCATCAGTAAATTG
Core 2 Side31 10	TTTTACGGTACCGAGTTTTTAGACATTTTTTTAACGGTAGCCAGAAT
Core 2 Side31 11	CGAGCTGAAAAGGTGGCATCAATTTCTACTTTTTTTATAGTACTCCAGCTTT
Core 2 Side31 12	AGGACGTTCAATAAAGCCGGTTCACGTTGGTGTGATTTCCTGTAGAGCATTAA
Core 2 Side31 13	CCCCAAACGCGCGGGGAGAGGCGGTTTTTTTTTGGCTATTGGGCGCCAGGGTG
Core 2 Side31 14	CAGTCGGGAAACCTGTCGTGCTTTTTTAGCTGCATTAATGAATCGGCCAAAAC
Core 2 Side31 15	AATCGGTTGTATTTTTTCAAAAACATTTATGACCCTGTACGTCGGATGCCAGTTT
Core 2 Side31 16	CATCAACATTAATGGGGAAACAAACGGCGGATTGTTTTTTCCGTAATGGGATATC
Core 2 Side31 17	GGAGAGGGTAGCTATTTTTTTTTTTAGAGATCTACAAAAGGTCAAGTGAATCAAAGAA
Core 2 Side31 18	ATTTTTGTAAATCAACGTGAACGTTTTTTTTTACCCAAATCAAGTTTTTTGGGGTCCG
Active Hubble1 1	ACTGTAGCCCTTTGCCTTGCCCTTTATAGCCCC
Active Hubble1 2	GGGGATGTGCTGCAAGCGCCAGCTTCGGTGCAGCGCAACT
Active Hubble1 3	ACGCCAGGCGCTATTAGCGATTAACCATGTTTGCCCTCCCT
Active Hubble1 4	CAGAGCAAAGCCACCAATAATCAAAATCACCGCAATGAAACCATC
Active Hubble1 5	TGTGAGAGATAGACTTATCAAACCTTAAGCATTTCGGTGCAGCGTCAG
Active Hubble1 6	GATAGCAGCACCGAGTAGCACAAACATCGACCACCACAGAGAATCAGAGCCT
Active Hubble1 7	TAACGGAATATTTTTCCCAAAAAGAACTGGCCTCGGAATTAGGGCGAGGCGAAAG
Active Hubble1 8	TTAGCGAACCTAAATGCAATGCCTAGGTTGAGGTTTTCCCGTACAGCGGTTGGGTA
Active Hole1 1	CTGGCTGGGCGCATCGTAACCGTGCATCT
Active Hole1 2	GAGCCGCCACGGGAACCAAGCTTTCAGAGGTG
Active Hole1 3	GCCAGTGCGGATAACCTCACCGGACATTACCATTA
Active Hole1 4	AATAGGAGTCTGGAGCAAACAAGAGAATCGTAATGCC
Active Hole1 5	GCAAGGCCGGATTTTTTCGATCCTCATAACGGAACCGCTTTCG
Active Hole1 6	CCCTGACGAGAAACACTTTTTTTGAACGAGTAAAAATAATTGCGGT
Active Hole1 7	AAAACCGTCTATCAGGGCTTTTTTTTTGGCCACTGCTCATTTTTTTAACC
Active Hubble2 1	CCCTCAGACGTTATTCGGTTCGCTGAGG
Active Hubble2 2	ATCGCCCACGCATAAATTTCTTAAACAGCTTTGA
Active Hubble2 3	GAACGAGGCTCAGCAGCGAAAGACAATGACAACAACC
Active Hubble2 4	GGCCGCTTTTGGCGGACTTGCAGGCGATCTAATTTTTCAGG
Active Hubble2 5	AGCATCGCGAGGTGAACCGATAACTCAGGAGGTTTAGTACCGC
Active Hubble2 6	CACCCTCAGAACCTGCCGTCGATAAGTTTACATGTTTCAGCTAATG
Active Hubble2 7	ATCAGCTACATGTAGGTGTATGGATAAGGCCACCCTCAGAACCGCCA
Active Hubble2 8	AACGCCTGTTTTTTTTTTCATTCACAGACAGCCCTCATAGTTAGCGTAAGAGTTAAA
Active Hole2 1	CATAACGCAACAATCAATAATCGGCTGT
Active Hole2 2	TGATGATACAGGAGTGTACTGGTAAGAGGGTTGAT
Active Hole2 3	TACCGATAGTTATAACCTTAGAAAACAAAATTAAT
Active Hole2 4	ATAAGTATAGCCCGGAATAATTTAGGCAGAGGAAG
Active Hole2 5	CTTTTCTTATCATTCCAAGAAGCGCCCAACGGTATTC
Active Hole2 6	CGAGGCAGCAGTATGGCGCAAAGACAAATTTTAGGGCGACATTCAA
Active Hole2 7	CCATGATTAAGACTCCTTATTTTTTTTACCGGAAAATTGTGTACATGAAAC
Active Hubble3 1	GAAATCGGCAAAAAGTCCACGCTGGTTTTGCCCC
Active Hubble3 2	GCAAGCGTCCCTTATACTGACCAACTTTGAAAGAGG
Active Hubble3 3	GGTCAATCATAAGACAAAGCTCCTTATGCGATTGCA
Active Hubble3 4	CCACTATTTTTGTTCCAGTTTGGAAATGATGGTGGTTCC

Name	Sequence
Active Hubble3 5	TCAACGTAGGAACCGAAAATCAAAAGAATAGCCCCGAG
Active Hubble3 6	ATAGGGTTGAGTCAAAGAACGTAATCGGAGGGCGCTGGCCTTTC
Active Hubble3 7	ACAGATGAACGGTTCATCAAGTGGTCAATTGTGTGCAACATTATT
Active Hubble3 8	GTTAATAACCCAAACTGACCTGTACAGACCAGGCGCAACGAGGCGCAGAC
Active Hole3 1	TGCTCCTTTTGATAAGTAATGTTTTAACAATAA
Active Hole3 2	TGACCATTAGATACATTTTCGAAAAGTAATCTTGA
Active Hole3 3	AGCAGGCGAAATAGAGCTTGACGGGAAAGCCGGC
Active Hole3 4	CTTTACCCATCAAAAAGATTAAGAGGAAGCCTACCTTTAAT
Active Hole3 5	TGGAAGTTTTCACAGTTGAACTAATGCAGATACATTTTTTTTACGCCAAAAGG
Active Hole3 6	CAAGAACCGGATATTCATTAACGAACAATCCGCGGTCACTGCAAGCGCGA
Active Hole3 7	AGGAACCCATGTACCGTTTTTTTTTACTGAGTTTCGTCAACCAGAGGTCATCGGTGTC
Passive Hubble1 1	TTTTTACTGTAGCCGTTTGCCTTGCCTTTATAGCCCC
Passive Hubble1 2	TTTTTGGGGATGTGCTGCAAGCGCCAGCTTCGGTGCAGGCGCAACT
Passive Hubble1 3	TTTTTACGCCAGGCGCTATTAGCGATTAACCATGTTTGCCTCCCT
Passive Hubble1 4	CAGAGCAAAGCCACCAATAATCAAAATCACCGCAATGAAACCATCTTTTT
Passive Hubble1 5	TGTGAGAGATAGACTTATCAAACCTAAGCATTTTTCGGTGAGCGTCAGTTTTT
Passive Hubble1 6	TTTTTGATAGCAGCACCGAGTAGCACAACAATCGACCACCACCAGAGAATCAGAGCCT
Passive Hubble1 7	TAACGGAATATTTTTCCCAAAAGAAGTGGCCTCGGAATTAGGGCGAGGCGAAAAGTTTTT
Passive Hubble1 8	TTAGCGAACCTAAATGCAATGCCTAGGTTGAGGTTTTCCCGTACAGCGGTTGGGTATTTTT
Passive Hole1 1	TTTTTCTGGCCTGGGCGCATCGTAACCGTGCATCT
Passive Hole1 2	TTTTTGAGCCGCCACGGGAACCAAGCTTTCAGAGGTGTTTTT
Passive Hole1 3	GCCAGTGCAGATAACCTCACCGGACATTACCATTATTTTT
Passive Hole1 4	TTTTTAATAGGAGTCTGGAGCAAACAAGAGAATCGTAATGCC
Passive Hole1 5	TTTTTGCAAGGCCGATTTTTTCGATCCTCATAACGGAACCGCTTTCG
Passive Hole1 6	CCCTGACGAGAAACACTTTTTTTGAACGAGTAAAAATAATTCGCGTTTTTT
Passive Hole1 7	AAAACCGTCTATCAGGGCTTTTTTTTGGCCACTGCTCATTTTTTAACCTTTTT
Passive Hubble2 1	TTTTTCCCTCAGACGTTATTCGGTGCCTGAGG
Passive Hubble2 2	TTTTTATCGCCCACGCATAATTTCTTAAACAGCTTGATTTTTT
Passive Hubble2 3	GAACGAGGCTCAGCAGCGAAAGACAATGACAACAACCTTTTT
Passive Hubble2 4	TTTTTGGCCGCTTTTGCAGGACTTGCAGGCGATCAATTTTCAGG
Passive Hubble2 5	AGCATCGCGAGGTGAAACCGATAACTCAGGAGGTTTAGTACCGCTTTTTT
Passive Hubble2 6	TTTTTACCCTCAGAACCTGCCGTCGATAAGTTTACATGTTTACGCTAATG
Passive Hubble2 7	ATCAGCTACATGTAGGTGTATGGATAAGGCCACCCTCAGAACCGCCATTTTT
Passive Hubble2 8	AACGCCTGTTTTTTTTTATTCCACAGACAGCCCTCATAGTTAGCGTAAGAGTTAAATTTTT
Passive Hole2 1	CTAAACGCAACAATCAATAATCGGCTGTTTTTT
Passive Hole2 2	TGATGATACAGGAGTGTACTGGTAAGAGGGTTGATTTTTT
Passive Hole2 3	TTTTTTACCGATAGTTATAACCTTAGAAAACAAAATTAAT
Passive Hole2 4	TTTTTATAAGTATAGCCCGGAATAATTTAGGCAGAGGAAG
Passive Hole2 5	TTTTTCTTTCCTTATCATTTCCAAGAAGCGCCCAACGGTATTC
Passive Hole2 6	TTTTTTCGAGGCAGCAGTATGGCGCCAAAGACAAATTTTTAGGGCGACATTCAA
Passive Hole2 7	CCATGATTAAGACTCCTTATTTTTTTACCGGAAAATTTGTGTACATGAAACTTTTT
Passive Hubble3 1	TTTTTGAAATCGGCAAAGTCCACGCTGGTTTGCCCTTTTT
Passive Hubble3 2	GCAAGCGTCCCTTATACTGACCAACTTTGAAAGAGGTTTTT
Passive Hubble3 3	TTTTTGGTCAATCATAAGACAAAGCTCCTTATGCGATTTGCA
Passive Hubble3 4	CCACTATTTTGTCCAGTTTGGAAATGATGGTGGTTCCTTTTT
Passive Hubble3 5	TCAACGTAGGAACCGAAAATCAAAAGAATAGCCCGATTTTT
Passive Hubble3 6	TTTTTATAGGGTTGAGTCAAAGAACGTAATCGGAGGGCGCTGGCCTTTC
Passive Hubble3 7	TTTTTACAGATGAACGGTTCATCAAGTGGTCAATTTGTGTGCAACATTATT
Passive Hubble3 8	GTTAATAACCCAAACTGACCTGTACAGACCAGGCGCAACGAGGCGCAGACTTTTT
Passive Hole3 1	TTTTTTGCTCCTTTTGATAAGTAATGTTTTAACAATAA
Passive Hole3 2	TGACCATTAGATACATTTTCGAAAAGTAATCTTGATTTTTT
Passive Hole3 3	TTTTTAGCAGGCGAAATAGAGCTTGACGGGAAAGCCGGC
Passive Hole3 4	CTTTACCCATCAAAAAGATTAAGAGGAAGCCTACCTTTAATTTTTT
Passive Hole3 5	TTTTTTGGAAGTTTACAGTTGAACATAATGCAGATACATTTTTTTTACGCCAAAAGG
Passive Hole3 6	TTTTTCAAGAACCGGATATTCATTAACGAACAATCCGCGGTCACTGCAAGCGCGA
Passive Hole3 7	AGGAACCCATGTACCGTTTTTTTTTACTGAGTTTCGTCAACCAGAGGTCATCGGTGCTTTTTT

TABLE VII: Staple sequences for X-triangle.

Name	Sequence
Core 1 Sidel 1	AGCCGCCGAAACAAATTCAGAACCACCCTCAGAACCGCCATACTCAGGGTCGAGAG
Core 1 Sidel 2	GTGCACTCAGGCTGGCCAAGCTTTAACACCGTCGGTGGTGATTTGCCGTTAGCTAT

Name	Sequence
Core 1 Side1 3	ATAAACAGATCGCCCAAAGCACTTAATGCGCCGCTACAGGGCGCGTTGCAGGG
Core 1 Side1 4	ATTTGTATGACCTGCTCTGAGGCTACTATGGTTGCTTAAAATCCCGTA
Core 1 Side1 5	TGAGCTAAGTGGTTTTTCTTTTCATGGTTCCGTTTGATGAGTGCCCGT
Core 1 Side1 6	CAACGGAGGGTTGATATTCGGTCGGTGCCTTGCAATACTTCTTTGATA
Core 1 Side1 7	AGTAAGTCAGACGATTATTAGGATTTTAGTTTTAACCTGTCCAGCAGT
Core 1 Side1 8	GTAGATGGGCGCATCGTAACCGTGCATCTGCGAACTGACCAGACGGT
Core 1 Side1 9	CCTACATTAGGGAACCCAGGCCATTGCAACAGGAAAAACGCTATGAG
Core 1 Side1 10	TATTTCAACCCGACAGTGGGCGGTGGAATTTGCAGCGCCATGTTTAC
Core 1 Side1 11	ATCGGCGACAGAGGTGATTACGCCGATCGGTGCGGGCCTGGCCTTGC
Core 1 Side1 12	GGAATACTGCCAGCACGCGTGCCTGTTCTTTTTTTCATAGATTATTT
Core 1 Side1 13	TGCAATGCAACATTATGACCCTGTAATACTTATTTTCATAAGAGGT
Core 1 Side1 14	ATTTACCGTTCCAAGTTAGCGTTTGCCATCCGCGTCCGGTGTAAAG
Core 1 Side1 15	AGAGCTTAAAACACCAGTAATCTTCAGCGCAGTGTCACTCTTCTGT
Core 1 Side1 16	AGTAACATACAGGACAGAATGGCACCCGGAACCCAGACCGGGGTTT
Core 1 Side1 17	AGAGAAGGGCCCTTGAAGGCGCATAACAGATGAACGGTGTCAACTTT
Core 1 Side1 18	CTTCGCTGAGCCGCGACGACAGTATCGGCCTCAGGAAGGAAGGGC
Core 1 Side1 19	TTTGACCCCCAGCGAACCCATGTACCGTAAAGAATAGCCCTGCCT
Core 1 Side1 20	CCTGGGGTGCCTACATCTGAAATGATCAAATAAAAGCGCA
Core 1 Side1 21	ACGTTGGTCGTCTGGCGCGCCTCAGATTGGGCTTGAGA
Core 1 Side1 22	GCCAGTGCTGACCTTCCGAGTAGATAGTTGCGGATGGCTT
Core 1 Side1 23	TTGCGGGATTTAGAACCCTCATATATTTTAAACCTTTTGA
Core 1 Side1 24	AAGAACTCAAACATCAGCTAAACACCTCACCATCGACAT
Core 1 Side1 25	GGTGCCGTCGCATAACAGTTAAAGAGCGCGAAACAAAGTA
Core 1 Side1 26	CGGGCCGTTTTACGGTCATAACCACCACCGGCAATCATA
Core 1 Side1 27	TTTGGGGCTCCCAATTCTGCGAAATCAAGAGAACGAGT
Core 1 Side1 28	AGGAGGCCTTAGAATCAGAGCGGGCAGTCCCTGTGTAC
Core 1 Side1 29	CCATGTTAAAATGACGAGCACGTATAACCGAGTTGTAG
Core 1 Side1 30	AAAAAAGTGTGTGCTTCCGCAAATGGTCAAGACCATTA
Core 1 Side1 31	AGGCTCATACTTGGCAGATTCAGCATAAATGAGCCT
Core 1 Side1 32	GGTGTGCTTTCTCGGATTAAGGGATTTTGTATTGC
Core 1 Side1 33	CATTTCCGGGTTTTTGCTAAAAATTGAAGCATT
Core 1 Side1 34	GCCGAAACGTCACCACAGTTTCAGCGGAGTG
Core 1 Side1 35	CAATAGGATTATACCAGCCGTTTTTGCGGGAT
Core 1 Side1 36	GTCTCTGAATTTTCGGAACCTATTAGCCAAGCC
Core 1 Side1 37	CATCAAAAATAATTCGTGCGGCCAGGTTGAGG
Core 1 Side1 38	CCAGTGAAATATTACCGCCATTTTGGTAATA
Core 1 Side1 39	GAGGGGACCACGGGAATTTAGGCGACAGACC
Core 1 Side1 40	ATTAAGCGTGACTGTTGACGCTCAATCGT
Core 1 Side1 41	GTAATAAGCGGATTAGTAATAACATCACTGG
Core 1 Side1 42	CTTAGCCGAAATCCGCCATCGCCTGATAAAT
Core 1 Side1 43	CGATAGTTGCGCCGCTCAGCAGCACTCATC
Core 1 Side1 44	GGAAACAGATACATGAACGTAACGGGGTCA
Core 1 Side1 45	CGCAAGGATCAGTACCAGGCGGACTCCTCA
Core 1 Side2 1	CGTATTAACTTTACAATATTCCTGCAAGCCGTTATAGAAGGCTTATCCACCCACAA
Core 1 Side2 2	GTGTGATATGGCTATTAGTCTTTAATGCGCGTTTACGAGAATCATAAAGAACAAG
Core 1 Side2 3	CTTTAATTGTATCGGGCTCCAATGGACTCCGAGTGGTTGCGGTCCACGCCCTGAG
Core 1 Side2 4	TGACGGAAAGGAATCAAGATGCTGATGCAAATCCAATCAACAATTCAAGAATA
Core 1 Side2 5	TTCATCGAGCAGCACCGTAATCTTTCTGTAGAATAATAAACAGCTTGATAC
Core 1 Side2 6	ACATTCAAAGGAGTGAATAACCTTGCTTTCGGTTATATAATCAGATTTTATT
Core 1 Side2 7	AGCGGTCTACAGAGCGAGGTGAGTTAGCCGTTAGTAAATGAATAGTAGCGA
Core 1 Side2 8	CGCTCACAATTCTGGCCAACAGAGAGCCATTTATAGGGTTAACGTTTT
Core 1 Side2 9	CATCCTAAAACCTGATATAAAGCATCACCTTGCTGAACACCAACACCCGG
Core 1 Side2 10	CCGATTGACAAAGACAAAATTCATATGGTTAATGAGGAAGTTTCCAT
Core 1 Side2 11	TGCAAATTTAATGGTTTGAATAACCGCTCAAATATCAAAGTATTAGA
Core 1 Side2 12	GGCCAACGCTTTCCAGTCGGGAAACCTGTCGTTAAAGGTGTAAATAT
Core 1 Side2 13	ATAAAAGAAACGCAAGACTTGCGGAGAGATAGGTATTCTTTTTTAAAC
Core 1 Side2 14	GTAAAGTCATCCTTGAGCTATTAATTAATTTTGTCTATCCGTGGCG
Core 1 Side2 15	AAACATAGCGATAGCTCATCGCAAGACAAAGTTAATTTGACAACCT
Core 1 Side2 16	ACCGTCACCGACTTGATAGAACCCTTTATCGAATCTGACCTGAAA
Core 1 Side2 17	AGGGCGATAAAGGGCGAAAAACCCAGCAAGTTCCAGTATGAATC
Core 1 Side2 18	TTGTTATCACTGCCCGCGGGGAGAGCGGTGACCCGAG
Core 1 Side2 19	AGCCATATTTGAAGCCTTAAATCAATAAAGGTGGCAACAT
Core 1 Side2 20	ACGTGGCACAGACAATATTTTTGAAAATAAGGATTATTCA

Name	Sequence
Core 1 Side2 21	GAACGCGAGAAAACCTTCCCTTAGACACTATTAAGAAAAGGA
Core 1 Side2 22	TTCATCGTCTGTTAAATCATCTTCTGACCTCAGATATTTTA
Core 1 Side2 23	AGAGTTGTTTCAAATCTGCATTATTGGAACATTAGGAAG
Core 1 Side2 24	GATTTAGAGCTTGACCTTGCTTTGCTTTGAGTAAACGGG
Core 1 Side2 25	AATAACGGTTTTTAAATGGAAACAGTACATAAAAAACAAT
Core 1 Side2 26	CAAAATCAAGTAATAAAAAGGGACATTCCACTCATGGT
Core 1 Side2 27	TCTTACCGAAGCCCTAATATCAGGAGGTTTATTTAT
Core 1 Side2 28	TCAATAGAAAAGGGCGAGAGCAAGATCAATAT
Core 1 Side2 29	CATAGCTGTTTCTGTGTGAAAGCGTAAGAAT
Core 1 Side2 30	CACAGACACACTACGACGAGGGTAGCAACGGC
Core 1 Side2 31	GACTAAAGACTTTTTTCGGGCGCTACCGGCGAA
Core 1 Side2 32	GGAGAAACGAATFGAGGAAATAGCAATAGCTA
Core 1 Side2 33	CATTAACCTGAACAAGAAAAATTATAAAGT
Core 1 Side2 34	AGAAGGAGCGGAATTATTAGATTATAGGTTGG
Core 1 Side2 35	TTAAGCCCAATAATAAGCAAGCAAACTATAT
Core 1 Side2 36	AGACCGCACTCATCGTTACTAGAATTTAGAA
Core 1 Side2 37	AAGAACGAAGGAGCGGGAGCCGCGCCAAT
Core 1 Side2 38	AAGAACGCTTAAACCAAGTAGAAAATATCC
Core 1 Side2 39	ATGTGGAAGAAAGCGAAAGGAGCCAGCGC
Core 2 Side3 1	CTTGTAGACCATATCACAATTACCTCATTGCCGAGAGATCTGCCGGAGAGGGTAGC
Core 2 Side3 2	CTAGCTGACCATAAATCAGGCAAGTAAAATGTATTGCAGGCGCTTCTAACGTCAGC
Core 2 Side3 3	CCAACGCTATTTAACAGGATTATAAAAAATTTATCAAATACAAAATCGAGAATTA
Core 2 Side3 4	TCAGCAGCAGCATCAGGAAAAAGAATCCAATAAATTAAGCTGATATTCAAACCGTT
Core 2 Side3 5	GCAATTAACGACGCAGATCCGGCAAACGCGGTCCGTTTTTTTTAGCAAAATCATA
Core 2 Side3 6	TTTCAGGTGAAATAAAGAAATTGAACATTATAATGGAGCTAAGGGCTTA
Core 2 Side3 7	ACAGTTGAAGATTAGAGCCGTCAAGATTGTTTACGCCAACAATAGCAG
Core 2 Side3 8	CGATGAACAAAGCTCGTCTTTTATTGCGGCTGGTATGAGCCGGGTCAC
Core 2 Side3 9	AACGGAATACCCAAAAGAGGAAACGCAATAATACAAACATGCCAATTA
Core 2 Side3 10	GAGGCGGTGATATTAGTACCCCGTTGATAAAGCATGTCATCATAT
Core 2 Side3 11	AAGCAAATATTTAAATTTGTAACAGGACGTTTTTACCTGCAACAAAAT
Core 2 Side3 12	CCTTTACATTAGACGGGCGCAGAGCAAGAAAAACAATTAATTACAT
Core 2 Side3 13	AAACAGGGAAGCGCAGAGAGAATTTGCACGTCTTCTGAATCATTTTG
Core 2 Side3 14	TAAATCGGAAGCCGGAGACAGTCAAATCACGCTTCAAATAGTAGTA
Core 2 Side3 15	TAAAGGTTTCATAAACATCCCTTACATGGGAACAAACGGTGGTGCCG
Core 2 Side3 16	GTGCCGGAGCGAGTTTTTGTAAAATTCGCATTAATTCGATTTTA
Core 2 Side3 17	AACGGAACGTGCCGGACGTAGATTTTCAATTTAAATTTATAACATAA
Core 2 Side3 18	AACTCGCACTCAATCCCGCTTGGCAAAGCGCATCAGGTGTGTT
Core 2 Side3 19	GTTATCTAGTAATCGGAGCAAACAAGAGAATGTTTTTGCC
Core 2 Side3 20	GTTAATATAACAACCCGTCCGATTCTCCGCTGATGCCGGG
Core 2 Side3 21	ATCCTCATGTGGTGTCTGGTCTGGAAGGGCGCGGTTGCG
Core 2 Side3 22	CCTCCGGCCAGAACGCGGGGTCTTAGACTGCTTTTTG
Core 2 Side3 23	ATAAAGCTACTAAGCGAACCTACGGTGCATCATAA
Core 2 Side3 24	GAAACCAGGGTAACGCAGCGAGAGGGATAGCG
Core 2 Side3 25	TGAGAGGGGGTAATAGCTATCAGGTGAGGCGAG
Core 2 Side3 26	TTTAAAGTTTTGAGTTGTTGCCCTTTAGGA
Core 2 Side3 27	AGGGTTAGAGAGTCTGATTGAGAATCGCCAT
Core 2 Side3 28	CAACAGTACAACATAAAGGAATTGAGGAAG
Core 2 Side3 29	CTCGTTTACCAGAACTCATTATAACAGTC
Core 2 Side3 30	TCGCTGCAAAAAGAAGATGATGAATATTTTT
Core 2 Side3 31	TCTGGAACCCACGACGATAAAAAGCCAGCG
Core2 Side12 1	TAAAATACGTAATGCGCCCTCATAATTTCTTATTTTTTCCACCGAGTTTTTTAAAAGA
Core2 Side12 2	ACATGGCTAAATCGGCATCACGCAACGGTACGCCTTTTTAGAAATCCTGAGAAGTGTC
Core2 Side12 3	CAGTACAAACTTTTTTACAACGCTGTTTTGCTAAACTTTTTAACTTTCAAATGAAAC
Core2 Side12 4	CAACAACCTTAATGCGTCTGTCCAAAATCCCTTATATTTTTTAATCAAAGAAT
Core2 Side12 5	CTGAGTAGTCCAGAACGACGGGCAACAGCTGATTGCTTTTTTCCCTTCCACCGCCTG
Core2 Side12 6	GCTGGTTTTGCCAGCTTTTTAGGCGAAAATCCTGTTAGACAGGAAATTAACC
Core2 Side12 7	TTGCGTATTTTTTTGGGCGCCAGGCTCACATTTTTTTAATTGCGTTGCGCTC
Core2 Side12 8	CCTCACAGTTGAGGATCCTTTTTCCGGGTACCGAGCTCGAAGCGGTT
Core2 Side12 9	CACTGAGTTTCGTCAACCACTAAAACGAAAGACATTTTTTGCATCGGAA
Core2 Side12 10	GGCCCACTACGTGAACCATCTTTTTACCCAAATCAAGTTTTTTTGG
Core2 Side12 11	ACGCTGCGCGTATTTTTTACCACCACACCCCGTCAACCAATGA
Core2 Side12 12	ACAACATACGAGCTTTTTTCGGAACCAAGTCATTTTTTACGACC
Core2 Side12 13	AAAGGAACAACATAAAGGAATTTTTTTGCTGGGATTAGCATTC

Name	Sequence
Core2 Side12 14	AGGCACCAACCTAAAACGAAATTTTTGAGGCAAAAAGAATA
Core2 Side12 15	GCCGCGCTAAATCGGAACCCTAAAGTTTTTGGAGCCCC
Core2 Side12 16	CATCGATGCATTTTTTTTTTCGGTCATAGCCCCCTTA
Core2 Side12 17	CCAGTAGCACTTTTTTCATTACCATTAGCAGTA
Core 2 Side23 1	GTATGTTAGCAAACGTAGTTTTTTTAATACATACAGATTAGTTTTTTTTTATTTTTGCAC
Core 2 Side23 2	CAAATAAGAAATTTTTGATTTTTCCAGCCAGCTACAATTTAATTACGCAGATAGCCG
Core 2 Side23 3	TTAACGTCAGATGAATATTTTTTTTAGTAACAGTACCTTTTACACTGTAAATCGTC
Core 2 Side23 4	TACCAGAACTGAACACCCTGAAAACGTCAACTGAGATTTTTTACTACCCCCAATC
Core 2 Side23 5	CCCTCAATCAATATTTTTTTTTGGTCAAGTTGGCAAATCAACACCGCCGTATAAAG
Core 2 Side23 6	ACCGACAAAAGGTAAATTTTTTTAATTCTGTATCAACATTTTTTTAGATAAGT
Core 2 Side23 7	TGTTTAGTATCTTTTTTATGCGTTATACAAATCTTACCATGCAACA
Core 2 Side23 8	ATTATCAGCTCCGGCTAGACGCTGTTTTTTAAGAGTCAATAGTGACA
Core 2 Side23 9	ATTCGCCTGATTGCTTTTTTTTGAATACCAAGTTCATAGGTAAATGAA
Core 2 Side23 10	TAGATAATACATTGAGGAAAAGCCAAAAATCGCCATAAACATCGC
Core 2 Side23 11	ATCCTTTGTTTTTTTCGAACGTTATTAATCGGAACAAAGAAACCA
Core 2 Side23 12	CCTGTTCCAGACGACGACCATTTTCTTTTTTAGCCAGTAATA
Core 2 Side23 13	ATACCGAATTTTTTTAACCACCAGCAGAAGATAAAAAGAACGCG
Core 2 Side23 14	AACAAAGTTTAAACAATTTTTTTTCATTTGAATTACCT
Core 2 Side23 15	AATTGAGCGCTTTTTAAGAAAATTTTTTTAAGCA
Core 2 Side23 16	AGCCTAATTTTTTTTTCCAGTTACAAAATAAAC
Core 2 Side23 17	ATGATGGCAATTCATTTTTTCAATATAATCCT
Core 2 Side31 1	CTGAGTAATGTGTAGTTTTTTTTTAAGATCAAACCAACAGGCTTTTTTTGATTAGAGA
Core 2 Side31 2	GTAATGGGGCCATTCGCCATTCAGCTGCTTTTTTTAACTGTTGGATCGCAC
Core 2 Side31 3	TGGTTTAATTTCAACTAGACGATCGACAAGAACCGTTTTTTATATTCATTA
Core 2 Side31 4	TTGTGAATTTTTTTTCTTATGTTTGTTTTTTTAATCAGCTCATTTTT
Core 2 Side31 5	TAACCAATAGGAACGCTAGCCAGCTTTCATCAACATTTTTTTAAATGTG
Core 2 Side31 6	CAGGGTTAGGTGTCCAACCGCAAGTTTTTTTTTGCCAACGGCAGCGTA
Core 2 Side31 7	TGAGAGATAGACTTTCTTTTTTTCGTGGTGAAGGGATAGCTCTCGCAC
Core 2 Side31 8	AGAACTGGTCAACGTAACAAGCTGCTCATTCTTTTTTTGAATAAG
Core 2 Side31 9	AACTAAAGAGACCGGAAGCAAACCTGGGTGAGATTGCTTTTTTTAAA
Core 2 Side31 10	ATTGCTGACAGTTGATGCGAGCTGAAATTTTTTTGGTGGCATCAATT
Core 2 Side31 11	CCATCCCACGCAATTTTTTCAGCTTACGGCTGGTCCCAGTCACGAC
Core 2 Side31 12	GCGGCCTTTTAGTGATGAAGGGTAAAGTTATTTTTTACGATGCTG
Core 2 Side31 13	TTGTA AACGACGTCCAGCCAGCTTTTTTTTTTCGGCACCGCTTC
Core 2 Side31 14	GTTTCATTCCATTTTTTTTTAAATATAATGTACCTTTAATTGCT
Core 2 Side31 15	ATFGCCGTAACAGCGGATCAAACCTTTTTTTAAATTTCTGCTC
Core 2 Side31 16	TGCCCCCTGTTTTTATCTTAATCAGCTFGCCCTGACGAG
Core 2 Side31 17	AGCTGGCGAAAGGGGTTTTTTTTGTGTGCTGCAAGCGATT
Core 2 Side31 18	GCTGTAGCTTTTTTTTACATGTTTTTAAATATGC
Core 2 Side31 19	CGGATTGACCGTTTTTTAATGGGATAGGTC
Active Hubble1 1	CTCAGAGCCGCCATGACAGGAGAATGCGGAAAGAGGTGTGGTGC
Active Hubble1 2	GGGATAGCCGGAATAGGTGTATCACCGCCCTCAGACATGAAAG
Active Hubble1 3	TATTCACCCAGCATCCAGAACCACCACCAGAACCGCCTCCCTC
Active Hubble1 4	CGATATATAAGTATATTCTGAAAGCCACCACCCTCATTTTCA
Active Hubble1 5	TCAGAACCCGCCACCCTCAGAGCCACCACC
Active Hubble1 6	AGAGCCGCCACCCAAATCCTCTATTAAGAGGCTGAGA
Active Hubble1 7	TAAGTGCCAGGTTTAGTACCGCCACCC
Active Hole2 1	TTGTGCTCAAAAAAAAAATTTATCAGGGGGAAAGGGGCGCTGGCAAGTGT
Active Hole2 2	GCGAACCTCCCAGACACCACGGAATAAGTTTATTTTGTCAAA
Active Hole2 3	TATAATCAGTGAGGCACGTTGAGAGCCAGCAGAATCAAGTT
Active Hole2 4	GGGAATTTAAATCTCCTTTCCAGAGTAACGATCTAAAGTT
Active Hole2 5	GCTGCTTTTCTTATCAACCAATCAATAATCG
Active Hole2 6	CATGTAGAATTTCCAAGAACGGGTAGAGGCGTTTTTA
Active Hole2 7	TGCTTTAGCGTCAGACTGTATTTCGTA
Active Hubble3 1	AAAAAGATTAAGATAATTTCGACATCAATAAATAAAGCCTCAGAGC
Active Hubble3 2	TACGTTAATAAAATCATAACCATATTCATTTCAATACTGCGGAAT
Active Hubble3 3	TACCACATCAACACTACGAACTAAAGAAGCAAAGCGGATTGCATC
Active Hubble3 4	TGAATCCCTCGGTTTTGGAAGCCGAAAGACTCAAAAATCAGGTC
Active Hubble3 5	GTAAGAGTCAACTAAGTTGAGATTTAGGAAGGGAAGAAAAATC
Active Hubble3 6	TCAAATACCCTCAAATTATAGTCCGGAACAACATTATTACAGGT
Active Hubble3 7	AGAAAGATTATCATGCAGATGATTGTATCAGCAAT
Active Hubble3 8	TTTACCCTGACTATGCTTTAAACAGTTTCAGAA
Active Hole3 1	TCAGCTAATGCACAGAGGTGTGCCACGCTGAGAGCAGCAGCAAATG

Name	Sequence
Active Hole3 2	AGGAAACCGAACTGGCATGATTAAGACTCCTTTTCCTGAATCTT
Active Hole3 3	AACGAGAATGATAAATTAATACAAAAGGGCAAAGAATCGTCTCG
Active Hole3 4	TAAAACCTTCAGAAAAGCCCCAAAAACAGGAAACATAACGCCA
Active Hole3 5	ACCAACGCTAACGAGCGTCTTTTGTTCAAAGTCAGAGGG
Active Hole3 6	AAAGGAATTACGAGGCATACAAAAGAACGTTAACG
Active Hole3 7	ATGTAATTTAGGCAGAGGAATAACAACATGT
Passive Hubble1 1	TTTTTCTCAGAGCCCATGACAGGAGAATGCGGGAAAAGAGGTGTGGTGC
Passive Hubble1 2	TTTTTGGGATAGCCGAATAGGTGTATCACCGCCCTCAGACATGAAAG
Passive Hubble1 3	TATTCACCCAGCATCCAGAACCACCACCAGAACCGCCTCCCTCTTTTT
Passive Hubble1 4	CGATATATAAGTATATTCTGAAAGCCACCACCCTCATTTTCATTTTT
Passive Hubble1 5	TTTTTTCAGAACCGCCGCCACCCTCAGAGCCACCACCTTTTT
Passive Hubble1 6	TTTTTAGAGCCGCCACCCAAATCCTCTATTAAGAGGCTGAGA
Passive Hubble1 7	TAAGTGCCAGGTTTAGTACCGCCACCCTTTTT
Passive Hole2 1	TTTTTTTGTCTCAAAAAAATTTATCAGGGGAAAAGGGGCGCTGGCAAGTGT
Passive Hole2 2	TTTTTGCGAACCTCCCAGACACCACGGAATAAGTTTATTTTGTACAA
Passive Hole2 3	TATAATCAGTGAGGCACGTTGAGAGCCAGCAGAATCAAGTTTTTTTT
Passive Hole2 4	GGGAATTAAAATCTCCTTTCCAGAGTAACGATCTAAAGTTTTTTTT
Passive Hole2 5	TTTTTGCTGTCTTTCTTATCAACCAATCAATAATCGTTTTT
Passive Hole2 6	CATGTAGAATTCCAAGAACGGGTAGAGGCGTTTTATTTTT
Passive Hole2 7	TTTTTTGCCTTTAGCGTCAGACTGTATTCGTAA
Passive Hubble3 1	TTTTTAAAAAGATTAAGATAATTGACATCAATAAATAAAGCCTCAGAGC
Passive Hubble3 2	TTTTTTACGTTAATAAAATCATAACCATATTCATTCCAATACTGCGGAAT
Passive Hubble3 3	TACCACATCAACACTACGAACCTAAAGAAGCAAAGCGGATTCATCTTTTT
Passive Hubble3 4	TGAATCCCTCGCGTTTGGAAAGCCCGAAAAGACTCAAAAAATCAGGTCTTTTT
Passive Hubble3 5	GTAAGAGTCAACTAAGTTGAGATTTAGGAAGGGAAGAAAATCTTTTT
Passive Hubble3 6	TCAAATACCTCAAATTATAGTCCGGAACAACATTATTACAGGTTTTTT
Passive Hubble3 7	TTTTTAGAAAGATTCATCATGCAGATGATTGTATCAGCAAAT
Passive Hubble3 8	TTTTTTTTACCCTGACTATGCTTTAAACAGTTCCAGAAATTTTT
Passive Hole3 1	TTTTTTCAGCTAATGCACAGAGGTGTGCCACGCTGAGAGCAGCAGCAAATG
Passive Hole3 2	AGGAAACCGAACTGGCATGATTAAGACTCCTTTTCCTGAATCTTTTTT
Passive Hole3 3	TTTTTAAACGAGAATGATAAATTAATACAAAAGGGCAAAGAATCGTCTCG
Passive Hole3 4	TAAAACCTTCAGAAAAGCCCCAAAAACAGGAAACATAACGCCATTTTT
Passive Hole3 5	TTTTTACCAACGCTAACGAGCGTCTTTTGTTCAAAGTCAGAGGG
Passive Hole3 6	TTTTTAAAGGAATTACGAGGCATACAAAAGAACGTTAACG
Passive Hole3 7	ATGTAATTTAGGCAGAGGAATAACAACATGTTTTTT
Strong3 Hubble1 1	TATTCACCCAGCATCCAGAACCACCACCAGAACCGCCTCCCTCGTT
Strong3 Hubble1 2	CGATATATAAGTATATTCTGAAAGCCACCACCCTCATTTTCATTG
Strong3 Hubble1 3	AGAGTCCGCATGACAGGAGAATGCGGGAAAAGAGGTGTGGTGC
Strong3 Hubble1 4	ATAGCCGGAATAGGTGTATCACCGCCCTCAGACATGAAAG
Strong3 Hubble1 5	GCCGCCACCCAAATCCTCTATTAAGAGGCTGAGA
Strong3 Hubble1 6	GAACCGCCGCCACCCTCAGAGCCACCACCTTA
Strong3 Hubble1 7	TAAGTGCCAGGTTTAGTACCGCCACCCGAG
Strong3 Hole2 1	TCTGCAAAAAAATTTATCAGGGGAAAAGGGGCGCTGGCAAGTGT
Strong3 Hole2 2	TATAATCAGTGAGGCACGTTGAGAGCCAGCAGAATCAAGTTATT
Strong3 Hole2 3	GGGAATTAAAATCTCCTTTCCAGAGTAACGATCTAAAGTTAAA
Strong3 Hole2 4	AACCTCCAGACACCACGGAATAAGTTTATTTTGTACAA
Strong3 Hole2 5	CATGTAGAATTCCAAGAACGGGTAGAGGCGTTTTTACAG
Strong3 Hole2 6	GTCTTTCTTATCAACCAATCAATAATCGCGC
Strong3 Hole2 7	CTTTAGCGTCAGACTGTATTCGTAA
Strong3 Hubble3 1	TGAATCCCTCGCGTTTGGAAAGCCCGAAAAGACTCAAAAAATCAGGTCAAC
Strong3 Hubble3 2	TACCACATCAACACTACGAACCTAAAGAAGCAAAGCGGATTGCATCACC
Strong3 Hubble3 3	TCAAATACCTCAAATTATAGTCCGGAACAACATTATTACAGGTAAA
Strong3 Hubble3 4	GTAAGAGTCAACTAAGTTGAGATTTAGGAAGGGAAGAAAATCTCA
Strong3 Hubble3 5	GTTAATAAAAATCATAACCATATTCATTCCAATACTGCGGAAT
Strong3 Hubble3 6	AAGATTAAGATAATTGACATCAATAAATAAAGCCTCAGAGC
Strong3 Hubble3 7	AAGATTCATCATGCAGATGATTGTATCAGCAAAT
Strong3 Hubble3 8	ACCCTGACTATGCTTTAAACAGTTCAGAATTT
Strong3 Hole3 1	AGGAAACCGAACTGGCATGATTAAGACTCCTTTTCCTGAATCTTAAA
Strong3 Hole3 2	TAAAACCTTCAGAAAAGCCCCAAAAACAGGAAACATAACGCCAAGA
Strong3 Hole3 3	GCTAATGCACAGAGGTGTGCCACGCTGAGAGCAGCAGCAAATG
Strong3 Hole3 4	GAGAATGATAAATTAATACAAAAGGGCAAAGAATCGTCTCG
Strong3 Hole3 5	AACGCTAACGAGCGTCTTTTGTTCAAAGTCAGAGGG
Strong3 Hole3 6	ATGTAATTTAGGCAGAGGAATAACAACATGTTAC

Name	Sequence
Strong3 Hole3 7	GGAATTACGAGGCATACAAAAGAACGTTAACG

TABLE VIII: Staple sequences for A-triangle.

Name	Sequence
Core 1 Side1 1	GAGGGTTGATATAAGGATAAGTGATTGTGAAGAGTAGTATTCATCAACAGGCGCA
Core 1 Side1 2	ACAAATTCGGTGGTTTTCCAGTCACGAATTGGAGACAAAACGGATAACCTCTCG
Core 1 Side1 3	GTTTTAACCCGTACTIONGATTAGCGGGTTTTACGCAATAATAACGGATGCAACT
Core 1 Side1 4	TTAACCAATAGGAACGTGCATCTGCCAGTTTGAGGGGACAGCCTTATCCCGAC
Core 1 Side1 5	AAGGCTTATCCGGTTACAATTTTAAAAACAGGGAAGCGCATTAGATAAGAGAA
Core 1 Side1 6	TTTAAGAGCTGACCAATTGGGATTGTGTGCGAAATCCACAAAAGTACAACGGA
Core 1 Side1 7	AAGCTAAATCGGTACAAGAGATAGACTTTCTCGAAAAAGCGTCTGGAG
Core 1 Side1 8	GTGGAGCCACGGCCAGTGCCAAGCGGTGCCGATTTCACATACATAA
Core 1 Side1 9	GAAGTTTCGAAGGAAAACCGAACTTAATGACCATAAATCGATTTAGG
Core 1 Side1 10	CCCAATAAATAACCCAAATTGAGCGCTAATATAACGATCTAAAAGTTTT
Core 1 Side1 11	CGAGAAACCCGAGGAATGCTCAGTACCAGGCGTATAGCCCAATACCAC
Core 1 Side1 12	ATTCTGCGAACGAGTAGATTTAGTTTGACCATGTTTACCAATAGCTAT
Core 1 Side1 13	CCCTCATAGTTAGCGTATAGTAAGATTCAACTCATTATACTATGCGAT
Core 1 Side1 14	TCAACCGGAAACAATCGGCGAAACGTTGTACCAAAAACAAAGGGTGA
Core 1 Side1 15	TAAACACCGGAACCTTATACCGACCGTGTGATAACCTGTAGAGCATA
Core 1 Side1 16	AAAGTACCCATTAAGAGACTTTTTTCATGATAACAGTTACAGATCA
Core 1 Side1 17	GGAATAGGACAGACAGGTCGTCTTTCCAGACGTTAGTAA
Core 1 Side1 18	TAGGCTGTTTCAGAGCCTGATAACTTGAGATTTAGCAAG
Core 1 Side1 19	AAACCAGGTTCCGGCACCGCTTCTACTGGCTAATGCAG
Core 1 Side1 20	GAGTTAAGCGCGCCTCAGGAAGATCGCATTATTAAGT
Core 1 Side1 21	CAACAGTTATCATATGCGTTATGTCCCGGAATTTGTG
Core 1 Side1 22	CGAACAAAGTTACCAAAGTAAGCAGATAGCAGCCCTT
Core 1 Side1 23	CATCTCCAGCCAGCTCAAAGCGCCATTCGCGTCCGTT
Core 1 Side1 24	ACCCGACTTCTAATATAAAGACCAATCTTTAAACAA
Core 1 Side1 25	ATTACTACGTGGTGAAGGGATAAAGCCTCTTAGCTA
Core 1 Side1 26	AGGTTGGGTTATATAATTACGAGCATGTAGAA
Core 1 Side1 27	TTGCGGGACCAACGCTTGGGTAACGCCAGTTA
Core 1 Side1 28	AATCAAGATTAAGTGAACACCCTGAACAAAGT
Core 1 Side1 29	GATTTGTACTTACCGAAAACAATGAAATAGCA
Core 1 Side1 30	CAGAGGGTCAAGAATFGGTTTTGAGACGACAG
Core 1 Side1 31	TTTAATCCCGTCGATAAGACCAGTATAAAG
Core 1 Side1 32	TATCGAAAAGGAATTACGAGGCCAGAGAG
Core 1 Side2 1	TAGCAATACCGAACGAGCACTCATCGTAGGAATTCATCAACGGATTGACCGTAATG
Core 1 Side2 2	CGTTTTTATTTTCATCGAGAACAACAGGAAGGTCAATCAAGAGGGTACTAGCTGA
Core 1 Side2 3	AGGGCGATCCCGTAAAAAAGCCGCACAGGCAGAATCCTAGTTTTTTTTCCACCAG
Core 1 Side2 4	TAGCTGTTGTGCTGCCAGCTGCATTAATGAAAGAAATAAAGAAATTCATTTGAA
Core 1 Side2 5	ACGCTGAGAAGAGTCTTTCTGCTCATTAAAGCCTTAGAATCCTTGAAACATTCTG
Core 1 Side2 6	TGCTTCTGCGTAAAACCTCGGCCAACGCGCGTCGGATTCTCCGTGGGAGTGAGTG
Core 1 Side2 7	CAACATGTTTTGTTTTCGCTAACGAGCGTCTTTCCAGAGGCGCCATGCAGAAC
Core 1 Side2 8	TCATCTTTGATGCAAATCCAATTCCTGAACCATTCCAACAAATCAGATATAG
Core 1 Side2 9	GGCAAGGCGCGGATCACCGAAACTTTTTCAAATATATTTTTCAATTCT
Core 1 Side2 10	TTACCTTTTTTAATGGGGCAAATCTATTTGCAAACCCTTCAAAATCCC
Core 1 Side2 11	CAAATTAACAACTTAAAAATAGTGAAGTACTAGCATATTCGGTGCAGGCGCTC
Core 1 Side2 12	AAAGCGTAGCTATTAGAAAGGAATTGAGGAAGAACAAATTCGCTAGAT
Core 1 Side2 13	ACCTGTTTATCAACAATAGATAAGCGCAAGACAGGTCTGAAGAGACGC
Core 1 Side2 14	AAGGATAAGATAGCTTAGATTTGCCGCTAAATCATAACAGGAGAAAG
Core 1 Side2 15	CAAAATAAACAAACGGCATTAATAACGTTAATTAAGCAAATATTTAA
Core 1 Side2 16	AAATTAATTACATTTGTTATCTAATGGAAGGTGGCACAGAATCCTGT
Core 1 Side2 17	TTATAATCGAGACGGGAGGGTGGTTTTTCTTTATTGTAAGTGAGCG
Core 1 Side2 18	ATGCCGGTATGTACCTCATATATTTTAAACCTTTATTTCAACGC
Core 1 Side2 19	TGCAATGCCTGAGTAAATCGTAAAATTTATCACAAGTACC
Core 1 Side2 20	CAGTGCCACGCTGAGACTTGCTGAGGTCAAGTTAAACAGTA
Core 1 Side2 21	AGTGTGTTCCAGTTTTTCACCAGTAGAAAAGCAGTAACAA
Core 1 Side2 22	TAAAAGGGTACGTGAAACGTTGACTCCAATTTAGTCCACT
Core 1 Side2 23	GTATTAATTTAGGAGCACTAACAAAACATCAAGAAAACA
Core 1 Side2 24	ACTGCTCAATCGTCTGTTTGAATGAGAATACGGTTAGAAC
Core 1 Side2 25	ACCTGCAGCCAGCGGTCTTCACCGGGTTCCGACATGGTCA

Name	Sequence
Core 1 Side2 26	TAAAAAATGGCCACAACATAGCAAACGTCAAAGGGCGA
Core 1 Side2 27	TAAATTAGGAACAAGTTAGAACCCCGGTTGGCCTTTTC
Core 1 Side2 28	TTCTGTAGCCAGCTTCATTACCCCTAATTTTCCCAATC
Core 1 Side2 29	GTAATGGGTAAAGGTGTTGCCCTGCCCCCTGTACACGA
Core 1 Side2 30	ACAGCCATATAAAACACCTCAATTCGCCATGCCTGCAA
Core 1 Side2 31	AGTCTGTCCATCACGCAAAGCAGTTGGGCGGTTGTGTA
Core 1 Side2 32	CAACAGCTGATTGCCGCCGAGATAGGGTTGATTAAGA
Core 1 Side2 33	TAAATCGTCCCGGGGAGAGGCGGTTTGCAATAATCGGC
Core 1 Side2 34	AGAAACAAAAGAATACTAATAGTAGTAGCATTAAACATC
Core 1 Side2 35	TATTGCGCAGGAACGGTACGCCGGCCTTTACGTCAGCG
Core 1 Side2 36	CTGAATAAAATATCTCCTTTGACAATATTAATGGAT
Core 1 Side2 37	TTGCTAATTAACAAATCATAAAGAACGCGAGATTG
Core 1 Side2 38	ATAAATCAAAGAATAGCCCGGTGCGGCTGCCATCAC
Core 1 Side2 39	GTTAAACGTTAAAGGGATTTTAGACGTAACCA
Core 1 Side2 40	GCGCCACCAGCAGAAGATTATTTAGCCAGTTA
Core 1 Side2 41	TGGTGTGTTCTGATCCCAAATCAGAGAAGTG
Core 1 Side2 42	AAAACCGTCTGTCAGCAGCAACCGGGTCACT
Core 1 Side2 43	CGCTATTAATAACCTCATAAATCAATATAT
Core 1 Side2 44	GCTTACATTGGCAGAGGGTTCGATATGAGCC
Core 1 Side2 45	CCCCAAAAGCAAGCATTAAACAGAGATAG
Core 2 Side3 1	TAATTTTCCACCCTCACCTCATGTTTGCCAATCAAAAAGATTATCATCATAAAT
Core 2 Side3 2	CGTCACCCAACCTAAAACGAAAGGCAATGCGGCTTAGATTAAGGTCACGTAAT
Core 2 Side3 3	CTTGACGGGGGAAGAATGTGGTGACGACGCGTCCACGCTTTCCACACAGATGATG
Core 2 Side3 4	CGGAATCGCGGTCATAGTGTAAGTTTATCAGAAAAGGAGAAAATCTCCAAAAAAA
Core 2 Side3 5	CTCAAATGAGCAAAGCACTAACGGACCCTCAGGCCAATAAGGAATTGCGAATAA
Core 2 Side3 6	GAACCGCCAACAACATAATAGCGAGAGGCTTTTGCAAAAATAGCAAAGCCACC
Core 2 Side3 7	GAGCCTCCCGTGCCTGTTCTTCGCAGCAAAGAATGCGGGGGTCAGGCGAAC
Core 2 Side3 8	CCATCCCAGCTTTTCGCACTCAATCGTGCCTCAGCGAAAGCGGAACAA
Core 2 Side3 9	TTTGAATACCAAGTTAGGATTCGCTGATTGCGCTAACTCAGCCGGAA
Core 2 Side3 10	CAGCTTGATGTGAGGACAGGTCCAAACCAGACCGTTTAAATTCGAGCT
Core 2 Side3 11	ACAATAACCAAAATCGCGCAGAGGCGAATTATTCATTTACAGTACCT
Core 2 Side3 12	AACTCCAATTAGAGAGTACCTTTAATAAGAATACACTAAGTCAATCA
Core 2 Side3 13	AGTTTCGTCAGCGGAGTGAGAATAGAAAGGATCTGAATTCACCTCA
Core 2 Side3 14	TTATCATCATATTTCCCAGAAGGTTTCTGCCTGCGGCCATCGTTAAC
Core 2 Side3 15	GTTAAAGGCCGCTTTTGCGGGATATTATTCAGCTTAATTTAGACTG
Core 2 Side3 16	AGAAACCATGATTATCAACATACGACATTAATTGCGTTGCGCTCACT
Core 2 Side3 17	TAATGCTAGGACCTCAGCAGCGAAAGACAGCATCGGATTGAGGG
Core 2 Side3 18	TTTAGAGGAATCCCGAAAGAATCCCGAACTTGCAGTTCCTTTT
Core 2 Side3 19	ATAGCGTCCAATACTGCGTCCGTGCATAAACCGGGGAGCGGAA
Core 2 Side3 20	GCTGGAGGTACCGATAAGGTGAATTTCTTAAACGGTCATA
Core 2 Side3 21	TAGACTGGATTCATTGAATCCCCCAACTTCAAATATCG
Core 2 Side3 22	GTAATAGTAAAACGAGGATTGCTCTTTTCTTTCATC
Core 2 Side3 23	TAAGGGAAAACGTAACCTAGCGCGTATAATCAA
Core 2 Side3 24	CAGTAGCGCGGAACCGAATCACCGGAACCGA
Core 2 Side3 25	CTTGCCCTTATTAGCTGTATCGGCCTAGGGG
Core 2 Side3 26	CATCGCCACGCATAACGACAATGACAACAAC
Core 2 Side3 27	GCGGGCCGGCCTTTCGGTGGCGAGAAAGGAA
Core 2 Side3 28	GGAAAGCCTTGCAGGCCGCAACCAGCTTACG
Core 2 Side3 29	TTACACTGGTGTGTTTCAAAGCGGCATCAGC
Core 2 Side3 30	GCCAGGGGGTGCCTAATGAGTGAAGGCTCC
Core 2 Side3 31	ACAGAATCAAGTAAATATTGACGGAA
Core 2 Side3 32	AAGAGGCATTTTGCCTTTAGCGGCTGAATA
Core 2 Side3 33	GCCCCCGCAGACCGCTCTCGTCTGGCA
Core2 Side12 1	CAAATAAGAAACGATTTTCAGCTAAATAGCAAAGGAAACGGGTTTACGCCCTTTTTCAGCTGGC
Core2 Side12 2	AGTAATTCTGTTTTTTCCAGACGACGAATAATATCCTTTTTTCATCCTAATCTATATG
Core2 Side12 3	GAACGCGATCGCCATAGAAAGGGGCAAACAAGAGAATTTTTTCGATGAACGGTA
Core2 Side12 4	GTA AACGGCCACGGGGTCAAATCACCATCAATATGTTTTTATATTCAACCGTT
Core2 Side12 5	GCTATTTTTCAGAGATTTTTTCTACAAAGGCTATCAGCATTACAGGGCAAGGCG
Core2 Side12 6	TGTGTAGGTTTTTTAAAGATTCAATTATGACCTTTTTCTGTAATACTTTTTGC
Core2 Side12 7	TATTTTCATTTGGGGCGCTTTTTGAGCTGAAAAGGTGGCAAGTAAAT
Core2 Side12 8	TATTTGCCGTAACCGCCATCAAAAATAATTCGTTTTTCGTCTGGCC
Core2 Side12 9	TACCGACAAAAGGTAAGAATAACATATCCTGAATTTTTCTTACCAA
Core2 Side12 10	ATTTTGTAAAATTCGCATTTTTTTAAATTTTTGTAAATCAGCT

Name	Sequence
Core2 Side12 11	ATAAATCGGCTGTCTTTTCTTTTTTTATAAGAAAACAATAAA
Core2 Side12 12	TAGCAAATTAAGTTTTTCAATAGCTCTCATTTTTTCGGAAAA
Core2 Side12 13	GATGTGCTCTGCGCAACTTTTTTGTGGGAAGGGCGATGTA
Core2 Side12 14	AACGTCAAAAATGAAAATAGCTTTTTTAGCCTTTACAGAGA
Core2 Side12 15	TAAATGCCTGATTTTTTCTAAATTTAATGGTTTTGAA
Core2 Side12 16	GGATAGGTACAGTTGGTGTTTTTTAGATGGGGCGCAT
Core2 Side12 17	GAGACTACCTTTTTTTTTTTAACCTCCGGTCATA
Core 2 Side23 1	ATTACCTGAGCAAAAAGAATTTTTTTTTGATGAAACACTAATAGATTTTTTTAGAGCCGTCA
Core 2 Side23 2	ATGCTGATTTTTTTTTCCGTTCCGGCAAACGCGGTGAGAATCAGAGCGGGACTACAGG
Core 2 Side23 3	TCACAGTTGAGGATCCCTTTTTTTGTACCGAGCTCGAATTCGTGTATTGGGCGCC
Core 2 Side23 4	GGGAGAAGCAATTCATCAATATAACATTATCCAGCTTTTTTGCGGAACCCGAAC
Core 2 Side23 5	GCAAGAATGCCAACTTTTTTGCAGCACCGTCCGGTGGTGGCCTCCGGATTTAGAG
Core 2 Side23 6	ATAACGGACGTGCCGGACTTAAAGCACTAATTTTTTTCCGAACCCTAAAGGGA
Core 2 Side23 7	CCACACCCGCGCGCTTTTTTTATGCGCCGGCTAAACTTTTTTTGAGGCCGA
Core 2 Side23 8	GCGCGTACTATGGTTGCGCTAGGGCGCTGGCAAGTTTTTTGTAGCGGTAC
Core 2 Side23 9	TTTACATCGCCCGCTTTTTTTTTTCAGTCGGGAAACCTTCCTGTGTGAAATT
Core 2 Side23 10	CATCAGACTTGATGGTCCCTGGCCCTTTTTTTAGAGAGTTGCAGCAACG
Core 2 Side23 11	CGCCGGGCGCGTTGCGGGGTGCCGTGTAGAAGTGATGAAGGGTAAA
Core 2 Side23 12	TTCTTTGCTTTTTTTGTCATAAACATCCCGGCATCAGATGCCGGG
Core 2 Side23 13	TTTCAGGTTTAACGTCAGATGAATATTTTTTTTCAGTAA
Core 2 Side23 14	TTAGACTTTTTTTTTTAAACAATTCGACAACCTC
Core 2 Side23 15	GATCCAGCGCAGTGTTTTTTTCACATGCGCGCT
Core 2 Side31 1	TCTGTATGGGATTTTGTTTTTTTTAAACAACCTTTCATGGCTTTTGTTTTTTTGATACAGGA
Core 2 Side31 2	TGAGACTCCTCATTTTTTTGAGAATGCCCGTGTACTGGTAATAAATGAATTTAACTACAA
Core 2 Side31 3	GCGACCTGGTACAGACGAGTAATCTTGACAAGTTTTTTTTCCGGATATTCATTACC
Core 2 Side31 4	CGGAAGCAGACCAACTTTGAAAGAGGACATTTTTTTTTGAACGGTCTCCATGT
Core 2 Side31 5	GGTTTACCAGCGCCAATTTTAAATAATACCCAAAATTTTTTAACTGGCATG
Core 2 Side31 6	GAGGCTTTGAGGACTAACGGGTAAAATACGTAATGTTTTTTCACTACGA
Core 2 Side31 7	AGGGCGACTTTTTTTCAACCCGAACGATTTTTTTGTAGCAACGGCTACA
Core 2 Side31 8	AAAGCTGCTAGTCAGACTTTAAACATTTTTTTTCAGAAAACGAGACCT
Core 2 Side31 9	CAGTCAGGACGTTGGGTTTTTTTTGAAAAATCTACGTTAATAAAATGTT
Core 2 Side31 10	AAACATGACCAGTAAGCGTCATACAACAGTTTCACCAGTTTTTTTACA
Core 2 Side31 11	AGGGAAGGACTCCTTATTACGCAGTATGTTAGTTTTTTTTAACGTAGA
Core 2 Side31 12	AAACAGTTAAGGATTAAGGAGTTTAGTTTTTTTACCGCCACCCTCA
Core 2 Side31 13	AACACTCATTTTTTTTTTGACCCCGAGGATTATACCAGGAAGTTT
Core 2 Side31 14	AAAAATCAGGTCTTTTTTTTTTACCCTGACTATTATCATTTCAGTGAAT
Core 2 Side31 15	AGGCTTGCCCTGATACTTAGCCGGAATTTTTTTGAGGCGCAGACG
Core 2 Side31 16	AGCAACACTATCATAACCCTCGTTTACCATTTTTTTACAGCATA
Core 2 Side31 17	AAAACCAATATTACAGGTAGAAATTTTTTATTCATCAGTTGA
Core 2 Side31 18	GTAGCTCAATTTTTTTATGAGACAAAAAATACATACATAAA
Core 2 Side31 19	CCTGCCTATTTTTTTTTCGGAACCTATTATTCTG
Active Hole1 1	GAAAGGCCGCCTGAGACTGTTTAGAGGGCTTATGTAATTTAGGCA
Active Hole1 2	TTAAATAAGAACGCCAACAAATTGAGAAGGCGTTTTAGCGAACCC
Active Hole1 3	GTTTATTTTTGTGATTCCCATTTAAGAAATTCATAAGCGCGAA
Active Hole1 4	GGTGTCTGATAGAAAAAGAAACGCAAAGACACCACGGAATAA
Active Hole1 5	TTGAGTAACAGTGCCCGTATGGTGGCAACATATAAATTCATAT
Active Hole1 6	GCGCCATTAGATACATTTTCGCAAATGGTCAATAAATAAGGCG
Active Hole1 7	GAGGCATTTTCGAGCCAGTAACGGGAGAATTAGTTGC
Active Hole1 8	CGCCTGTAGCATTTCCTGTATCAGGGGTGAGTGCC
Active Hubble2 1	TGACCTGCCAGTAAGAACTCAATTTTTTATACGCTCATGGAATACCTAC
Active Hubble2 2	CTAAAACACAATATCTACCTCAAATATCAAACGAGGTGAGGCGGT
Active Hubble2 3	ATTTTGACATCGGCCTTGCTGGTAATAAGGAAAAAATCAGTGA
Active Hubble2 4	AAATCTAAAGCATCACGCCAGCAGGCGGAACGAGTAGAA
Active Hubble2 5	CGCCAGCCATTGCAACTCCAGAACACTTGCCTTGATAGCC
Active Hubble2 6	CATCGACAGGCCACCGAGTAAAAGATAACATCAATATTAC
Active Hubble2 7	CTACCATATCAAATAACAGTTGTCTTTAATCAAATGAA
Active Hubble2 8	CAGTATTAACACCTAAAAATACTTCTTTGATTAGTA
Active Hubble3 1	GGAACCCATGTACCGTAACACTGGAACCGCTACCGTTAAGTATTAGGTCAGA
Active Hubble3 2	GCAGCACCCAGCCAGCATTGACAGGAGTCAACAAACGCGCAGTCACAATAA
Active Hubble3 3	CCTCCCTCAATGGAAAAAATAAATCCTCATTAAGAGCCGCCACCA
Active Hubble3 4	AAGCCAGAGCCGAGCCGCGGTAGCACCATTACCATTAGCAA
Active Hubble3 5	GAGACACCAGCCACCCTCAGAACCGCCAC
Active Hubble3 6	GGCCGGAACCGTCCACCGTCATGCAGGGAGATAAGAG

Name	Sequence
Active Hubble3 7	GCAAAATGAATTATACCAATGAAACCATCGATA
Active Hubble3 8	CGATTGGCCTTGATATGTTGAGGCGCCACCAC
Active Hole3 1	TTATCCGCTCACAAGGTTTGCCATTTTGGAGCGGGCTTTGACGAGCAC
Active Hole3 2	GAGGATTTGTTGAGTAATCCTGATTGTTTTTTTTGGATTATACTT
Active Hole3 3	GTTATTAATTTTTTTTTAAAAAGAAGTAATAGATAATACATTT
Active Hole3 4	CCTCAGAGCCATCACGTTGCCTTAATTTTTCAGGGGAAGTTTT
Active Hole3 5	GTTGCGCCCGATATATTCGGTCGCTGAGGCTCCGACTTGAGC
Active Hole3 6	GTATAACGTGCTTTCCTCGTTCGTTTTTTTACATCCTC
Active Hole3 7	CATTTGGGAATTAGAGCCAGGCATTTTTGTCATTTT
Passive Hole1 1	GAAAGGCCGCTGAGACTGTTTAGAGGGCTTATGTAATTTAGGCATTTTT
Passive Hole1 2	TTTTTTTAAATAAGAACGCCAACAATTGAGAAGGCGTTTTAGCGAACC
Passive Hole1 3	TTTTTGTTTTATTTTGTGATTCCCATTAAAGAAATTCATAAGCGCGAA
Passive Hole1 4	GGTGTCTGATAGAAAAAAGAAACGCAAAGACACCACGGAATAATTTTT
Passive Hole1 5	TTTTTTTGAGTAACAGTGCCCGTATGGTGGCAACATATAATTCATAT
Passive Hole1 6	CGCCATTAGATACATTTTCGCAAATGGTCAATAAATAAGGCGTTTTT
Passive Hole1 7	TTTTTGAGGCATTTTCGAGCCAGTAACGGGAGAATTAGTTGC
Passive Hole1 8	CGCCTGTAGCATTCTGTATCAGGGGTCAGTGCCTTTTT
Passive Hubble2 1	TGACCTGCCAGTAAGAACTCAATTTTTTATACGCTCATGGAAATACCTACTTTTT
Passive Hubble2 2	CTAAAACACAATATCTACCTCAAATATCAAACGAGGTGAGGCGTTTTTTT
Passive Hubble2 3	TTTTTATTTTGACATCGGCCCTTGCTGTAATAAGGAAAAAATCAGTGA
Passive Hubble2 4	TTTTTAAATCTAAGCATCACGCCAGCAGCGCGAACCAGTAGAA
Passive Hubble2 5	TTTTTCGCCAGCCATTGCAACTCCAGAACACTTGCCTTGATAGCC
Passive Hubble2 6	CATCGACAGGCCACCGAGTAAAAGATAACATCAATATTACTTTTT
Passive Hubble2 7	CTACCATATCAAAAATAACAGTTGTCTTTAATCAAATGAATTTTT
Passive Hubble2 8	TTTTTCAGTATTAACACCTAAAATACTTCTTTGATTAGTA
Passive Hubble3 1	GGAACCCATGTACCGTAACACTGGAACCGCTACCGTTAAGTATTAGGTCAGATTTTT
Passive Hubble3 2	TTTTTGCAGCACCCAGCCAGCATTGACAGGAGTCACAAACGCGCAGTCACAACATA
Passive Hubble3 3	CCTCCCTCAATGGAAAAAATAAATCCTCATTAAGAGCCGCCACCATTTTT
Passive Hubble3 4	AAGCCAGAGAGCCGAGCCGCGCTAGCACCATTACCATTAGCAATTTTT
Passive Hubble3 5	TTTTTGAACCACCACCAGCCACCCTCAGAACCGCCACTTTTT
Passive Hubble3 6	TTTTTGCCCGGAAACGTCCACCGTCATGCAGGGAGATAAGAG
Passive Hubble3 7	GCAAAATGAATTATACCAATGAAACCATCGATATTTTT
Passive Hubble3 8	TTTTTCGATTGGCCTTGATATGTTGAGGCGCCACCAC
Passive Hole3 1	TTATCCGCTCACAAGGTTTGCCATTTTGGAGCGGGCTTTGACGAGCACTTTTT
Passive Hole3 2	TTTTTGAGGATTTGTTTGGAGTAATCCTGATTGTTTTTTTTGGATTATACTT
Passive Hole3 3	GTTATTAATTTTTTTTTAAAAAGAAGTAATAGATAATACATTTTTTTTT
Passive Hole3 4	TTTTTCCTCAGAGCCATCACGTTGCCTTAATTTTTCAGGGGAAGTTTT
Passive Hole3 5	GTTGCGCCCGATATATTCGGTCGCTGAGGCTCCGACTTGAGCTTTTT
Passive Hole3 6	TTTTTGTATAACGTGCTTTCCTCGTTCGTTTTTTTACATCCTC
Passive Hole3 7	TTTTTCATTTGGGAATTAGAGCCAGGCATTTTTGTCATTTT
Strong3 Hole1 1	GAAAGGCCGCTGAGACTGTTTAGAGGGCTTATGTAATTTAGGCATCA
Strong3 Hole1 2	GGTGTCTGATAGAAAAAAGAAACGCAAAGACACCACGGAATAAAGA
Strong3 Hole1 3	GCGCCATTAGATACATTTTCGCAAATGGTCAATAAATAAGGCGCTC
Strong3 Hole1 4	AATAAGAACGCCAACAATTGAGAAGGCGTTTTAGCGAACC
Strong3 Hole1 5	TATTTTGTGATTCCCATTAAAGAAATTCATAAGCGCGAA
Strong3 Hole1 6	AGTAACAGTGCCTGATGGTGGCAACATATAATTCATAT
Strong3 Hole1 7	CGCCTGTAGCATTCTGTATCAGGGGTCAGTGCCGGG
Strong3 Hole1 8	GCATTTTCGAGCCAGTAACGGGAGAATTAGTTGC
Strong3 Hubble2 1	TGACCTGCCAGTAAGAACTCAATTTTTTATACGCTCATGGAAATACCTACTGC
Strong3 Hubble2 2	CTAAAACACAATATCTACCTCAAATATCAAACGAGGTGAGGCGGTGCG
Strong3 Hubble2 3	CATCGACAGGCCACCGAGTAAAAGATAACATCAATATTACGCT
Strong3 Hubble2 4	CTACCATATCAAAAATAACAGTTGTCTTTAATCAAATGAATTG
Strong3 Hubble2 5	TTGACATCGCCTTGCTGGTAATAAGGAAAAAATCAGTGA
Strong3 Hubble2 6	TCTAAAGCATCACGCCAGCAGGCGCGAACCAGTAGAA
Strong3 Hubble2 7	CAGCCATTGCAACTCCAGAACAATTGCCCTTGATAGCC
Strong3 Hubble2 8	TATTAACACCTAAAATACTTCTTTGATTAGTA
Strong3 Hubble3 1	GGAACCCATGTACCGTAACACTGGAACCGCTACCGTTAAGTATTAGGTCAGAGAG
Strong3 Hubble3 2	GCACCCAGCCAGCATTGACAGGAGTCACAAACGCGCAGTCACAACATA
Strong3 Hubble3 3	CCTCCCTCAATGGAAAAAATAAATCCTCATTAAGAGCCGCCACCACCT
Strong3 Hubble3 4	AAGCCAGAGAGCCGAGCCGCGCTAGCACCATTACCATTAGCAACAT
Strong3 Hubble3 5	GCAAAATGAATTATACCAATGAAACCATCGATAGTA
Strong3 Hubble3 6	CGGAAACGTCCACCGTCATGCAGGGAGATAAGAG
Strong3 Hubble3 7	CCACCACCAGCCACCCTCAGAACCGCCACGAA

Name	Sequence
Strong3 Hubble3 8	TTGGCCTTGATATGTTGAGGCGCCACCAC
Strong3 Hole3 1	TTATCCGCTCACAAAGTTTGCCATTTTGGAGCGGGCTTTGACGAGCACGCA
Strong3 Hole3 2	GTTATTAATTTTTTTTTTAAAAAGAAGTAATAGATAATACATTTTCTGA
Strong3 Hole3 3	GTTGCGCCCGATATATTCGGTCGCTGAGGCTCCGACTTGAGCGGC
Strong3 Hole3 4	GATTTGTTTGAGTAATCCTGATTGTTTTTTTTTGGATTATACTT
Strong3 Hole3 5	CAGAGCCATCACGTTGCCTTTAATTTTCAGGGGAAGTTTT
Strong3 Hole3 6	TAACGTGCTTTCCTCGTTCGTTTTTTTACATCCTC
Strong3 Hole3 7	TTGGAATTAGAGCCAGGCATTTTGTCATTTT

TABLE IX: Staple sequences for B-triangle.